SMOS Wind Data Service

Algorithm Theoretical

Basis Document

	Function	Name	Signature	Date
Prepared by	Consortium	IFREMER,ODL Nicolas Reul and Joseph Tenerelli		01/07/2021
Accepted by	ESA technical officer	Raffaele Crapolicchio	Raffaele Crapolicchio	Digitally signed by Raffaele Crapolicchio DN: cn=Raffaele Crapolicchio, o=ESA, ou=EOP-GMQ, email=raffaele.crapolicchio@esa.int, c=IT Date: 2021.08.04 11:05:22 +02'00'

Laboratoire d'Océanographie Physique et Spatiale – Z.I. Pointe du Diable-B. P. 70, Plouzané – France
Tél. : +33 (0)2 98 22 44 10 – Fax : +33 (0)2. 98. 22. 45. 33 – E-mail : nreul@ifremer.fr

Indexing form

Customer	ESA/ESRIN	Contract N°4000122821/17/I-EF	-

Confidentiality codes				**Document management**	
Company / Programme		Defence			
Non-protected	☐	Non-protected	☒	None	☐
Reserved	☒	Limited diffusion	☐	Internal	☒
Confidential	☐	Defence confidentiality	☐	Customer	☐

Contractual document		**Project N°**	**Work Package**
Yes	☒		-
No	☐		

ATBD

Summary
SMOS Wind Data Service-Algorithm Theoretical Basis Document

Document			
File name	SMOS_WIND_DS_ATBD.docx	Nbr of pages	89
Project	-	Nbr of tables	0
Software	Microsoft Office Word	Nbr of figures	0
Language	English	Nbr of appendices	0

Document reference					
Internal	SMOS_WIND_DS_ATBD	Issue	1	Date	18/03/2019
External	-	Revision	5	Date	04/08/2021

Author(s)	**Verified by**	**Authorised by**
Nicolas REUL		Raffaele Crapolicchio

Laboratoire d'Océanographie Physique et Spatiale – Z.I. Pointe du Diable-B. P. 70, Plouzané – France
Tél. : +33 (0)2 98 22 44 10 – Fax : +33 (0)2. 98. 22. 45. 33 – E-mail : nreul@ifremer.fr

Distribution list

INTERNAL	EXTERNAL	
Name	Name	Company / Organisation
N. REUL J.TENERELLI S. HERLEDAN J-F. PIOLLE C. LE JEUNE	R. CRAPOLICCHIO	ESA

Document status

Title SMOS wind data service: Algorithm Theoretical Basis Document			
Issue	**Revision**	**Date**	**Reason for the revision**
1	0	13/03/2018	Initial version
1	3	20/09/2019	Final first version (v110 baseline)
1	4	01/07/2021	Second version
1	5	04/08/2021	Final second version (v300 baseline)

Modification status				
Issue	Rev	Status *	Modified pages	Reason for the modification
1	2		Pages 52-64	Update of the quality levels following the ORR meeting in Brest, 19-20, Sep 2019
1	3		Section 3.7.2.4, table 7 & 8	Update of the QL description following R. Crappolicio email from 2019-09-24
1	4		Added p7	Summary of ATBD upates on July 2021
			Section 3.4.1	Update of the dielectric constant model
			Section 3.6	Description o the Bayesian retrieval Method
			Section 4.3	Update of the fraction of missing data for wind radii estimates
1	5		n/a	RC full document review

* *I = Inserted* *D = deleted* *M = Modified*

Table of contents

Scope and structure of the Document

This document is the Algorithm Theoretical Basis Document (ATBD) of the SMOS Wind Data Service project. An overview is provided in §1. The Algorithm used to generate the SMOS Level2 NRT wind products is described in §2 and §3. The algorithm used to generate the NRT wind radii estimates from the SMOS wind L2 swath data intercepts with Tropical Cyclones is described in §4. The algorithm used to generate the SMOS Level 3 wind daily products is given in §5.

Note: ATBD update as of 1st July 2021.

With respect the previous ATBD (ref: SMOS_WIND_DS_ATBD_20191107_signed.pdf) for product version 110, note that the following changes have been included into this updated ATBD applicable for product version 300:

1. An additional pre-processing step has been added for L1B images processed in Gibbs-2. This pre-processing computes the Brigthess Tempratures of the "artificial scene" removed during the L1B image reconstruction in Gibbs-2 and adds back these Brigthess Tempratures to obtain a final calibrated image. Algorithm theoretical basis about the computation of the "artificial scene" is available in [AD.7] and algorithm theoretical basis about the computation of the final calibrated image is available in [AD.8]. The SMOS wind processor follows exactly these algorithm basis by using the same level 1 processor software library.
2. In the preceding ATBD, a direct SMOS wind inversion method was used. However, it does not facilitate the introduction of constraints on the retrieved wind speed. The MIRAS measurements are sufficiently noisy that in low roughness conditions the weighted average excess emission can be negative, in which case the direct method yields negative wind speeds. To avoid this issue and to allow the introduction of additional a priori information on surface wind speed, a new wind retrieval method has been introduction. This Bayesian approach and its impacts are described in detail in §3.6.
3. A third change, applied to both the reprocessed and near real time products, involves use of the dielectric model described in [RD.33] to compute the specular emission (rather than the model of Klein and Swift [RD.13]).
4. The fourth change, applied only to the reprocessed dataset, involves use of version 1.9 CCI weekly averaged SSS [RD.34] instead of the daily mean SSS from the Mercator Ocean analysis system to compute the sea water dielectric constant at L-band.
5. The fifth change is about the threshold value of the fraction of non-missing wind data within the domain of a given geographical sector used to determine wind radii evolved from 50% to 30% (see section 4.3).

Applicable and Reference Documents

Applicable Documents (ADs)

The following documents, listed in order of precedence, contain requirements applicable to the activity:

Table-1: SMOS Wind Data Service Applicable Documents

Ref.	Title	Code	Version	Date
[AD.1]	SMOS NRT Product Format Specification Document	SO-ID-DMS-GS-0002	4.2	25.03.2019
[AD.2]	SMOS level 1 and auxiliary data products Format Specification Document	SO-TN-IDR-GS-0005	6.4	25.05.2018
[AD.3]	SMOS High Wind Speed: AlgorithmTheoretical Basis Document	SMOSpluSTORM_EVOLU_S _HWS_ATBD_v1.1	1.1	31.05.2016
[AD.4]	Definition of Coordinate System/Reference Frame and Units Nomenclature.	SO-PL-CASA-PLM-0022,	2.2	14/09/06.
[AD.5]	M.Zundo, B.Duesman. On-ground BT Frame of Reference TN	SO-TN-ESA-GS-5873	3.3	24/05/10
[AD.6]	SMOS Wind Data Service. Product Description Document.	SMOS_WIND_DS_PDD	1.5	01/07/2021
[AD.7]	SMOS L1 Processor L1a to L1b Data Processing Model	SO-DS-DME-L1OP-0008	2.25	12/07/2018
[AD.8]	SMOS L1 Processor L1c Data Processing Model	SO-DS-DME-L1OP-0008	2.17	28/11/2017

Reference Documents (RDs)

The following documents are relevant for the project:

Table-2: SMOS Wind Data Service Reference Documents

Ref.	Title	Code/Reference	Version	Date

[RD.1]	A revised L-band radio-brightness sensitivity to extreme winds under Tropical Cyclones: the five year SMOSstorm database	Remote Sensing of Environment 180 (2016)274–291	n/a	2016
[RD.2]	ECMWF – SMOS DPGS Interface	XSMS-GSEG-EOPG-ID-06-0002	4.4	22.01.2013
[RD.3]	SMAP L-Band Passive Microwave Observations Of Ocean Surface Wind During Severe Storms	Ieee Transactions On Geoscience And Remote Sensing , 54(12), 7339-7350	n/a	2016
[RD.4]	A new generation of Tropical Cyclone Size measurements from space.	Bulletin of the American Meteorological Society.	n/a	2017
[RD.5]	SMOS satellite L-band radiometer: A new capability for ocean surface remote sensing in hurricanes	Journal Of Geophysical Research-oceans , 117	n/a	2012
[RD.6]	Capability of the SMAP Mission to Measure Ocean Surface Winds in Storms	Bulletin of the American Meteorological Society.	n/a	2017
[RD.7]	Using routinely available information to estimate tropical cyclone wind structure.	Mon. Wea. Rev., 144:4, 1233-1247.	n/a	2016
[RD.8]	"International Workshop on Measuring High Wind Speeds over the Ocean"-Proceedings	SMOSSTORMEvolution_WKP_D160	n/a	2017
[RD.9]	SMOS L2 OS Algorithm Theoretical Baseline Document	SO-TN-ARG-GS-0007_L2OS-ATBD	v3.13	29 April 2016
[RD.10]	SMOS L2 OS OTT Post-Processor Software User Manual	O-MA-ARG-GS-0081_L2OS-OTTPPSUM	v0.4	29 April 2016
[RD.11]	E. Anterrieu, P. Waldteufel, and A. Lannes, Apodization functions for 2-d hexagonally sampled synthetic aperture imaging radiometers	IEEE Trans. Geosci. and Remote Sens., vol. 40, no. 3, pp. 2531-2541,	n/a	Dec. 2002.
[RD.12]	SMOS L2 OS Algorithm Theoretical Baseline Document	SO-TN-ARG-GS-0007	13	29 April 2016
[RD.13]	L. A. Klein and C. T. Swift. An Improved model of the dielectric	IEEE Trans. Antennas Propag., 25:104-111,		1977

	constant of sea water at microwave frequencies.			
[RD.14]	Nicolas Reul, Joseph Tenerelli, Bertrand Chapron, and Philippe Waldteufel. Modeling sun glitter at L-band for sea surface salinity remote sensing with SMOS.	IEEE Trans. Geosci. and Remote Sens.,45(7):2073-2087	n/a	2007
[RD.15]	A. G. Voronovich and V. U. Zavorotny, “Theoretical model for scattering of radar signals in Ku and C-bands from a rough sea surface with breaking waves	Waves Random Media, vol. 11, no. 3, pp. 247–269		2001
[RD.16]	Vladimir Kudryavtsev, Daniele Hauser, Gerard Caudal, and Bertrand Chapron. A semi-empirical model of the normalized radar cross-section of the sea surface-Part 1. background model.	J. Geophys. Res., 108(C3, 8054)		2003
[RD.17]	Tenerelli Joseph, Reul Nicolas, Mouche Alexis, Chapron Bertrand (2008). Earth-viewing L-band radiometer sensing of sea surface scattered celestial sky radiation - Part I: General characteristics	IEEE-Transactions on geoscience and remote sensing , 46(3), 659-674		2008
[RD.18]	H. J. Liebe, “MPM:An atmopsheric millimeter-wave propagation model,”	International Journal of Infrared and Millimeter Waves, vol. 10, no. 6, pp. 631–650.		July 1989
[RD.19]	H. J. Liebe, G. A. Hufford, and M. G. Cotton, “Propagation modeling of moist air and suspended water/ice particles at frequencies below 1000 GHz,”	in AGARD 52nd Specialists' Meeting of the Electromagnetic Wave Propagation Panel, pp. 3–1–3–10.		May 1993
[RD.20]	Arthur C. Ludwig. The definition of cross polarization.	IEEE Trans. Antennas Propag., AP-21(1):116-119,		Jan 1973.
[RD.21]	Nicolas Floury. Estimation of Faraday rotation from auxiliary data.	ESA Technical Note, September		2007
[RD.22]	Yin, X., J. Boutin, E. Dinnat, Q. Song, and A. Martin, 2016. Roughness and foam signature on smos-miras brightness temperatures: A semi-theoretical approach.	Remote sensing of environment, 180:221–233, 471.		2016

[RD.23]	Sampson, C. R., and A. J. Schrader, The Automated Tropical Cyclone Forecasting System (version 3.2).	Bull. Amer. Meteor. Soc., 81, 1231–1240		2000
[RD.24]	SMOS L1 Processor L1c Data Data Processing Model	SO-DS-DME-L1OP-0009	2.14	25/03/ 2014
[RD.25]	SMOS L1 Processor L1a to L1b Data Processing Model	SO-DS-DME-L1OP-0008	2.19	25/03/ 2014
[RD.26]	Garrison, J. L., Komjathy, A., Zavorotny, V. U., Katzberg, S. J.. Wind speed measurement using forward scattered GPS signals.	IEEE Transactions on Geoscience and Remote Sensing, 40 (1),50-65.doi: 10.1109/36.981349		2002
[RD.27]	Wilson, W.J., Yueh, S.H., Dinardo, S., Yi Chao, Fuk Li, 2003, Precision ocean salinity measurements using the Passive Active L/S-band aircraft instrument.	Geoscience and Remote Sensing Symposium, 2003. IGARSS '03. Proceedings. 2003 IEEE International Volume: 4, 2792- 2794.		2003
[RD.28]	Wilson, W.J., Yueh, S.H., Dinardo, S.J., Li, F.K. High-stability L-band radiometer measurements of saltwater.	IEEE Trans. Geosci. And Remote Sens., 42 (9), 1829-1835.		2004
[RD.29]	Reul, N., Tenerelli, J., Chapron, B., Guimbard, S., Picard, S.-S., Le Traon, P.-Y., Zine, S. Preparing the potential and challenge of remote sensing-based sea surface salinity estimation: The CoSMOS airborne campaign	Proceedings of the SPIE 7150, edited by R. J. Frouin et al. p. 715006, doi:10.1117/12.804940.		2008
[RD.30]	Cox,C.;Munk, W. Measurement of the roughness of the sea surface from photographs of the sun's glitter.	J. Opt. Soc. Am. 1954, 44, 838–850, doi:10.1364/JOSA.44.000838		1954
[RD.31]	ISAS-15 temperature and salinity gridded fields. Kolodziejczyk, N., Prigent-Mazella A. and F. Gaillard	https://doi.org/10.17882/52367 SEANOE		2017
[RD.32]	Wentz, F. J. (2005), The effect of clouds and rain on Aquarius salinity retrieval,	Tech. Memo. 3031805, Remote Sens. Syst., Santa Rosa, Calif.		2005
[RD.33]	J. Boutin, J. Vergely, E. Dinnat, P. Waldteufel, F. DAmico, N. Reul, A. Supply, and C.	IEEE Trans. Geosci. and Remote Sens., pp. 1-14,		Nov. 2020.

	Thouvenin-Masson, Correcting sea surface temperature spurious e ects in salinity retrieved from spaceborne L-Band radiometer measurements,"			
[RD.34]	Boutin, J.; Vergely, J.-L.; Koehler, J.; Rouffi, F.; Reul, N. (2019): ESA Sea Surface Salinity Climate Change Initiative (Sea_Surface_Salinity_cci): Version 1.8 data collection. Centre for Environmental Data Analysis, 25 November 2019.	doi:10.5285/9ef0ebf847564c2eabe62cac4899ec41. http://dx.doi.org/10.5285/9ef0ebf847564c2eabe62cac4899ec41		2019

Acronyms and Abbreviations

ATBD	Algorithm Theoretical Basis Document
ATCF	NOAA Automated Tropical Cyclone Forecast system
BC	Bias Correction
CMB	Cosmic Microwave Background
CMEMS	Copernicus Marine Environment Monitoring Service
DPGS	SMOS Data Processing Ground Segment
ECMWF	European Center for Medium Range Weather Forecasts
ETC	Extra Tropical Cyclone
ESA	European Space Agency
ESL	Expert Support Laboratory
FOV	Field Of View
GMF	Geophysical Model Function
GFDL	Geophysical Fluid Dynamic Laboratory
GNSS	Global Navigation Satellite System
GO	Geometrical Optics
HWIND	HRD real-time WIND analysis
HRD	NOAA’s Hurricane Research Division
ICD	Interface Control Document

IFREMER	Institut Francais de Recherche pour l'Exploitation de la Mer
IPP	Ionospheric Pierce Point
JTWC	Joint Typhoon Warning Center
KA	Kirchhoff Approximation
L1B	SMOS level 1B product type
LSC	Land Sea Contamination
MIRAS	Microwave Imaging Radiometer using Aperture Synthesis
NCEP	National Centers for Environmental Prediction
NHC	National Hurricane Center
NOAA	National Oceanic and Atmospheric Administration
NRT	Near Real Time
NWP	Numerical Weather Prediction
ODL	Ocean Data Lab
OTT	Ocean Target Transformation
QC	Quality Control
RFI	Radio Frequency Interference
RMS	Root Mean Square
RSGA	Report of Solar-Geophysical Activity
SFMR	Step Frequency Microwave Radiometer
SMOS	Soil Moisture and Ocean Salinity ESA's EO mission
SSS	Sea Surface Salinity
SST	Sea Surface Temperature
SWS	Surface Wind Speed
TC	Tropical Cyclone
TCGP	Tropical Cyclone Guidance Project
TECU	Total Electronic Content Unit
VTEC	Vertical Total Electronic Content
WEF	WEighting Function
WOA	World Ocean Atlas

1. Forewords and Overview

In the present document, we describe the updated algorithm (from [AD.3]) that is used to generate surface wind speed estimates in Near-Real Time (NRT) from the SMOS Level 1B brightness temperature datasets delivered by ESA in NRT to IFREMER in the context of the SMOS wind Data service project.

A general overview of the main algorithm steps is given in Fig. 1. A pre-processing (left block in Fig. 1) is first needed to prepare the data to be used in the wind speed retrieval algorithm (right block in Fig 1). Operational Level 1B data are provided in half-orbits packets, while NRT data blocks can contain snapshots from both ascending and descending passes, depending on the NRT data download to the SMOS ground stations. After reading the NRT Level 1B and associated data, the algorithm first identify the ascending & descending ½ orbit segments within the input data blocks. The processor then read the pre-generated Ocean Target Transformation (OTT) which corresponds to the time window of the input data block. The processor then apply the correction developed by N. Floury to correct the input Total Electronic Content fields for the satellite altitude. Auxilliary geophysical parameters from ECMWF (atmospheric parameters) or other sources (e.g. sea surface salinity from CMEMS ocean model) that are needed to evaluate the wind are then collected over the time period corresponding to each ½ orbit segment.

We then apply the wind speed retrieval algorithm per se, which contains a series of processing steps, namely:

- the algorithm separates ‘snapshots’ scenes from the Level 1B NRT ½ orbit data packets,
- it then estimates the measured First Stokes parameter at the antenna Level on the director cosine coordinates from Level 1B Fourier Coefficients,
- the algorithm then computes the forward model components for that scene except for the sea surface roughness & foam induced brightness temperature contrats,
- it then estimates the brightness temperature residuals obtained from the “measured minus modeled” First Stokes parameter,
- Radio Frequency Interferences (RFI), sun aliases filtering as well as Land/sea ice masks are then applied,
- the OTT correction is performed to estimate the bias-corrected First Stokes roughness and foam-induced brightness temperature residuals,
- the brightness temperature residuals ΔTb are then corrected for the Land Sea Contamination (LSC),
- an inversion algorithm of the $\Delta Tb=f(\text{wind})$ Geophysical Model Function (GMF) is finally used to derive the surface wind speed,
- the inversion error and quality indicators are estimated,
- output netcdf wind product NRT files are generated.

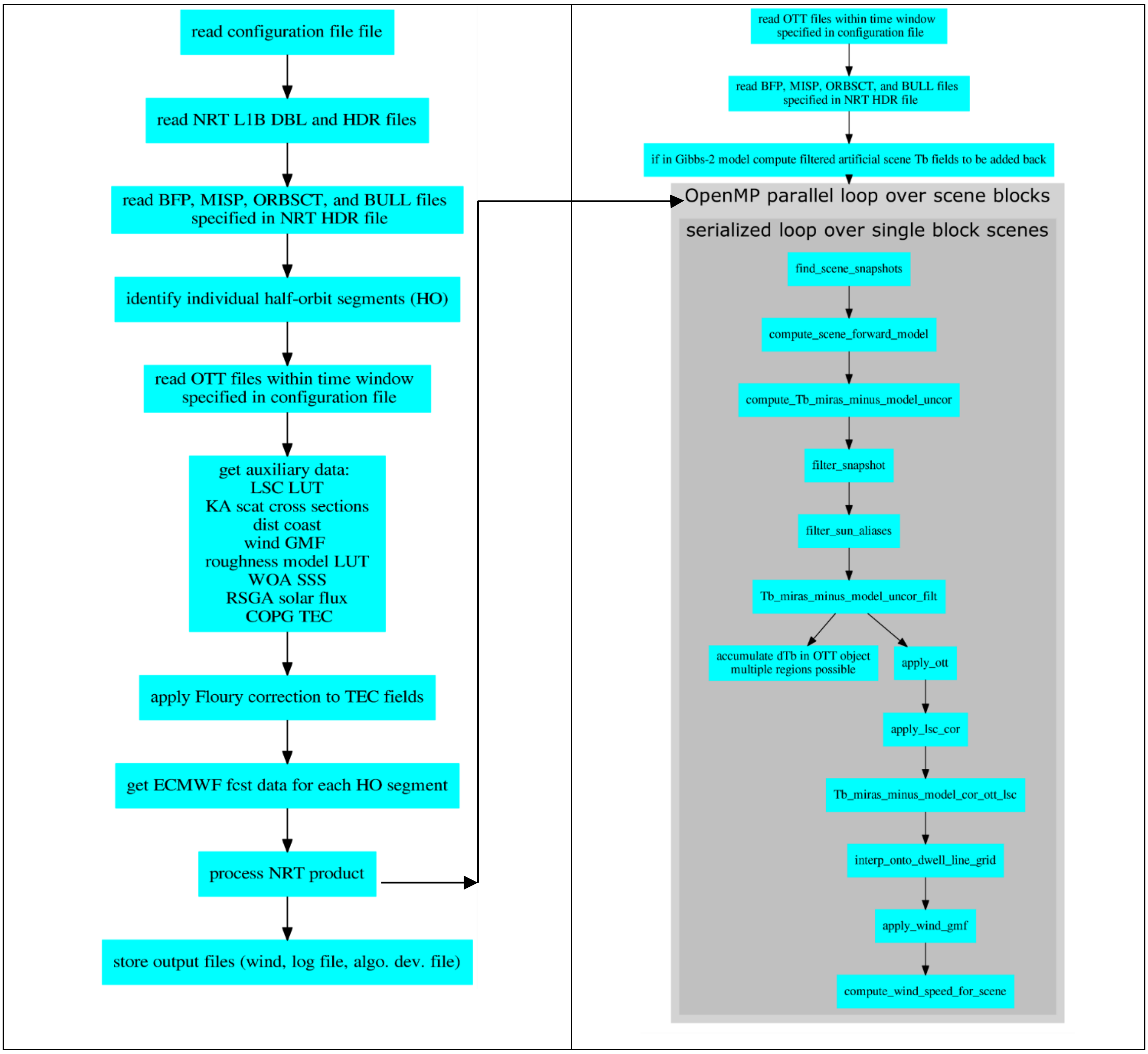

Figure 1: Schematic view of the SMOS NRT wind data processing flow

In the following document, we will describe in detail the algorithm and successive steps we used in our processing chain. It uses already many sub-processing steps existing in the SMOS Level 1B to Level 2 OS processings and ESL & CATDS breadboards. Nevertheless, several differences exists and each time a different processing is used, it will be detailed.

A dedicated algorithm is also provided (§4) to determine which of the NRT L2 swath data intercepts current storms and provide estimates of the wind radii per geographical sectors around the storm centers.

Finally, a simple algorithm describes (§5) how the processor generates the SMOS NRT Level 3 products which are daily composite of the Swath Level 2 wind data, splitted into ascending and descending passes.

2. From L1B Fourier components to brightness temperature scenes at antenna level

In this first processing step, we transform L1B Fourier components into brightness temperatures at the antenna level. The choice for the apodization window used in the inverse Fourier transform can be an important factor in the context of hurricane wind-speed retrieval as it impacts the spatial resolution. It therefore described here below.

2.1 From Fourier Space Level 1B to physical Space brigthness temperature

2.1.1 Rectangular DFT

Before moving into the description of the Fourier transform appropriate to MIRAS L1B Fourier components, we first review the discrete Fourier transform for functions that take their values on rectangular grids in two dimensions:

$$\hat{T}(q_1, q_2) = \mathrm{DFT}\{T(p_1', p_2')\} = \sum_{p_1'=0}^{N-1} \sum_{p_2'=0}^{N-1} T(p_1', p_2') e^{-\frac{2\pi i [p_1' q_1 + p_2' q_2]}{N}} \tag{2.1}$$

This is the forward transform of $T(p_1', p_2')$ from physical space to the Fourier domain, and $\hat{T}(q_1, q_2)$ is a generic brightness temperature Fourier component (with polarization unspecified for simplicity) at wavenumber (q_1, q_2). The inverse transform, from the Fourier to the physical domain, is computed within as:

$$N^2 T(p_1, p_2) = I\mathrm{DFT}\{\hat{T}(q_1', q_2')\} = \sum_{q_1'=0}^{N-1} \sum_{q_2'=0}^{N-1} \hat{T}(q_1', q_2') e^{\frac{2\pi i [p_1' q_1 + p_2' q_2]}{N}} \tag{2.2}$$

where (p_1, p_2) is a location in the physical domain. With respect to the ordering of data in the Fourier domain, in each dimension the positive frequencies are stored in the first half of the output and the negative frequencies are stored in backwards order in the second half of the output. In other words, the frequency -qi/N is the same as the frequency (N-qi)/N. All of the data fields are defined over the complete grids. In the case of the real brightness temperatures the Fourier components $\widehat{T_{xx}}(q_1, q_2)$ and $\widehat{T_{yy}}(q_1, q_2)$ are conjugate symmetric about the origin (q_1= 0; q_2 = 0) in the Fourier domain.

2.1.2 From the rectangular to the hexagonal DFT

The development below follows essentially that presented in [RD.24; RD.25]. The aim is to define the basis vector in Fourier and spatial domains over which the L1B inverse Fourier transform will be made. We begin by generalizing the discrete Fourier transform relations (2.1) and (2.2):

$$\hat{T}(\mathbf{u_q}) = \mathrm{DFT}\{T(\mathbf{x_p})\} = \sum_{\mathrm{p}\,\in\,\mathbb{G}_p} \sigma_x T(\mathbf{x_p})\, e^{-2\pi i[\mathbf{x_p}\cdot\mathbf{u_q}]} \tag{2.3}$$

and

$$T(\mathbf{x_p}) = I\mathrm{DFT}\{\hat{T}(\mathbf{u_q})\} = \sum_{\mathrm{q}\,\in\,\mathbb{G}_q} \sigma_u \hat{T}(\mathbf{u_q})\, e^{2\pi i[\mathbf{x_p}\cdot\mathbf{u_q}]} \tag{2.4}$$

where we have introduced sets of integer vectors $\mathbb{G}_p$ and $\mathbb{G}_q$ and associated coordinate vectors $\mathbf{x_p}$ in physical space and $\mathbf{u_q}$ in Fourier space. This is done with the aim of generalizing the domains over which the forward and inverse Fourier transforms act. By introducing mappings from the integer vectors to the coordinate vectors:

$$\mathbf{x_p} \quad = \quad \mathbf{x_p}(\mathbf{p}) = p_1\mathbf{x}^{(1)} + p_2\mathbf{x}^{(2)},\ \mathbf{p} = (p1,\, p2)T\ \ \in \mathbb{Z}^2, \tag{2.5}$$

$$\mathbf{u_q} \quad = \quad \mathbf{u_q}(\mathbf{q}) = q_1\mathbf{u}^{(1)} + q_2\mathbf{u}^{(2)},\ \mathbf{q} = (q1,\, q2)T\ \ \in \mathbb{Z}^2. \tag{2.6}$$

The basis vectors ($\mathbf{x}^{(1)}$, $\mathbf{x}^{(2)}$) and ($\mathbf{u}^{(1)}$, $\mathbf{u}^{(2)}$) and sets of integer vectors G$\mathbf{p}$ and G$\mathbf{q}$ must be chosen so that the Fourier transform relations (2.3) and (2.4) hold.

For the Y-shaped MIRAS array the visibility function is sampled on a hexagonal grid extending over a star-shaped region in Fourier space [RD.. It is thus natural to define this grid by establishing basis vectors which, when multiplied by integers, yield the gridpoint locations in a cartesian frame in the Fourier domain:

$$\mathbf{u}^{(1)} \quad = \quad \delta u(1,\, 0)^T, \tag{2.7}$$

$$\mathbf{u}^{(2)} \quad = \quad \delta u(-1/2,\, \sqrt{3/2})^T, \tag{2.8}$$

Here $\delta u = d/\lambda$, where d is the antenna spacing and λ is the radiation wavelength, and

$$\|\mathbf{u}^{(2)}\| = \delta u = d/\lambda \tag{2.9}$$

The infinite set of points corresponding to all possible integers ($q1$, $q2$) forms the hexagonal lattice

$$\mathcal{H} = \{\mathbf{u_q} = q_1\mathbf{u}^{(1)} + q_2\mathbf{u}^{(2)}\,, \qquad q = (q_2, q_2)^T\ \in \mathbb{Z}^2\} \tag{2.10}$$

Given the finite frequency coverage of MIRAS, it is necessary to select a subset of this lattice. The natural choice for the fundamental period of the hexagonal lattice is an hexagon just large enough to contain this frequency coverage. The hexagon is arranged so that two of its edges are bisected by the basis vectors $\mathbf{u}^{(1)}$and $\mathbf{u}^{(2)}$. The entire Fourier plane may be covered, without gaps, by an infinite tiling of these hexagons. The centers, or nodes, of these hexagons lie on another lattice:

$$N\mathcal{H} = \left\{\mathbf{U_q} = Q_1\mathbf{U}^{(1)} + Q_2\mathbf{U}^{(2)}\ ,\ q = (Q_1, Q_2)^T\ \in \mathbb{Z}^2\right\} \tag{2.11}$$

where the basis vectors for this lattice in a cartesian frame are:

$$\begin{aligned}\mathbf{U}^{(1)} &= N\mathbf{u}^{(1)}\\ \mathbf{U}^{(2)} &= N\mathbf{u}^{(2)}\end{aligned} \tag{2.12}$$

or some choice positive integer N which governs the size of each cell. For N = 64 the star-shaped frequency coverage of MIRAS, or *baseline star domain*, is completely contained within the primitive hexagonal cell $C(N\,H)$. More specifically the measured frequencies lie on the grid G$\mathbf{q}(N\,H)\delta u$, where

$$\mathbb{G}_q(N\mathcal{H}) = \left\{\,\mathbf{q} \in \mathbb{Z}^2\ :\ \mathbf{u_q}\ \in\ \mathcal{C}(N\mathcal{H})\right\} \tag{2.13}$$

In our algorithm, we choose N = 64 which is the smallest power of two that yields a hexagonal cell that contains the MIRAS coverage. The corresponding cell $N\mathcal{H}$ and the frequency coverage of MIRAS are shown in Fig. 2.

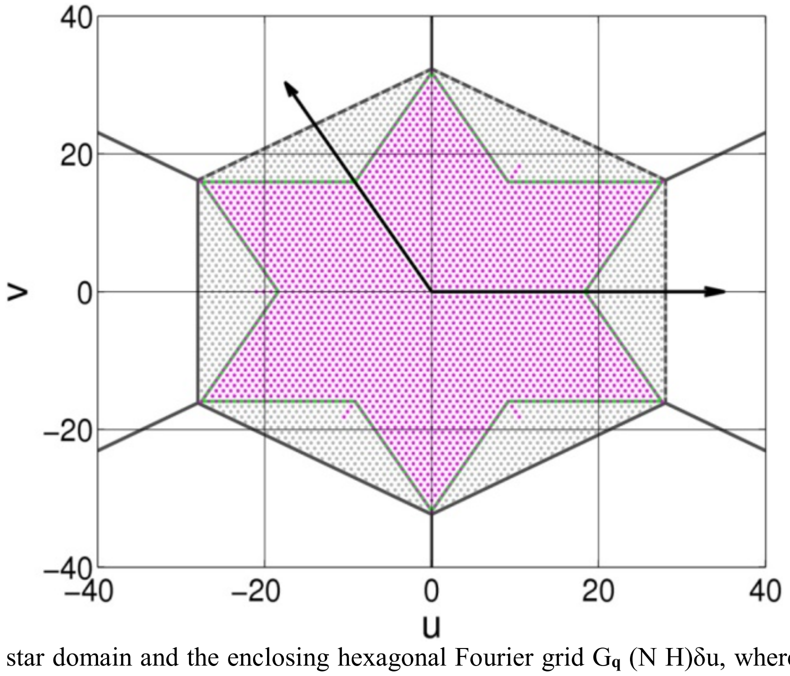

Figure 2: The baseline star domain and the enclosing hexagonal Fourier grid $G_{\mathbf{q}}$ (N H)δu, where the choice N = 64 has been made since this is the minimum power of two that completely encloses the spatial frequencies measured by MIRAS. With this choice for N , G**q** (N H)δu contains 4096 gridpoints. The vectors show the basis vectors for the hexagonal Fourier grid $\mathbf{u}^{(1)}$ and $\mathbf{u}^{(2)}$ reduced in scale to fit in the plot.

An inverse Fourier transform may be applied to the set of Fourier components defined over this grid to obtain brightness temperatures over some spatial grid within an elementary cell $\mathcal{C}(N^*)$ of some reciprocal lattice defined by:

$$\mathcal{H}^* = \left\{\mathbf{X_p} = P_1\mathbf{X}^{(1)} + P_2\mathbf{X}^{(2)}\ ,\qquad \mathbf{P} = (P_1, P_2)^T\ \in \mathbb{Z}^2\right\} \tag{2.14}$$

The spatial grid lies on a portion of the lattice:

$$\mathcal{H}^* = \{\mathbf{x_p} = p_1\mathbf{x}^{(1)} + p_2\mathbf{x}^{(2)}, \qquad \mathbf{p} = (p_1, p_2)^T \in \mathbb{Z}^2\} \tag{2.15}$$

defined by the set of integers:

$$\mathbb{G}_p(\mathcal{H}^*) = \{\, \mathbf{p} \in \mathbb{Z}^2 : \mathbf{x_p} \in \mathcal{C}(\mathcal{H}^*)\} \tag{2.16}$$

To find the form of this reciprocal physical space grid we begin by *insisting* that forward and inverse discrete Fourier transforms exist and take the form:

$$\hat{T}(\mathbf{u_q}) = \mathrm{DFT}\{T(\mathbf{x_p})\} = \sum_{\mathrm{p} \in \mathbb{G}_p(\mathcal{H}^*)} \sigma_x T(\mathbf{x_p})\, e^{-2\pi i[\mathbf{x_p}\cdot\mathbf{u_q}]} \tag{2.17}$$

and

$$T(\mathbf{x_p}) = \mathrm{IDFT}\{\hat{T}(\mathbf{u_q})\} = \sum_{\mathrm{q} \in \mathbb{G}_{q(N\mathcal{H})}} \sigma_u \hat{T}(\mathbf{u_q})\, e^{2\pi i[\mathbf{x_p}\cdot\mathbf{u_q}]} \tag{2.18}$$

where:

$$\mathbb{G}_p(\mathcal{H}^*)\delta\xi = \{\mathbf{x_p} = p_1\mathbf{x}^{(1)} + p_2\mathbf{x}^{(2)}, \qquad \mathbf{p} = (p_1, p_2)^T \in \mathbb{Z}^2\}$$

is some grid in physical space to be defined, and $\sigma_x = |\mathbf{x}^{(1)} \times \mathbf{x}^{(2)}|$ is the area of an elementary cell of a lattice on which the individual gridpoints of G$\mathbf{p}(H*)$ lie. Comparing (2.17) and (2.18) with (2.3) and (2.4), we see that (2.17) and (2.18) will hold if :

$$\begin{aligned} \sigma_x\sigma_u &= 1/N^2 \\ \mathbf{x_p}\cdot\mathbf{u_q} &= (\mathbf{p}\cdot\mathbf{q})/N = (p_1q_1 + p_2q_2)/N \end{aligned} \tag{2.19}$$

The condition (2.19) will be satisfied provided that:

$$\begin{aligned} \mathbf{x}^{(1)}\cdot\mathbf{u}^{(1)} &= 1/N, \\ \mathbf{x}^{(1)}\cdot\mathbf{u}^{(2)} &= 0, \\ \mathbf{x}^{(2)}\cdot\mathbf{u}^{(1)} &= 0, \\ \mathbf{x}^{(2)}\cdot\mathbf{u}^{(2)} &= 1/N, \end{aligned}$$

Referring to the definitions of the basis vectors $\mathbf{u}^{(1)}$ and $\mathbf{u}^{(2)}$ in (2.12), the requirement that $\mathbf{x}^{(1)}\cdot\mathbf{u}^{(2)} = 0$ is satisfied if:

$$\mathbf{x}^{(1)} = \alpha_1(0,0,1)^T \times \mathbf{u}^{(2)} = \alpha_1\delta u\left(-\sqrt{3}/2\,, 1/2\right)^T$$

for some choice of α_1. Now, in order to satisfy the condition $\mathbf{x}^{(1)}\cdot\mathbf{u}^{(1)} = 1/N$,

$$\alpha_1 \delta u\left(-\sqrt{3}/2\,,1/2\right)^T \cdot \mathbf{u}(1) = \alpha_1 \delta u\left(-\sqrt{3}/2\,,\frac{1}{2}\right)^T \cdot (1{,}0)^T = -\alpha_1(\delta u)^2\left(\sqrt{3}/2\right) = 1/N$$

and so:

$$\alpha_1 = -\left(\frac{2}{\sqrt{3}}\right)\left(\frac{1}{N(\delta u)^2}\right)$$

and therefore:

$$\mathbf{x}^{(1)} = (1/\delta u)\left(1/N\,,1/(N\sqrt{3})\right)^T = (1/\delta u)\left(\frac{2}{\sqrt{3}N}\right)\left(\sqrt{3}/2\,,1/2\right)^T = \delta\xi\left(\sqrt{3}/2\,,1/2\right)^T$$

where we have introduced the grid spacing of the grid G$\mathbf{p}(H*)$ in physical space:

$$\delta\xi = \left(\frac{2}{\sqrt{3}}\right)\left(\frac{1}{\delta u}\right)$$

In a similar manner, the requirement that $\mathbf{x}^{(1)} \cdot \mathbf{u}^{(2)} = 0$ is satisfied if:

$$\mathbf{x}^{(2)} = \alpha_2(0{,}0{,}1)^T \times \mathbf{u}^{(1)} = \alpha_2(0, \delta u)^T$$

for some choice of α_2. Now in order to satisfy the condition $\mathbf{x}^{(2)} \cdot \mathbf{u}^{(2)} = 1/N$,

$$\alpha_2(0{,}0{,}1)^T \cdot \left(-\delta u/2\,, -\delta u\sqrt{3}/2\right)^T = \alpha_2(\delta u)^2\left(\sqrt{3}/2\right) = 1/N$$

and so

$$\alpha_2 = \left(\frac{2}{\sqrt{3}}\right)\left(\frac{1}{N(\delta u)^2}\right)$$

and therefore

$$\mathbf{x}^{(2)} = \alpha_2(0, \delta u)^T = \left(\frac{2}{\sqrt{3}N}\right)\left(\frac{1}{\delta u}\right)(0{,}1)^T = \delta\xi(0{,}1)^T$$

To summarize the two reciprocal sets of basis vectors, we have in the Fourier domain the basis vectors:

$$\mathbf{u}^{(1)} = \delta u(1,\ 0)^T,$$

$$\mathbf{u}^{(2)} = \delta u(-1/2,\ \sqrt{3/2})^T,$$

and in the physical domain the basis vectors:

$$\mathbf{x}^{(1)} = \delta\xi\ (\sqrt{3/2}\ ,1/2)\,,$$

$$\mathbf{x}^{(2)} = \delta\xi(0{,}1),$$

with

$$\delta\xi = \left(\frac{2}{\sqrt{3}}\right)\left(\frac{1}{\delta u}\right)$$

The areas of the corresponding primitive rhombus-shaped cells are:

$$\sigma_x = \left|\mathbf{x}^{(1)} \times \mathbf{x}^{(2)}\right| = \frac{\sqrt{3}}{2}(\delta\xi)^2,$$

$$\sigma_u = \left|\mathbf{u}^{(1)} \times \mathbf{u}^{(2)}\right| = \frac{\sqrt{3}}{2}(\delta u)^2,$$

and the product of these two areas is:

$$\sigma_x\sigma_u = \left(\frac{\sqrt{3}}{2}\right)^2 (\delta\xi)^2(\delta u)^2 = \left(\frac{\sqrt{3}}{2}\right)^2 \left(\frac{2}{\sqrt{3}N}\right)^2 \left(\frac{1}{\delta u}\right)^2 (\delta u)^2 = \frac{1}{N^2},$$

which satisfies requirement (2.19) for the validity of the Fourier transform relationships (2.17) and (2.18) between the brightness temperature $T(\mathbf{x_p})$ and its Fourier transform $\hat{T}(\mathbf{u_q})$. The spatial grid G$\mathbf{p}$($H*$)$\delta\xi$ is shown in Fig. 3.

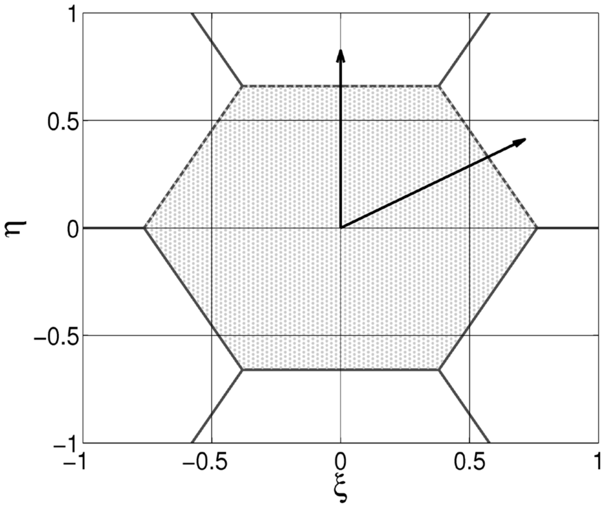

Figure 3: The physical space hexagonal grid Gp (H∗)δξ corresponding to the hexagonal Fourier grid Gq (N H)δu for N = 64. Like the Fourier grid, this grid contains 4096 gridpoints arranged in a hexagonal configuration. The basis vectors for this grid x(1) and x(2) have been reduced in scale to fit in the plot.

With the preceding definitions of the Fourier and physical space basis vectors the Fouriertransform relations (2.16) and (2.17) may be rewritten directly in terms of the sets of grid integers:

$$\hat{T}(\mathbf{u_q}) = \mathrm{DFT}\{T(\mathbf{x_p})\} = \sum_{\mathrm{p} \in \mathbb{G}_p(\mathcal{H}^*)} \sigma_x T(\mathbf{x_p})\, e^{-2\pi i(\mathbf{x_p}\cdot\mathbf{u_q})} \tag{2.20}$$

and

$$T(\mathbf{x_p}) = \mathrm{IDFT}\{\hat{T}(\mathbf{u_q})\} = \sum_{\mathrm{q} \in \mathbb{G}_{q(N\mathcal{H})}} \sigma_u \hat{T}(\mathbf{u_q})\, e^{2\pi i[\mathbf{q}\cdot\mathbf{p}]/N} \tag{2.21}$$

However, as noted in [RD.24; RD.25], the grids are not convenient for application of the fast Fourier transform to (2.20) and (2.21) owing to the definitions of the integer sets and G**p**($H*$) and G**q**. However, in [RD.24,RD.25] it is shown that the grid G**q** may be remapped onto the rhombus-shaped grid $\mathbb{G}'_{q'}$ in the manner illustrated in Figs. 4(a) and 4(b) with no change in the phase factor of the Fourier transform (because of periodicity). Likewise, the hexagonal physical space grid may be obtained from a rhombus-shaped grid in the manner shown in Figs. 5(a) and 5(b).

(a) (b)

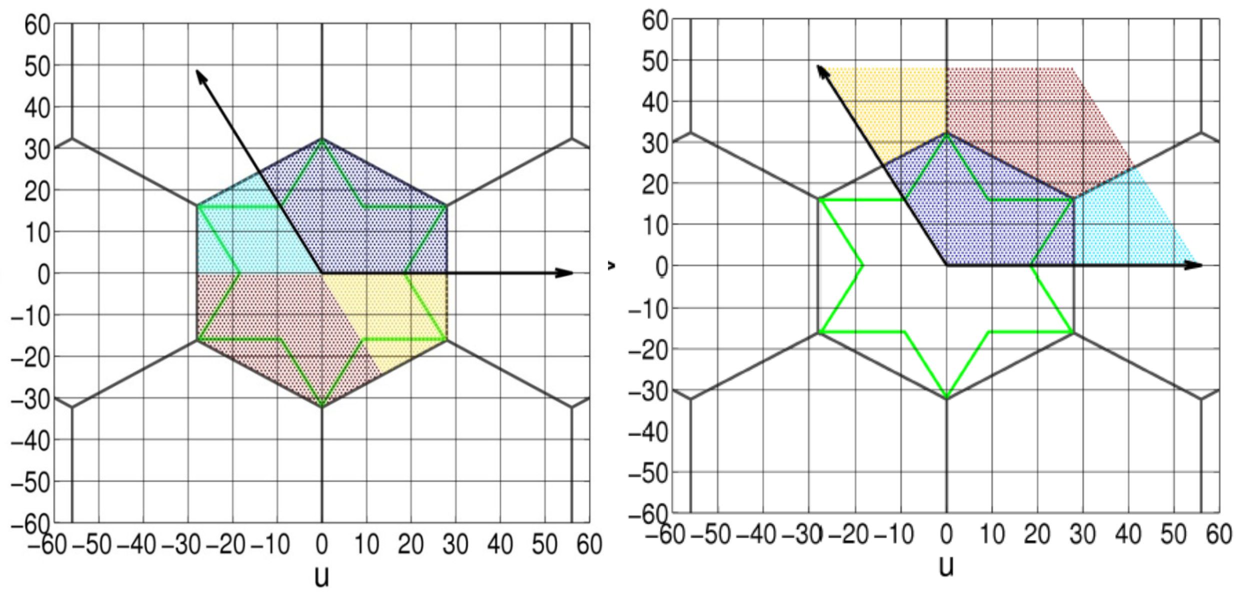

Figure 4: Graphical representation of the remapping of the spatial frequency grid G**q** ($N\ H)\delta u$ containing the MIRAS Fourier components. (a) UV-space hexagonal grid Gq (N H)δu. (b) UV-space hexagonal grid Gq (N H)δu remmaped to a rhombus-shaped grid UV-space hexagonal grid G'q (N H)δu

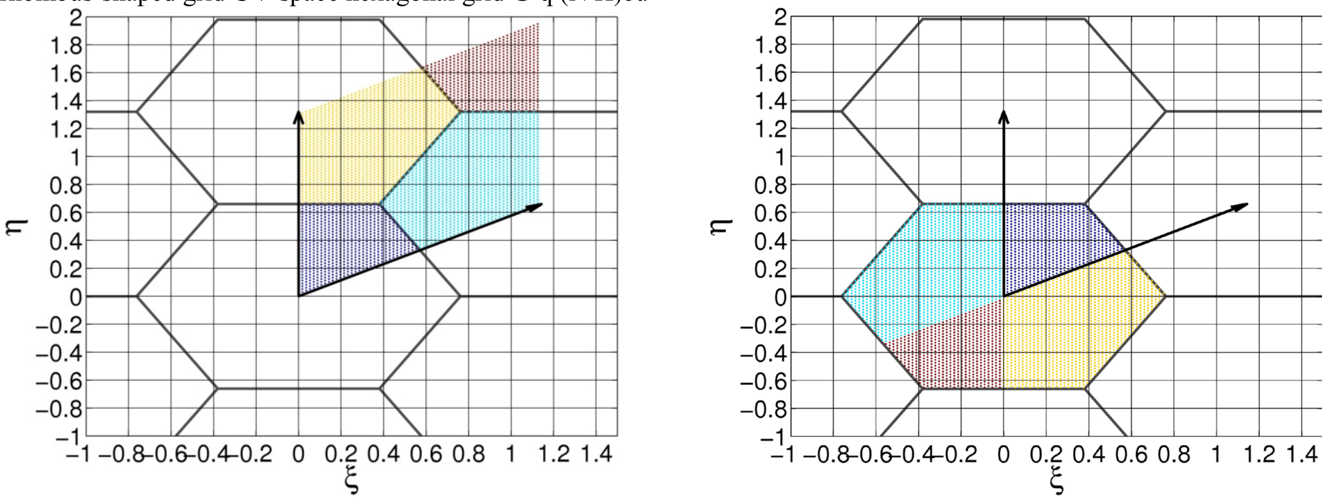

(a) physical space hexagon (director cosine coordinates) (b) physical space hexagon (director cosine coordinates)

Figure 5: Graphical representation of the remapping of the hexagonal spatial grid G**p** $(H*)\delta\xi$ into the rhombus-shaped grid G**p**, $(H*)\delta\xi$. As in Fourier space, the phase factor in the Fourier transform remains unchanged under the transformation of points between these two grids owing to the hexagonal periodicity. Colors indicate portions of the grids that are shifted by the same amount in ξ and η. The vectors show the basis vectors for the hexagonal spatial grid, $\mathbf{x}^{(1)}$ and $\mathbf{x}^{(2)}$ at their true scales.

2.1.3 The Spatial Filter

Recall that the inverse discrete Fourier transform of some function $\hat{T}(\mathbf{u_q})$ without a spatial filter is:

$$T(\mathbf{x_p}) = \mathrm{IDFT}\{\hat{T}(\mathbf{u_q})\} = \sum_{q\,\in\,\mathbb{G}_{q(N\mathcal{H})}} \sigma_u \hat{T}(\mathbf{u_q})\, e^{2\pi i[\mathbf{x_p}\cdot\mathbf{u_q}]}$$

With a spatial filter the Fourier components of $\hat{T}(\mathbf{uq})$ are weighted by a filter $\hat{W}(\mathbf{uq})$ so that:

$$\tilde{T}(\mathbf{x_p}) = \mathrm{IDFT}\{\hat{T}(\mathbf{u_q})\} = \sum_{q\,\in\,\mathbb{G}_{q(N\mathcal{H})}} \sigma_u \hat{W}(\mathbf{u_q})\hat{T}(\mathbf{u_q})\, e^{2\pi i[\mathbf{x_p}\cdot\mathbf{u_q}]}$$

where $\tilde{T}(\mathbf{x_p})$ denotes the filtered function in physical space. This filtering operation corresponds to a convolution between $T(\mathbf{x_p})$ and some weighting function $W(\mathbf{x_p})$, or WEF, in physical space:

$$\tilde{T}(\mathbf{x_p}) = \sum_{p'\,\in\,\mathbb{G}_p(\mathcal{H}^*)} \sigma_x W(\mathbf{x_p} - \mathbf{x_{p'}}) T(\mathbf{x_{p'}})$$

The physical space weighting function may be obtained by computing the inverse Fourier transform of $\hat{W}(\mathbf{u_q})$ using (2.18):

$$W(\mathbf{x_p}) = \mathrm{IDFT}\{\hat{W}(\mathbf{u_q})\} = \sum_{q\,\in\,\mathbb{G}_{q(N\mathcal{H})}} \sigma_u \hat{W}(\mathbf{u_q})\, e^{2\pi i[\mathbf{x_p}\cdot\mathbf{u_q}]}$$

Note that the product of the physical space area element σ_x and $W(\mathbf{x_p})$ sums to unity over the physical space hexagonal grid $\mathbf{Gp}(H*)\delta\xi$,

$$\sum_{p\,\in\,\mathbb{G}_p(\mathcal{H}^*)} \sigma_x W(\mathbf{x_p}) = 1$$

Here $\sigma_x = 1/(N^2\sigma_u)$ in accordance with (2.19). The forward discrete Fourier transform applied to this physical space weighting function is, from (2.17):

$$\hat{W}(\mathbf{u_q}) = \mathrm{DFT}\{W(\mathbf{x_p})\} = \sum_{p\,\in\,\mathbb{G}_p(\mathcal{H}^*)} \sigma_x W(\mathbf{x_p})\, e^{-2\pi i(\mathbf{x_p}\cdot\mathbf{u_q})}$$

so that$\hat{W}(\mathbf{u_q})$ and $W(\mathbf{x_p})$ are Fourier transform pairs. To emphasize the relative weighting given to brightness as a function of distance from synthetic boresight the function is normalized to a maximum of unity:

$$W_n(\mathbf{x_p}) = W(\mathbf{x_p})/\max(W(\mathbf{x_p}))$$

where for the filters considered here $\max(W(\mathbf{x_p})) = W(\mathbf{0})$

In what follows the spatial filters have been modified to incorporate the intrinsic frequency cutoff im- posed by the instrument which provides measurements only inside the star shaped experimental frequency coverage H rather than over some hexagonal domain in Fourier space [RD.24]. However, without any further filtering, the sharp frequency cutoff at the edge of H can produce significant ripples in the reconstructed images.

The spatial filter used here by default is the approximate Blackman filter [RD.24]:

$$\widehat{W}^b(\mathbf{u_q}) = \begin{cases} 0.42 + 0.5\cos\pi\left(\dfrac{|\mathbf{u_q}|}{u_{max}}\right) + 0.08\cos 2\pi\left(\dfrac{|\mathbf{u_q}|}{u_{max}}\right) & \text{for } \mathbf{u_q}\ inside\ \mathcal{H} \\ 0 & \text{otherwise} \end{cases} \tag{2.22}$$

Here the normalization u_{max} is chosen such that the amplitude of the filter drops to zero at some distance from the origin. By default in our processing chain, this radius corresponds to the maximum frequency resolved by the instrument (i.e., the tip of the stars in the baseline star frequency coverage), so that:

$$u_{max} = u_{max}^{b1} = 21\sqrt{3}\delta u = 21\sqrt{3}(.875) \approx 31.8264$$

This one-dimensional Blackman star filter is shown as a function of the distance from the origin $\sqrt{u^2 + v^2}$ in Fig. 6(a).

Insight into the corresponding footprint may be gained by examination of the corresponding azimuthally-averaged normalized weighting function $Wn(\mathbf{xp})$ which is shown by the red curve in Fig. 6(b). The weighting function is quite symmetric, since the azimuthal maximum, if $Wn(\mathbf{xp})$ is not significantly larger that the mean, and both the mean and maximum drop to near zero about 50 km from synthetic boresight. Also, about 75% of the total brightness temperature of a uniform scene is associated with brightness within 25 km of the synthetic boresight, as shown by the blue curve in the same figure.

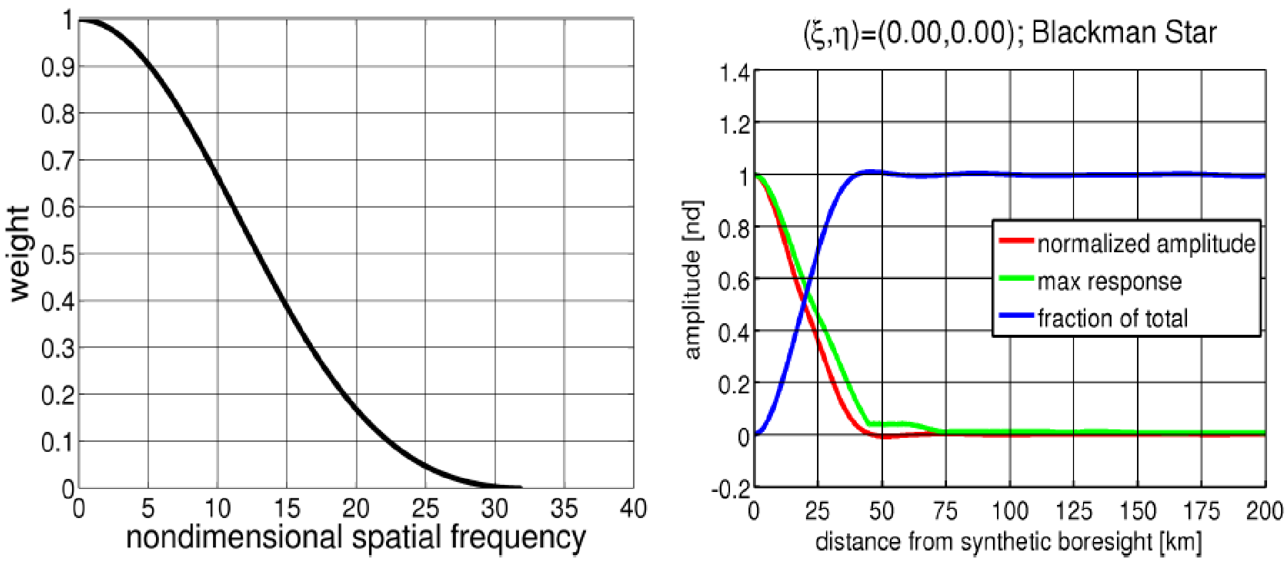

(a) Blackman filter in Fourier Space (b) Weighting function in physical Space

Figure 6: (a) the isotropic Blackman spatial filter used in our algorithm to create images of brightness temperature from their Fourier components; (b) Profiles of the corresponding spatial weighting function as a function of distance from synthetic boresight at $(\xi, \eta) = (0, 0)$. The red curve shows the WEF amplitude normalized to a maximum of unity at synthetic boresight center; the green curve shows the maximum normalized amplitude at each radius; The blue curve shows the WEF integrated outward from the synthetic boresight center and shows, in the case of a uniform brightness temperature scene, the fraction of the total synthetic beam brightness temperature accounted for by brightness within a given radius

2.2 The scene assembly at the antenna level

SMOS instrument is not measuring both linear polarization (XX) and (YY) at the same acquisition time. In dual polarization mode the Level 1B brightness temperature frequencies are delivered sucessively in XX and YY polarisations (namely T_{xx} and T_{yy}) every Δt=1.2 ms, the instrument integration time. In full polarisation mode, visibilities are acquired following a complex temporal cycle of rotating polarizations. To build up a First Stokes parameter, we therefore combined successively acquired linearly polarized data following a "scene" concept. In that concept, we basically assume that successively acquired linear polarization correspond to the same brightness temperature scene (neglecting the antenna boresight displacement over Δt).

In dual polarization mode, a scene is defined by the combination of two successive snaphots separated by the the instrument integration time Δt, so that the the two successively polarized brightness images are assembled at the antenna level to form a scene indexed number "i" :$scene_i$ corresponding to a "mean" aquisition time t_i of a scene and obtained following:

$$scene= [T_{xx}\ (\xi, \eta, t_i);\ T_{yy}\ (\xi, \eta, t_i + \Delta t)\ ] \qquad (2.23)$$

In full polarization mode, the Level 1B brightness temperature frequencies are delivered in the following order:

Receivers in all arms in X-pol for 1.2 s:
1) XX-long

Receivers in X-pol in 2 arms and in Y-pol in the third arm rotating for 1.2 s:
2) XX-short
3) XY-real
4) XY-imaginary

Receivers in all arms in Y-pol for 1.2 s:
5) YY-long

Receivers in Y-pol in 2 arms and in X-pol in the third arm rotating for 1.2 s:
6) YY-short
7) XY-real
8) XY-imaginary

To deal with the complexity of the SMOS polarimetric information in full polarization mode, we introduce the 'scene' here consists of a collection of 4 snapshots yielding the complete Stokes vector (XX,YY,XYR,XYI).

The individual snapshots corresponding to a given complete Stokes vector scene may be obtained from an index mappings, which provide the set of snapshot indices for each scene index. These scene index mappings are stored in a snapshots substructure within each analysis file.

Our algorithm reads the Level 1B DBL file and loops through all snapshots in the order in which they appear in the file. The snapshots are assumed to be in order of increasing time.

The code reads successive snapshots until a complete Stokes vector is obtained, without regard to whether or not particular snapshots correspond to mixed or pure polarization modes of the instrument. As each snapshot is read, any snapshot already read that is being considered to be part of the next complete Stokes vector is discarded if the time difference between this snapshot and the one just read exceeds 5 seconds.

In this manner complete Stokes vector scenes consisting of successive snapshots are created. Note that, given the typical ordering of snapshots in the data files, each scene will typically consist of either a mixed of short integration time-XX, long-integration time YY and mixed real and imaginary part for XY snapshot, or, a mixed of long integration time –XX, short-integration time YY and mixed real and imaginary part for XY snapshot.

3. Surface Wind Speed Retrieval from Antenna Tbs

The process of retrieving the surface wind speed from MIRAS-derived brightness temperatures consist in first estimating the residual brightness temperature contrasts which are induced by the wind-generated roughness and foam formations at the sea surface. To do so, the reconstructed MIRAS brightness temperature images are best corrected from all other contributions to the signal using a radiative transfer forward emissivity model forced by auxilliary geophysical data describing the observed scene. These contributions are estimated using semi-empirical electromagnetic models and include the Faraday rotation across the ionosphere, the atmospheric effects, the sea-surface scattered sky and solar radiation contributions, and the near surface thermo-haline condition impacts on the sea surface specular emission. The sum of the previously listed forward model contributions is estimated at antenna level and substracted to the reconstructed MIRAS Tb corrected for image biases and Land-Sea contamination to derive an estimation of the residual wind/wave/foam-driven brightness temperature contrasts. These steps are followed by the inversion of the residual Tb contrasts in surface wind speed using the so-called « wind Geophysical Model Function (GMF) ». The GMF we use is a monotonic function of wind speed combining two models : (1) the Yin et al. (2016) model for the low to moderate wind conditons (surface wind speed<12 m/s) and (2) the quadratic function of wind speed at high winds as derived by Reul et al. (2012; 2016).

We describe in §3.1 the definition for all the contributing terms and quantities that are used in the algorithm, detailed in §3.2.

3.1 Definitions

Table 3: nomenclature

Notation	Definition
τ_d	1-way atmosphereic transmittance associated with molecular oxygen absorption [nd]
τ_v	1-way atmosphereic transmittance associated with water vapor absorption [nd]
T_{esh}	H-pol brightness temperature of specular emission (surface pol. Basis) [K]
T_{erh}	H-pol brightness temperature of rough surface emission (surface pol. Basis) [K]
T_{sch}	H-pol brightness temperature of scattered celestial sky radiation (surface pol. Basis) [K]
T_{ssh}	H-pol brightness temperature of scattered solar radiation (sunglint) (surface pol. Basis) [K]
T_{esv}	V-pol brightness temperature of specular emission (surface pol. Basis) [K]
T_{erv}	V-pol brightness temperature of rough surface emission (surface pol. Basis) [K]
T_{scv}	V-pol brightness temperature of scattered celestial sky radiation (surface pol. Basis) [K]
T_{ssv}	V-pol brightness temperature of scattered solar radiation (sunglint) (surface pol. Basis) [K]
T_{ea}	Unpolarized brightness temperature of atmospheric 1-way emission [K]
R_h	Fresnel power reflection coefficient at the surface in H-pol
R_v	Fresnel power reflection coefficient at the surface in V-pol
e_{rh}	Rough surface emissivity in H-pol
e_{rv}	Rough surface emissivity in V-pol

T_{erU}	Third Stokes brightness temperature of rough surface emission (surface pol. Basis) [K]
T_{erV}	Fourth Stokes brightness temperature of rough surface emission (surface pol. Basis) [K]
F_f	Fractionnal area of sea surface covered by foam [nd]
T_s	Sea Surface Temperature [K]
w_r	10-m height Sea surface wind speed modulus [m/s]

3.2 Overview of the wind Retrieval Algorithm

Considering all components of the scene brightness temperature at L-band, the complete model solution for the upwelling brightness temperatures above the atmosphere but below the ionosphere (before Faraday rotation) in the surface polarization basis, is, in horizontal polarization:

$$T_{th}^{(full)} = (\tau_d\tau_v)[T_{esh} + T_{sch} + T_{ssh} + R_h T_{ea}] + T_{ea} + (\tau_d\tau_v)\left[(1 - F_f)T_{erh} - F_f T_{esh} - e_{rh}T_{ea}\right]$$

and in vertical polarization:

$$T_{vh}^{(full)} = (\tau_d\tau_v)[T_{esv} + T_{scv} + T_{ssv} + R_v T_{ea}] + T_{ea} + (\tau_d\tau_v)\left[(1 - F_f)T_{erv} - F_f T_{esv} - e_{rv}T_{ea}\right]$$

The terms in blue indicate the rough and foamy surface induced brightness-temperature contrasts. The only contribution in this model to the third and fourth Stokes parameters in the surface polarization basis comes also from the rough surface emission component, so that:

$$T_{tU}^{(full)} = (\tau_d\tau_v)T_{erU}$$

and

$$T_{tV}^{(full)} = (\tau_d\tau_v)T_{erV}$$

The full model solution for the first Stokes parameter, $T_{th}^{(full)} + T_{tv}^{(full)}$ is given as follows with the rough and foamy surface emission terms replaced by the GMF used for the wind retrieval (in red):

$$T_{th}^{(full)} + T_{tv}^{(full)} = (\tau_d\tau_v)[T_{esh} + T_{sch} + T_{ssh} + R_h T_{ea} + T_{esv} + T_{scv} + T_{ssv} + R_v T_{ea}] + 2T_{ea} + T_s GMF(w_r)$$

where w_r is the surface wind speed to be retrieved. The GMF is invertible over the full range of wind speeds, so that w_r can be retrieved if the value of $GMF(w_r)$ is known. In particular,

$$GMF(w_r) = \frac{1}{T_s}\ [T_{th}^{(full)} + T_{tv}^{(full)} - (\tau_d\tau_v)[T_{esh} + T_{sch} + T_{ssh} + R_h T_{ea} + T_{esv} + T_{scv} + T_{ssv} + R_v T_{ea}] - 2T_{ea}$$

so

$$w_r = GMF^{-1}\left\{\frac{1}{T_s}\left[T_{th}^{(full)} + T_{tv}^{(full)} - (\tau_d\tau_v)[T_{esh} + T_{sch} + T_{ssh} + R_h T_{ea} + T_{esv} + T_{scv} + T_{ssv} + R_v T_{ea}] - 2T_{ea}\right]\right\}$$

For convenience, the preceeding argument to the inverse of the GMF is denoted as:

$$\Delta e_{s1} = \frac{1}{T_s}\left[T_{th}^{(full)} + T_{tv}^{(full)} - (\tau_d \tau_v)[T_{esh} + T_{sch} + T_{ssh} + R_h T_{ea} + T_{esv} + T_{scv} + T_{ssv} + R_v T_{ea}] - 2T_{ea}\right]$$

and the retrieved wind becomes:

$$w_r = GMF^{-1}(\Delta e_{s1})$$

In the retrieval algorithm, $T_{th}^{(full)} + T_{tv}^{(full)}$ are the bias-corrected brightness temperatures obtained from MIRAS reconstruction algorithm, where the Bias Correction (BC) terms includes both the Ocean Target Transformation (OTT) and the Land Sea Contamination (LSC) corrections (see §3.3):

$$\Delta T_p^{BC}(\xi,\eta) = \Delta T_p^{OTT}(\xi,\eta) + \Delta T_p^{LSC}(\xi,\eta)$$

so that:

$$T_{th}^{(full)}(\xi,\eta) + T_{tv}^{(full)}(\xi,\eta) \rightarrow \left[T_x^{miras}(\xi,\eta) + T_y^{miras}(\xi,\eta)\right] - \left[T_x^{BC}(\xi,\eta) + T_y^{BC}(\xi,\eta)\right]$$

The resulting residual emissivity maps are functions of director cosine coordinates, so:

$$\Delta e_{s1} = \Delta e_{s1}(\xi,\eta)$$

The resulting maps are interpolated onto the final latitude-longitude analysis grid to obtain:

$$\Delta e_{s1}^{(i)} = \Delta e_{s1}^{(i)}(lat,lon)$$

Where the superscript *i* is the scene index for a given analysis gridpoint. The inverse GMF is applied to the individual scene residual emissivities:

$$\mathrm{w}_r^{(i)}(lat,lon) = GMF^{-1}\left\{\Delta e_{s1}^{(i)}(lat,lon)\right\}$$

After the entire NRT product is processed, the final retrieved wind speed is obtained by averaging the individual scene retrieved wind speeds $\mathrm{w}_r^{(i)}$:

$$w_r(lat,lon) = \langle \mathrm{w}_r^{(i)}(lat,lon)\rangle_{i=1..n}$$

where *n* is the number of individual winds observed at a given grid node (lat,lon).

New: The direct inversion method was used for the first version of the SMOS wind products (v2.0). However, it does not facilitate the introduction of constraints on the retrieved wind speed. The MIRAS measurements are sufficiently noisy that in low roughness conditions the weighted average excess emission can be negative, in which case the direct method yields negative wind speeds. To avoid this issue and to allow the introduction of additional a priori information on surface wind speed, a new wind retrieval method has been introduced for the products v3.0 and is described in details in section 3.6. In this Bayesian approach, the posterior distribution of the retrieved wind speed is taken to be the product of the likelihood function $\mathcal{L}$ and a prior distribution *P* based on ECMWF forecasts wind speed:

$$\widehat{w_r} = arg_{\widetilde{w}} max\ P\left(\widetilde{w}\middle|\boldsymbol{T_p},\boldsymbol{\theta_i};\sigma,w_p\right)$$

3.3 Bias Corrections applied to the Brightness temperatures

In the retrieval algorithm, $T_{th}^{(full)} + T_{tv}^{(full)}$ are the bias-corrected brightness temperatures obtained from MIRAS reconstruction algorithm, where the Bias Correction (BC) terms includes both the Ocean Target Transformation (OTT) and the Land Sea Contamination (LSC) corrections:

$$\Delta T_p^{BC}(\xi,\eta) = \Delta T_p^{OTT}(\xi,\eta) + \Delta T_p^{LSC}(\xi,\eta)$$

We detail how both $\Delta T_p^{OTT}(\xi,\eta)$ and $\Delta T_p^{LSC}(\xi,\eta)$ are obtained in the following sections.

3.3.1 Ocean Target Transformation

Brightness temperatures derived from MIRAS measurements are biased relative to the forward model. In general, the bias is a function of position in the field of view and time. Without loss of generality, this bias can be separated into three components as follows (for polarization p):

$$\Delta T_p(\xi,\eta,t) = \langle \Delta T_p \rangle_{t_f}(\xi,\eta,t_s) + \langle \Delta T_p \rangle_{\xi,\eta}(t_s,t_f) + \Delta T_p(\xi,\eta,t_s,t_f)$$

Where the fast time t_f corresponds to variations within a single orbit while the slow time t_s refers to variations on longer time scales. The term in red corresponds to the usual Ocean Target Transformation (OTT) as defined in the SMOS Level 2 processor ATBD [RD.12]. Note that the fast time scale variation also varies on the slow time to account for the fact that the orbital bias variation depends upon the time of year. The bias is computed as the difference between the brightness temperatures derived from MIRAS measurements and those obtained from the scene brightness model (in the instrument polarization basis):

$$\Delta T_p(\xi,\eta,t) = T_p^{miras}(\xi,\eta,t) - T_{tp}^{(full)}$$

The purpose of the OTT is to remove the component of the bias that varies arbitrarily over the field of view but slowly in time, so that:

$$\Delta T_p^{OTT}(\xi,\eta,t_s) = \langle \Delta T_p \rangle_{t_f}(\xi,\eta,t_s)$$

where p is the polarization in the instrument polarization basis. As the OTT varies as function of the slow time, it must be computed using data within some time window around the time for which this OTT is to be used. This time window is a configurable option in the wind processor.

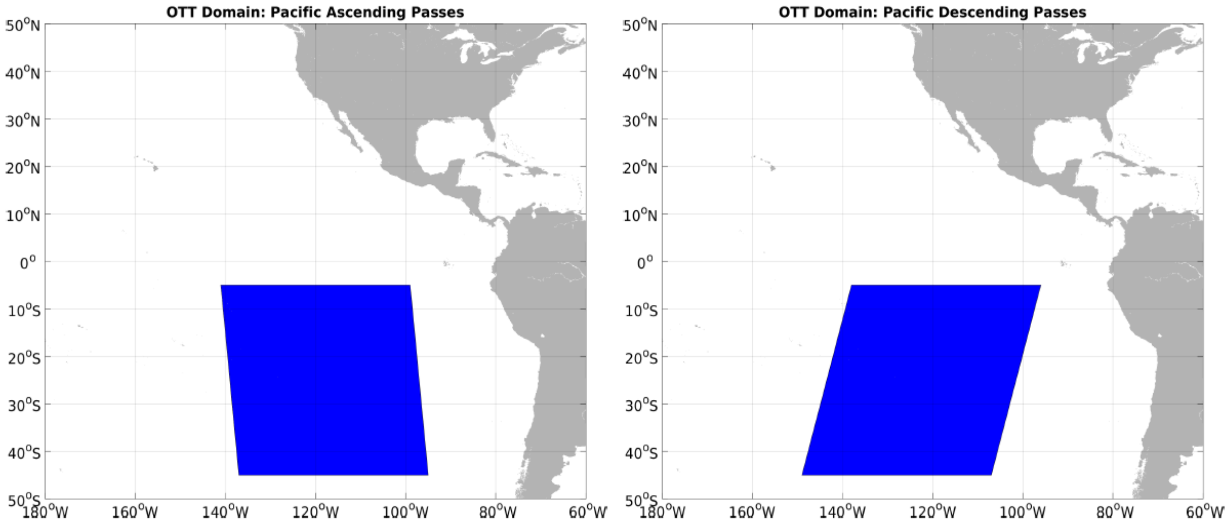

(a) OTT Domain Ascending Passes (b) OTT Domain Descending Passes

Figure 7: spatial domains used for evaluating the OTT in (a) ascending and (b) descending passes.

The OTTs for individual products are stored as one file per product with asc and desc pass OTTs stored as separate records. The OTTs are computed using only data with boresight positions (on the earth surface) in the blue regions shown in Fig. 7.

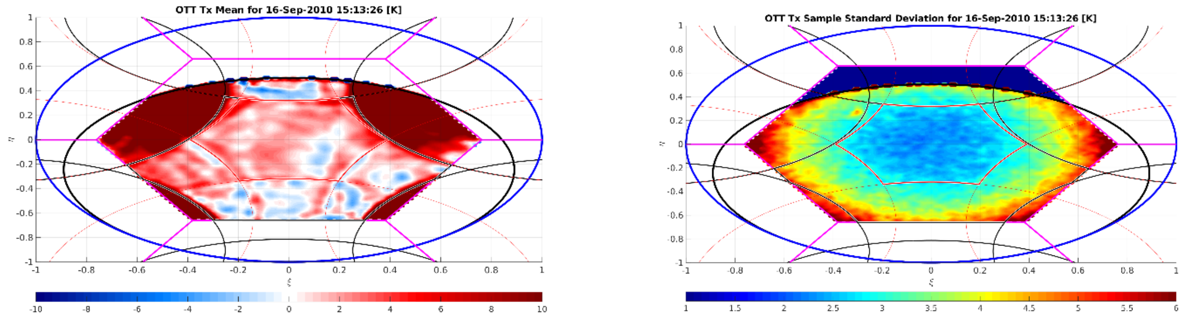

Figure 8. Examples of the OTT in x-polarisation for the 16-Sep 2010 (a) Mean and (b) Standard deviation.

3.3.2 Land Sea Contamination correction

In the present algorithm we use exactly the same Land Sea contamination correction than the one described in detail in the SMOS Level 2 ocean salinity algorithm [see RD. 12, ANNEX-5: Land (Mixed Scene) Contamination Correction]. Therefore, we do not duplicate the ATBD here and the reader is refered to [RD.12]. This empirical correction is expressed as a function of polarization p, the pass direction D, the geographic longitude and latitude and the director cosine coordinates:

$$\Delta T_p^{LSC}(\xi,\eta)=\Delta T_p^{LSC}(D,lat,lon,\xi,\eta)$$

3.4 Forward emissivity model contributions

As expressed above, the algorithm evaluate the residual wind/wave/foam induced emissivity as follows:

$$\Delta e_{s1} = \frac{1}{T_s}\left[T_{th}^{(full)} + T_{tv}^{(full)} - (\tau_d\tau_v)[T_{esh} + T_{sch} + T_{ssh} + R_h T_{ea} + T_{esv} + T_{scv} + T_{ssv} + R_v T_{ea}] - 2T_{ea}\right]$$

where $T_{th}^{(full)} + T_{tv}^{(full)}$ are the bias-corrected MIRAS Tbs and where the other contributions are estimate using a forward radiative transfer model, which include:

- T_{esp}: the specular sea surface emission at polarization p (§3.4.1)
- T_{ssp}: the sea surface scattered solar radiation (§3.4.2)
- T_{scp}: the sea surface scattered celestial sky radiation (§3.4.3)
- τ_d: the 1-way atmospheric transmittance associated with molecular oxygen absorption (§3.4.4)
- τ_v: the 1-way atmospheric transmittance associated with water vapor absorption (§3.4.4)
- T_{ea}: the unpolarized brightness temperature of atmospheric 1-way emission (§3.4.4)

We successively detail the forward models used for each of these contributions in the following paragraphs as indicated in parenthesis in the list above.

3.4.1 Specular sea surface Emission contribution

For a perfectly flat ocean surface the scattered electric and magnetic fields may be expressed in terms of the incident fields. The reflected electric field components (E'_h, E'_v) are related to the incident components (E_h, E_v) by the diagonal matrix equation:

$$\begin{pmatrix} E'_h(\theta_s, \phi_s) \\ E'_v(\theta_s, \phi_s) \end{pmatrix} = \begin{pmatrix} R_{hh}^{(0)} & 0 \\ 0 & R_{vv}^{(0)} \end{pmatrix} \begin{pmatrix} E_h(\theta_s, \phi_s - 180°) \\ E_v(\theta_s, \phi_s - 180°) \end{pmatrix}$$

where (θ_s, ϕ_s) is the specular reflection direction for radiation indicdent from direction $(\theta_s, \phi_s - 180°)$. The superscripts on the reflection coefficients indicate that they correpond to zero order expansion in surface slope, i.e., the flat surface reflection. The flat surface reflection coeffcients on the preceding matxix are given by the Fresnel equations:

$$R_{hh}^{(0)}(S, T_s, \theta_s) = \frac{\cos\theta_s - \sqrt{\epsilon_{sw}(S, T_s) - \sin^2\theta_s}}{\cos\theta_s + \sqrt{\epsilon_{sw}(S, T_s) - \sin^2\theta_s}}$$

$$R_{vv}^{(0)}(S, T_s, \theta_s) = \frac{\epsilon_{sw}(S, T_s)\cos\theta_s - \sqrt{\epsilon_{sw}(S, T_s) - \sin^2\theta_s}}{\epsilon_{sw}(S, T_s)\cos\theta_s + \sqrt{\epsilon_{sw}(S, T_s) - \sin^2\theta_s}}$$

Where $\epsilon_{sw}(S, T_s)$ is the dielectric constant for seawater given by the Klein and Swift model (1977) [RD.13] was used for SMOS NRT wind product v2.0, which is a function of the surface salinity S in practical salinity units (psu) and the temperature T_s in kelvin. For the version v3.0 products, a change has been applied to both the reprocessing and near real time products, involves use of the dielectric model described in [RD.33] to compute the specular emission (rather than the model of Klein and Swift [RD.13]).

The Fresnel reflection matrix equation is:

$$T' = \begin{pmatrix} T'_h \\ T'_v \\ U' \\ V' \end{pmatrix} = M^{(0)}T = \begin{pmatrix} \left|R_{hh}^{(0)}\right|^2 \delta^2 & 0 & 0 & 0 \\ 0 & \left|R_{vv}^{(0)}\right|^2 \delta^2 & 0 & 0 \\ 0 & 0 & \Re\left\{R_{hh}^{(0)}\left(R_{vv}^{(0)}\right)^*\right\} & \Im\left\{R_{hh}^{(0)}\left(R_{vv}^{(0)}\right)^*\right\} \\ 0 & 0 & -\Im\left\{R_{hh}^{(0)}\left(R_{vv}^{(0)}\right)^*\right\} & \Re\left\{R_{hh}^{(0)}\left(R_{vv}^{(0)}\right)^*\right\} \end{pmatrix} \begin{pmatrix} T_h \\ T_v \\ U \\ V \end{pmatrix}$$

The Fresnel power reflection coefficients are thus:

$$\left|R_{hh}^{(0)}(S, T_s, \theta_s)\right|^2 = \left|\frac{\cos\theta_s - \sqrt{\epsilon_{sw}(S, T_s) - \sin^2\theta_s}}{\cos\theta_s + \sqrt{\epsilon_{sw}(S, T_s) - \sin^2\theta_s}}\right|^2$$

$$\left|R_{vv}^{(0)}(S, T_s, \theta_s)\right|^2 = \left|\frac{\epsilon_{sw}(S, T_s)\cos\theta_s - \sqrt{\epsilon_{sw}(S, T_s) - \sin^2\theta_s}}{\epsilon_{sw}(S, T_s)\cos\theta_s + \sqrt{\epsilon_{sw}(S, T_s) - \sin^2\theta_s}}\right|^2$$

For typical ocean values of SST (0°-38°C) and SSS (20-40 psu), the sensitivity of the flat sea surface reflectivity at L-band (terms $\left|R_{pp}^{(0)}(\epsilon_{sw}, \theta_s)\right|^2$) to SSS varies from about 0.5 x 10^{-3} psu^{-1} to 3.5 x 10^{-3} psu^{-1} and its sensitivity to SST vary from about 0.2×10^{-3} °C^{-1} to 2×10^{-3} °C^{-1}, considering both linear polarizations and all incidence angles between 0° and 60°.

The specular emission in horizontal polarization is then:

$$T_{esh}(S, T_s, \theta_s) = T_{esh}(\epsilon_{sw}(S, T_s), T_s, \theta_s) = T_s\left[1 - \left|R_{hh}^{(0)}(\epsilon_{sw}, \theta_s)\right|^2\right]$$

and in vertical polarization:

$$T_{esv}(S, T_s, \theta_s) = T_{esv}(\epsilon_{sw}(S, T_s), T_s, \theta_s) = T_s\left[1 - \left|R_{vv}^{(0)}(\epsilon_{sw}, \theta_s)\right|^2\right]$$

3.4.2 Sun glint contribution

At the surface, the brightness temperature of the scattered solar radiation in polarization *p* may be expressed as (Reul et al., 2007 [RD.14]):

$$T_{ssp} = (\tau_d \tau_v) \frac{\bar{T}_{sun}(t)\Omega_{sun}}{4\pi \cos(\theta_s)} \left[\sigma_{pp}\left(\theta_o, \phi_o, \theta_s, \phi_s\right) + \sigma_{pq}\left(\theta_o, \phi_o, \theta_s, \phi_s\right)\right]$$

where $\bar{T}_{sun}(t)$ is the brightness temperature of the sun averaged over the solar disc at 1.4 GHz and at time t, Ω_{sun}=8.2 x 10^{-5} sr is the solid angle of the sun at L-band, p and q represent the polarizations H or V, and $(\sigma_{pp}, \sigma_{pq})$ are the bistatic scattering cross-sections of the rough sea surface, expressed as functions of the scattering geometry. The incidence and azimuth angles from the scattering surface toward the sun are θ_o and ϕ_o, respectively, and the corresponding angles towards the satellite are θ_s and ϕ_s. Atmospheric attenutaion on the downward path from the sun to the sea surface is accounted for by the factor $\tau_d \tau_v$ expressed in §3.4.4.

The Kirchhoff Approximation (KA) is used to model the bistatic scattering coefficients $\sigma^0_{\alpha\alpha_o}$ fro scattering of the incoming plane waves of polarization α_o into the outgoing plane waves of polarization α:

$$\sigma_{\alpha\alpha_o}(\boldsymbol{k_s}, \boldsymbol{k_o}) = \frac{1}{\pi} \left| \frac{2q_s q_o}{q_s + q_o} B_{\alpha\alpha_o}(\boldsymbol{k_s}, \boldsymbol{k_o}) \right|^2 e^{-(q_s+q_o)^2 \rho(0,0)} \cdot I_K$$

where $\boldsymbol{k_o}$ and $\boldsymbol{k_s}$ are the incident and scattered radiation wavenumber vectors, respectively, and, can be expressed in component form as:

$$\boldsymbol{k_o} \;\; /k = \left(\sin\theta_o \cos\phi_o\right)\hat{\boldsymbol{x}} + \left(\sin\theta_o \sin\phi_o\right)\hat{\boldsymbol{y}} + (\cos\theta_o)\hat{\boldsymbol{z}}$$

$$\boldsymbol{k_s} \;\; /k = \left(\sin\theta_s \cos\phi_s\right)\hat{\boldsymbol{x}} + \left(\sin\theta_s \sin\phi_s\right)\hat{\boldsymbol{y}} + (\cos\theta_s)\hat{\boldsymbol{z}}$$

where $(\hat{\boldsymbol{x}}, \hat{\boldsymbol{y}}, \hat{\boldsymbol{z}})$ are basis vectors for a local cartesian coordinate system centered at the scattering surface and k is the wavenumber vector magnitude. The Kirchhoff Integral I_K is given in cartesian coordinates by:

$$I_K = \int_{-\infty}^{\infty} \int_{-\infty}^{\infty} \left\{ e^{[(q_s+q_o)^2 \rho(\mathbf{x})]} - 1 \right\} e^{[-i(\boldsymbol{k_s}-\boldsymbol{k_o})\cdot x]} dx dy$$

The vector **x** is the horizontal displacement and the integral is evaluated over all possible displacements on the horizontal plane. $q_s = \widehat{\boldsymbol{z_e}} \cdot \boldsymbol{k_s}$ and $q_o = -\widehat{\boldsymbol{z_e}} \cdot \boldsymbol{k_o}$ are the vertical projections of the scattered and incident wavenumbers, respectively; the kernel functions $B_{\alpha\alpha_o}(\boldsymbol{k_s}, \boldsymbol{k_o})$ are functions of both the scattering geometry and the dielectric constant of sea water. Analytical expression of these functions for the Kirchhoff Approximation (KA) can be found in Voronovich and Zavarotny (2001, RD.15). The dielectric constant for seawater at L-band is obtained from the Klein and Swift model [RD. 13] using fixed sea surface temperature (SST) and salinity (SSS) of 15°C and 35 psu, respectively.

The sea surface elevation function is assumed to be a Gaussian random process, and the correlation function of the ocean surface elevation, ρ(x), is obtained from the Fourier transform of the directional roughness spectrum W(k), which here is given by the wave spectrum model of [RD. 16]. In the present algorithm, only the isotropic part of the spectrum is considered.

3.4.3 Scattered celestial sky radiation contribution

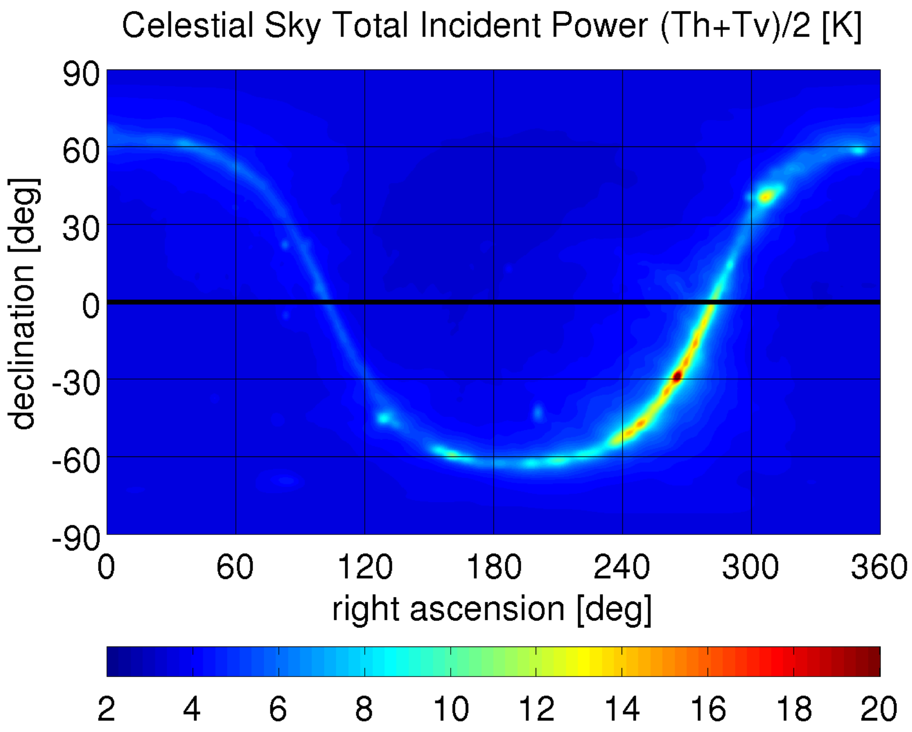

Figure 9. Map of the incident Total power from sky radiation at L-band including CMB, Hi-line (integrated over the SMOS radiometer bandwidth) and continuum contributions.

Radiation from the galactic background (Le Vine and Abraham, 2004) includes Cosmic Microwave Background (CMB) radiation, which is constant in space and time at 2.7 K, plus hydrogen line emission and continuum radiation from extraterrestrial sources. Both are variable across the sky and can affect the measured brightness values by up to 2 – 3 K in general. The total contribution can however be more than 12 K in the direction of the plane of the galaxy even when smoothed by the aperture of large antennas like SMOS (Tenerelli et al., 2008, R.D. 17). Galactic radiation reflects at the sea surface into the satellite radiometer aperture, but can be corrected using data obtained from all sky surveys using L-band radiometers (LeVine and Abraham, 2004; Dinnat and Le Vine, 2008; Tenerelli et al., 2008; Reul et al., 2008a).

In our algorithm we use the same celestial sky radiation map as is used in the SMOS level 2 processor [RD.12]. An electromagnetic scattering model is used to quantify the proportion and direction of reflection at the sea surface into the satellite radiometer aperture. As shown in RD.17,we can uniquely represent the rough sea surface scattered sky radiation as a function of six variables:

$$T_{scp} \rightarrow T_{scp}(\alpha_s, \delta_s, \theta_s, \psi_{uh}, u_{10}, \varphi_w)$$

Where

Variable	Physical Quantity
α_s	Specular right ascension [deg]
δ_s	Specular declination [deg]
θ_s	Scattered incidence angle [deg]
ψ_{uh}	Orientation angle [deg]
u_{10}	10 m height surface wind speed [m/s]
φ_w	Wind direction relative to North [deg]

Table 4 : variables used in the scattering model used for sky radiation

The approach used to model the sea surface scattered sky brightness towards the radiometer integrates the sea surface bistatic scattering coefficients at the radiometer frequency over the incident sky brightness temperatures at 1.4 GHz:

$$T_{scp}(\alpha_s, \delta_s, \theta_s, \psi_{uh}, u_{10}, \varphi_w) = \frac{1}{4\pi\cos\theta_s}\int_{\Omega_o}\left[T_p^{sky}(\Omega_o)\sigma_{pp} + T_q^{sky}(\Omega_o)\sigma_{pq}\right]d\Omega_o$$

where the domain of integration is detrmined uniquely by the set $\{\alpha_s, \delta_s, \theta_s, \psi_{uh}\}$ and T_p^{sky} and T_q^{sky} are the downwelling celestial sky radiation at polarization p and q and $(\sigma_{pp}, \sigma_{pq})$ are the bistatic scattering cross-sections of the rough sea surface. While the sunglint contribution to SMOS measured signal is dominantly induced by scattered radiations far away from the specular direction (see Reul et al., 2017), the scattered sky radiation is dominated by contributions around the specular directions, so that the scattering cross-sections model can be simplified using the Geometrical Optics approximation (which is valid around the specular direction) as follows:

$$\sigma_{pq} = \mathcal{A}\cdot P(S_u, S_c).\left|\bar{\mathcal{K}}_{pq}\right|^2$$

where $\mathcal{A} = \frac{\pi k^2 q^2}{q_z^4}$ and P is the sea surface slope 2D probability distribution function which is taken to be Gaussian in the upwind and crosswind directions:

$$P(S_u, S_c) = \frac{1}{2\pi\sigma_u\sigma_c}exp\left[-\frac{\xi^2+\eta^2}{2}\right]$$

where σ_u^2 and σ_c^2 are the upwind and crosswind mean square slope which are function of the surface wind speed (see further) and the normalized facet slopes are:

$$\eta = S_u/\sigma_u,$$

$$\xi = S_c/\sigma_c,$$

and where the specular facet upwind and crosswind slopes are defined by:

$$S_u = s_{nx}/s_{nz}$$
$$S_c = -s_{ny}/s_{nz}$$

with the cartesian components of the specular facet normal vector which are proportional to:

$$s_{nx} = (\hat{k}_{ox} + \hat{k}_{sx})/2$$

$$s_{ny} = (\hat{k}_{oy} + \hat{k}_{sy})/2$$
$$s_{nz} = (\hat{k}_{oz} + \hat{k}_{sz})/2$$

The unit vectors pointing outward from the origin towards the incident and scattered wave directions are:

$$\hat{\boldsymbol{k}}_o = \hat{k}_{ox}\hat{\boldsymbol{x}} + \hat{k}_{oy}\hat{\boldsymbol{y}} + \hat{k}_{oz}\hat{\boldsymbol{z}}$$
$$\hat{\boldsymbol{k}}_s = \hat{k}_{sx}\hat{\boldsymbol{x}} + \hat{k}_{sy}\hat{\boldsymbol{y}} + \hat{k}_{sz}\hat{\boldsymbol{z}}$$

with:

$$\hat{k}_{ox} = \sin\theta_o \cos\tilde{\phi}_o$$
$$\hat{k}_{oy} = \sin\theta_o \sin\tilde{\phi}_o$$
$$\hat{k}_{oz} = \cos\theta_o$$

and

$$\hat{k}_{sx} = \sin\theta_s \cos\tilde{\phi}_s$$
$$\hat{k}_{sy} = \sin\theta_s \sin\tilde{\phi}_s$$
$$\hat{k}_{sz} = \cos\theta_s$$

where we have defined the downwind-relative azimuth directions as follows:

$$\tilde{\phi}_o = \phi_o - \phi_w$$
$$\tilde{\phi}_s = \phi_s - \phi_w$$

The scattering coefficients σ_{pq} can be estimated with the previous terms and the dimensionless Kirchhoff kernel functions $\overline{\mathcal{K}}_{pq}$:

$$\overline{\mathcal{K}}_{hh} = C \cdot \left[R_v(\widehat{\boldsymbol{h}_s} \cdot \widehat{\boldsymbol{n}_o})(\widehat{\boldsymbol{h}_o} \cdot \widehat{\boldsymbol{n}_s}) + R_h(\widehat{\boldsymbol{v}_s} \cdot \widehat{\boldsymbol{n}_o})(\widehat{\boldsymbol{v}_o} \cdot \widehat{\boldsymbol{n}_s})\right]$$
$$\overline{\mathcal{K}}_{vv} = C \cdot \left[R_v(\widehat{\boldsymbol{v}_s} \cdot \widehat{\boldsymbol{n}_o})(\widehat{\boldsymbol{v}_o} \cdot \widehat{\boldsymbol{n}_s}) + R_h(\widehat{\boldsymbol{h}_s} \cdot \widehat{\boldsymbol{n}_o})(\widehat{\boldsymbol{h}_o} \cdot \widehat{\boldsymbol{n}_s})\right]$$
$$\overline{\mathcal{K}}_{hv} = C \cdot \left[R_v(\widehat{\boldsymbol{h}_s} \cdot \widehat{\boldsymbol{n}_o})(\widehat{\boldsymbol{v}_o} \cdot \widehat{\boldsymbol{n}_s}) + R_h(\widehat{\boldsymbol{v}_s} \cdot \widehat{\boldsymbol{n}_o})(\widehat{\boldsymbol{h}_o} \cdot \widehat{\boldsymbol{n}_s})\right]$$
$$\overline{\mathcal{K}}_{vh} = C \cdot \left[R_v(\widehat{\boldsymbol{v}_s} \cdot \widehat{\boldsymbol{n}_o})(\widehat{\boldsymbol{h}_o} \cdot \widehat{\boldsymbol{n}_s}) + R_h(\widehat{\boldsymbol{h}_s} \cdot \widehat{\boldsymbol{n}_o})(\widehat{\boldsymbol{v}_o} \cdot \widehat{\boldsymbol{n}_s})\right]$$

Here, R_v and R_h are the Fresnel reection coefficients, given as functions of surface salinity S, physical surface temperature T_s and local incidence angle θ_L at the facet:

$$R_{hh}^{(0)}(S,T_s,\theta_L) = \frac{\cos\theta_L - \sqrt{\epsilon_{sw}(S,T_s) - \sin^2\theta_L}}{\cos\theta_L + \sqrt{\epsilon_{sw}(S,T_s) - \sin^2\theta_L}}$$

$$R_{vv}^{(0)}(S,T_s,\theta_L) = \frac{\epsilon_{sw}(S,T_s)\cos\theta_L - \sqrt{\epsilon_{sw}(S,T_s) - \sin^2\theta_L}}{\epsilon_{sw}(S,T_s)\cos\theta_L + \sqrt{\epsilon_{sw}(S,T_s) - \sin^2\theta_L}}$$

where $\theta_L = \mathrm{acos}(\hat{\boldsymbol{k}}_o.\hat{\boldsymbol{k}}_s)/2$.

The unit vectors pointing inward towards the origin from the incident and scattered wave directions are:

$$\hat{\boldsymbol{n}}_o = -\hat{k}_{ox}\hat{\boldsymbol{x}} - \hat{k}_{oy}\hat{\boldsymbol{y}} - \hat{k}_{oz}\hat{\boldsymbol{z}}$$

$$\hat{\boldsymbol{n}}_s = \hat{k}_{sx}\hat{\boldsymbol{x}} + \hat{k}_{sy}\hat{\boldsymbol{y}} + \hat{k}_{sz}\hat{\boldsymbol{z}}$$

and with the polarization basis vectors for the incident and scattered waves in the forward scattering alignment basis convention which are:

$$\begin{aligned}
\hat{\boldsymbol{h}}_o &= \hat{h}_{ox}\hat{\boldsymbol{x}} + \hat{h}_{oy}\hat{\boldsymbol{y}} + \hat{h}_{oz}\hat{\boldsymbol{z}} \\
\hat{\boldsymbol{h}}_s &= \hat{h}_{sx}\hat{\boldsymbol{x}} + \hat{h}_{sy}\hat{\boldsymbol{y}} + \hat{h}_{sz}\hat{\boldsymbol{z}} \\
\hat{\boldsymbol{v}}_o &= \hat{v}_{ox}\hat{\boldsymbol{x}} + \hat{v}_{oy}\hat{\boldsymbol{y}} + \hat{v}_{oz}\hat{\boldsymbol{z}} \\
\hat{\boldsymbol{v}}_s &= \hat{v}_{sx}\hat{\boldsymbol{x}} + \hat{v}_{sy}\hat{\boldsymbol{y}} + \hat{v}_{sz}\hat{\boldsymbol{z}}
\end{aligned}$$

where:

$$\begin{aligned}
\hat{h}_{ox} &= -\sin\overline{\phi_o} \\
\hat{h}_{oy} &= \cos\overline{\phi_o} \\
\hat{h}_{oz} &= 0
\end{aligned}$$

$$\begin{aligned}
\hat{h}_{sx} &= -\sin\overline{\phi_s} \\
\hat{h}_{sy} &= \cos\overline{\phi_s} \\
\hat{h}_{sz} &= 0
\end{aligned}$$

The vertical polarization basis vector components are given by:

$$\begin{aligned}
\hat{v}_{ox} &= -\cos\theta_o \cos\overline{\phi_o} \\
\hat{v}_{oy} &= -\cos\theta_o \sin\overline{\phi_o} \\
\hat{v}_{oz} &= -\sin\theta_o
\end{aligned}$$

$$\begin{aligned}
\hat{v}_{sx} &= -\cos\theta_s \cos\overline{\phi_s} \\
\hat{v}_{sy} &= -\cos\theta_s \sin\overline{\phi_s} \\
\hat{v}_{sz} &= -\sin\theta_s
\end{aligned}$$

With $\overline{\phi_o} = \tilde{\phi}_o + 180°$ and $\overline{\phi_s} = \tilde{\phi}_s$.

This scattering model is using effective sea surface slope variance parameters which are about 50% less than for optical data (Cox and Munk, 1954) and which vary as function of incidence angle and type of pass (ascending versus descending) as illustrated in Fig. 10. These effective upwind and crosswind mean square slope σ_u^2 and σ_c^2 were derived empirically to best match SMOS observed sky radiation scattering at L-band.

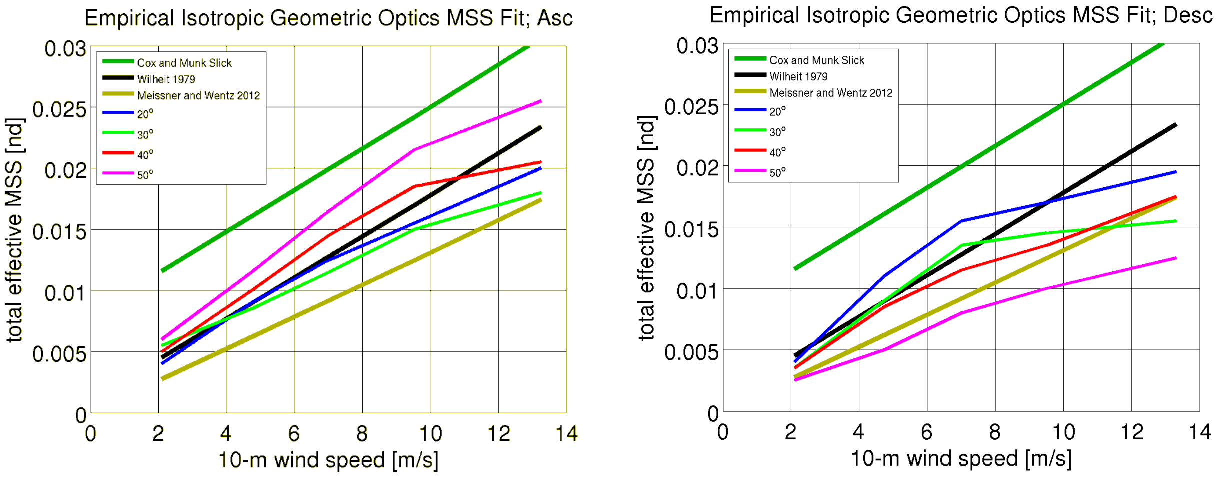

Figure 10. Total mean square slope variance empirical fit : $\sigma_u^2 + \sigma_c^2$ as a function 10-m height surface wind speed as used in our algorithm for ascending (left) and descending (right) passes.

The values (see Fig 10) are consistent with the model used for GNSS-Reflectometry studies at L-band (RD.26) and well match the aircraft flight data acquired by the JPL PALS instrument (RD.27; RD.28), or during the ESA/COSMOS, campaigns (RD.29). SMOS satellite salinity fields however show remaining differences between ascending and descending swaths. These remaining ascending – descending biases have a clear spatial and temporal pattern, which can correlate with the reflection of galactic radiation from the ocean surface, indicating potential residual errors for this contribution. So that for significant sky glint, the wind data will be flagged.

3.4.4 Atmospheric contributions

Following the simpified single layer atmospheric model used in the ESA SMOS Level 2 Ocean Salinity Processor [RD.12], the atmospheric contributions are approximated by the following formulation in which the emission and absorption are expressed purely in terms of air surface temperature T_o, surface pressure P_s, and total column water vapor V.

In terms of these quantities, the vertically integrated absorption owing to modelcular oxygen and water vapor are, respectively:

$$A_d = A_d^{(u)} = A_d^{(d)} = 10^{-6}\left(C_{aao}^{(0)} + C_{aao}^{(1)} T_o + C_{aao}^{(2)} P_s + C_{aao}^{(3)} T_o^2 + C_{aao}^{(4)} P_s^2 + C_{aao}^{(5)} T_o P_s\right)$$

and

$$A_v = A_v^{(u)} = A_v^{(d)} = 10^{-6}\left(C_{aav}^{(0)} + C_{aav}^{(1)} P_s + C_{aav}^{(2)} V\right)$$

Where the numerical values for coefficients in this mono-layer model are from the papers of Liebe (1989, RD.18) and of Liebe et al. (1993, RD.19).

$$C_{aao}^{(0)} = 8033.3$$
$$C_{aao}^{(1)} = -103.999$$
$$C_{aao}^{(2)} = 28.2992$$
$$C_{aao}^{(3)} = 0.2626$$
$$C_{aao}^{(4)} = 0.0064$$
$$C_{aao}^{(5)} = -0.0942$$

and

$$C_{aav}^{(0)} = -151.7150$$
$$C_{aav}^{(1)} = 0.1554$$
$$C_{aav}^{(2)} = 3.5406$$

The corresponding 1-way atmosphereic transmittances associated with molecular oxygen absorption and water vapor along a line of sight at angle θ_s from nadir are:

$$\tau_d = exp[-A_d \sec\theta_s]$$
$$\tau_v = exp[-A_v \sec\theta_s]$$

with this formulation, the surface brightness temperature after passage through the atmosphere T_B' is related to the unattenuated brightness temperature T_B by:

$$T_B' = (\tau_d\tau_v)T_B$$

The upwelling and downwelling atmospheric emission are assumed to be equal and take the following form at nadir for the oxygen and water vapor contributions, respectively:

$$T_{bad} = A_d\left[T_o - C_{aeo}^{(0)} - C_{aeo}^{(1)}T_o - C_{aeo}^{(2)}P_s - C_{aeo}^{(3)}T_o^2 - C_{aeo}^{(4)}P_s^2 - C_{aeo}^{(5)}T_oP_s\right]$$

and

$$T_{bav} = A_v\left[T_o - C_{aev}^{(0)} - C_{aev}^{(1)}P_s - C_{aev}^{(2)}V\right]$$

where:

$$C_{aeo}^{(0)} = -0.7789$$
$$C_{aeo}^{(1)} = 0.1376$$
$$C_{aeo}^{(2)} = -0.0011$$
$$C_{aeo}^{(3)} = -1.1578 \times 10^{-4}$$
$$C_{aeo}^{(4)} = 1.2847 \times 10^{-6}$$
$$C_{aeo}^{(5)} = -1.1133 \times 10^{-5}$$

and

$$C_{aev}^{(0)} = 8.1637$$
$$C_{aev}^{(1)} = 2.4235 \times 10^{-4}$$
$$C_{aev}^{(2)} = 0.0337$$

and the total atmospheric emission brightness temperature at nadir (unpolarized) is:

$$T_{ea} = T_{bad} + T_{bav}$$

Along a path at angle θ_s from nadir, the unpolarized brightness temperature of atmospheric 1-way emission is:

$$T_{ea}(\theta_s) = \sec\theta_s\,[T_{bad} + T_{bav}]$$

3.4.5 Accounting for rotation of the polarization plane in the Stokes vector

In this section, we summarize the Stokes vector transformation that is applied to the forward model from the surface basis to the instrument antenna frame basis, under the conventions used in SMOS, accounting for both a change in polarization basis and the Faraday rotation associated with the passage of radiation through the ionosphere.

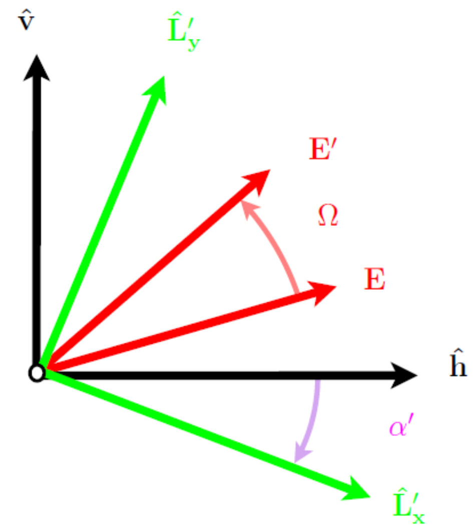

Figure 11. Diagram summarizing the two rotations required to transport a brightness temperature vector from the surface basis $(\hat{\boldsymbol{h}}, \hat{\boldsymbol{v}})$ into the instrument Ludwig-3 basis $(\hat{\boldsymbol{L}}'_x, \hat{\boldsymbol{L}}'_y)$. Here boresight is into the page so we are looking down towards the target from the instrument. Positive Faraday rotation corresponds to the rotation of the electric field vector ***E*** into ***E'*** by the angle Ω as shown. The additional rotation associated with the change of basis is a further counterclockwise rotation of the electric field vector, or clockwise rotation of the basis $(\hat{\boldsymbol{h}}, \hat{\boldsymbol{v}})$ by the angle α'.

3.4.5.1 From surface polarization basis to Ludwig-3 antenna basis

The first rotation, counterclockwise by angle α' looking down towards the target from the instrument, is associated with the change of polarization basis from the surface basis to the instrument basis (so-called Ludwig-3 basis as defined in RD.20), so that:

$$\begin{pmatrix} E_x \\ E_y \end{pmatrix} = \begin{pmatrix} \cos\alpha' & -\sin\alpha' \\ \sin\alpha' & \cos\alpha' \end{pmatrix} \begin{pmatrix} E_h \\ E_v \end{pmatrix}$$

and the corresponding transformation of the Stokes vector is given by:

$$\begin{pmatrix} T_x \\ T_y \\ U_{xy} \\ V_{xy} \end{pmatrix} = \begin{pmatrix} \cos^2\alpha' & \sin^2\alpha' & -\cos\alpha'\sin\alpha' & 0 \\ \sin^2\alpha' & \cos^2\alpha' & \cos\alpha'\sin\alpha' & 0 \\ \sin 2\alpha' & -\sin 2\alpha' & \cos 2\alpha' & 0 \\ 0 & 0 & 0 & 1 \end{pmatrix} \begin{pmatrix} T_h \\ T_v \\ U \\ V \end{pmatrix}$$

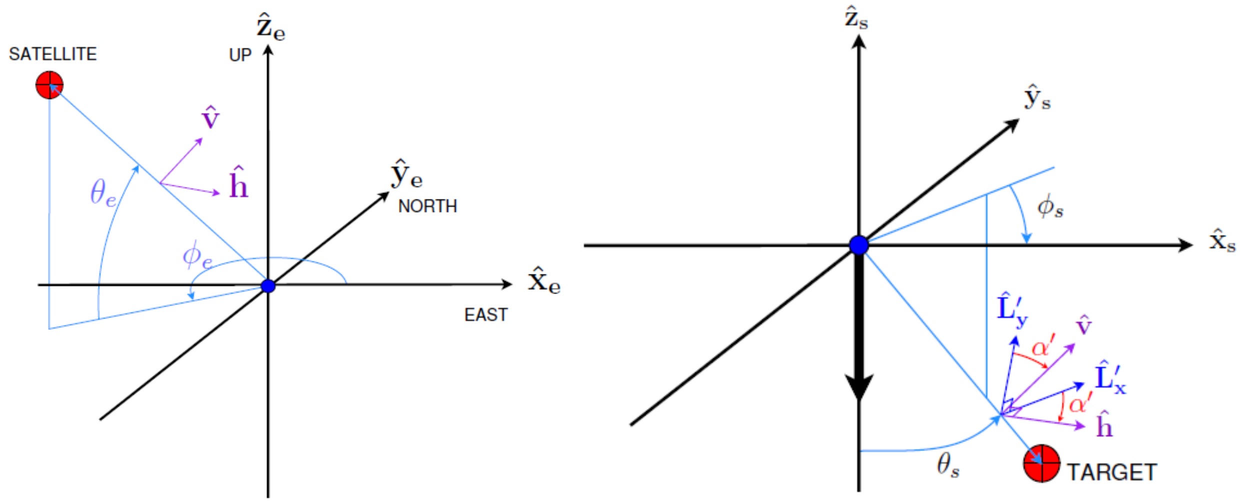

Figure 12 Left : Diagram showing the geometry and polarization basis vectors in the surface target frame, denoted by $(\hat{\mathbf{h}}, \hat{\mathbf{v}})$. The altitude of the emission vector, directed towards the satellite, is θ_e, and the azimuth of this vector, ϕ_e, is measured positive counterclockwise from due east. Right : Diagram showing the geometry in the instrument, or antenna, frame. Ludwig-3 polarization basis vectors are denoted by basis $(\hat{\mathbf{L}}'_x, \hat{\mathbf{L}}'_y)$. The polarisation basis rotation angle α' is the clockwise rotation of the surface $(\hat{\mathbf{h}}, \hat{\mathbf{v}})$ into the instrument Ludwig-3 polarization basis $(\hat{\mathbf{L}}'_x, \hat{\mathbf{L}}'_y)$. Equivalently, this angle is the counterclockwise rotation of the electric field vector looking down towards the target. The angle of the look direction (towards the ground) off of boresight is θ_s, and the azimuth of the look direction ϕ_s, is measured positive clockwise from north.

Fig. 12 shows the surface and instrument (Ludwig-3) polarization basis vectors. The polarization basis rotation angle is found using the method introduced by Duesman and Zundo [AD.5]. In this method, the surface polarization basis vectors have the following cartesian components:

$$\begin{aligned} \hat{\boldsymbol{h}} \cdot \hat{\mathbf{x}}_e &= -\sin\phi_e, \\ \hat{\boldsymbol{h}} \cdot \hat{\mathbf{y}}_e &= \cos\phi_e, \\ \hat{\boldsymbol{h}} \cdot \hat{\mathbf{z}}_e &= 0, \\ \hat{\boldsymbol{v}} \cdot \hat{\mathbf{x}}_e &= -\sin\theta_e\cos\phi_e, \\ \hat{\boldsymbol{v}} \cdot \hat{\mathbf{y}}_e &= -\sin\theta_e\sin\phi_e, \\ \hat{\boldsymbol{v}} \cdot \hat{\mathbf{z}}_e &= \cos\theta_e \end{aligned}$$

For the instrument polarization basis, the following associations are made:

$$\hat{\boldsymbol{x}}_s \rightarrow \hat{\boldsymbol{y}}$$
$$\hat{\boldsymbol{y}}_s \rightarrow \hat{\boldsymbol{x}}$$
$$\hat{\boldsymbol{z}}_s \rightarrow -\hat{\boldsymbol{z}}$$

Now in the conventional formulation for the Ludwig-3 polarization basis vectors, we denote the vector pointing from the antenna to the target by $\hat{\boldsymbol{t}}$ and we simply begin by defining the usual « zonal » and « meridional » unit vectors on the sphere and then rotate them about the target vector $\hat{\boldsymbol{t}}$ by the antenna azimuth ϕ. Thus, we define :

$$\hat{e}_\phi = \frac{\hat{\boldsymbol{z}} \times \hat{\boldsymbol{t}}}{\|\hat{\boldsymbol{z}} \times \hat{\boldsymbol{t}}\|} = \frac{(\hat{\boldsymbol{x}} \times \hat{\boldsymbol{y}}) \times \hat{\boldsymbol{t}}}{\|(\hat{\boldsymbol{x}} \times \hat{\boldsymbol{y}}) \times \hat{\boldsymbol{t}}\|} = \frac{\hat{\boldsymbol{y}}(\hat{\boldsymbol{t}} \cdot \hat{\boldsymbol{x}}) - \hat{\boldsymbol{x}}(\hat{\boldsymbol{t}} \cdot \hat{\boldsymbol{y}})}{\|\hat{\boldsymbol{y}}(\hat{\boldsymbol{t}} \cdot \hat{\boldsymbol{x}}) - \hat{\boldsymbol{x}}(\hat{\boldsymbol{t}} \cdot \hat{\boldsymbol{y}})\|}$$
$$\hat{e}_{\theta =}(\hat{\boldsymbol{z}} \times \hat{\boldsymbol{t}}) \times \hat{\boldsymbol{t}}$$

For convenience, we also define the corresponding unnormalized polarization vectors:

$$e_\phi = \hat{\boldsymbol{y}}(\hat{\boldsymbol{t}} \cdot \hat{\boldsymbol{x}}) - \hat{\boldsymbol{x}}(\hat{\boldsymbol{t}} \cdot \hat{\boldsymbol{y}})$$
$$e_\theta = (\hat{\boldsymbol{z}} \times \hat{\boldsymbol{t}}) \times \hat{\boldsymbol{t}} = (\hat{\boldsymbol{z}} \cdot \hat{\boldsymbol{t}})\hat{\boldsymbol{t}} - \hat{\boldsymbol{z}}$$

which both have the same length, given by $\|\hat{\boldsymbol{y}}(\hat{\boldsymbol{t}} \cdot \hat{\boldsymbol{x}}) - \hat{\boldsymbol{x}}(\hat{\boldsymbol{t}} \cdot \hat{\boldsymbol{y}})\|$. For simplicity, we will use these latter two vectors, rather than the normalized vectors, in what follows. The Ludwig-3 unnormalized components are defined in terms of the preceding unnormliazed vectors by a rotation by the target azimuth in the antenna frame. This rotation is defined so that at boresight, the resulting vectors are now a function of azimuth ϕ:

$$\boldsymbol{L}'_y = e_\theta \cos\phi - e_\phi \sin\phi$$
$$\boldsymbol{L}'_x = e_\theta \sin\phi + e_\phi \cos\phi$$

Now $\cos\phi$ and $\sin\phi$ can be expressed in terms of the target vector and the cartesian basis vector as follows:

$$\cos\phi = -\hat{\boldsymbol{y}} \cdot \left[\frac{\hat{\boldsymbol{t}} \times \hat{\boldsymbol{z}}}{\|\hat{\boldsymbol{t}} \times \hat{\boldsymbol{z}}\|}\right]$$
$$\sin\phi = \hat{\boldsymbol{x}} \cdot \left[\frac{\hat{\boldsymbol{t}} \times \hat{\boldsymbol{z}}}{\|\hat{\boldsymbol{t}} \times \hat{\boldsymbol{z}}\|}\right]$$

The normalized Ludwig-3 basis vectors are:

$$\hat{\boldsymbol{L}}'_x = \boldsymbol{L}'_x / \|\boldsymbol{L}'_x\|$$
$$\hat{\boldsymbol{L}}'_y = \boldsymbol{L}'_y / \|\boldsymbol{L}'_y\|$$

Given a target/satellite position with angles (θ_e, ϕ_e) and (θ_s, ϕ_s), both the surface polarization basis vectors $(\hat{\boldsymbol{h}}, \hat{\boldsymbol{v}})$ and Ludwig-3 basis $(\hat{\boldsymbol{L}}'_x, \hat{\boldsymbol{L}}'_y)$ can be determined with the previous equations. To find the clockwise basis rotation of the surface basis into the Ludwig-3 basis, we note that this corresponds to a counterclockwise rotation of the electric field vector itself, and so :

$$\begin{pmatrix} E_x \\ E_y \end{pmatrix} = \begin{pmatrix} \hat{\boldsymbol{L}}'_x \cdot \hat{\boldsymbol{h}} & \hat{\boldsymbol{L}}'_x \cdot \hat{\boldsymbol{v}} \\ \hat{\boldsymbol{L}}'_y \cdot \hat{\boldsymbol{h}} & \hat{\boldsymbol{L}}'_y \cdot \hat{\boldsymbol{h}} \end{pmatrix} \begin{pmatrix} E_h \\ E_v \end{pmatrix} = \begin{pmatrix} \cos\alpha' & -\sin\alpha' \\ \sin\alpha' & \cos\alpha' \end{pmatrix} \begin{pmatrix} E_h \\ E_v \end{pmatrix}$$

Therefore, we have :

$$\hat{\boldsymbol{L}}'_x \cdot \hat{\boldsymbol{h}} = \cos \alpha'$$
$$\hat{\boldsymbol{L}}'_x \cdot \hat{\boldsymbol{v}} = -\sin \alpha'$$

and so, the polarization rotation angle α' may be computed as :

$$\alpha' = \mathrm{atan2}(-\hat{\boldsymbol{L}}'_x \cdot \hat{\boldsymbol{v}}, \hat{\boldsymbol{L}}'_x \cdot \hat{\boldsymbol{h}})$$

3.4.5.2 Faraday rotation angle

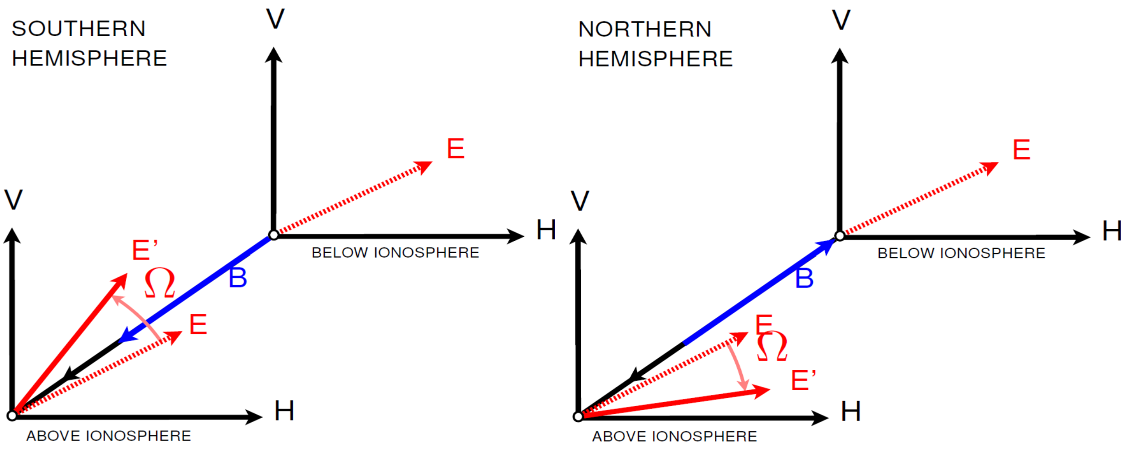

(a) Southern hemisphere, $\Omega > 0$ (b) Northern hemisphere, $\Omega < 0$

Figure 13: Diagram showing how the sense of Faraday rotation depends upon the relative directions of the magnetic field and energy propagation. Also noted is the expected sense of rotation in each hemisphere.

The plane of polarization rotates as radiation passes through the ionosphere with the angle :

$$\Omega = \left(K_f/f^2\right) \cdot VTEC(z = 800\ km, lat_{400}, lon_{400}) \cdot B_0 \cdot \cos \tilde{\theta} \cdot \sec \chi$$

where K_f=1.355x10^4 TECU^{-1}GHz^2 T^{-1}, f is the electromagnetic frequency, VTEC is the vertical total electron content reduced to the satellite altitude using the formulation of Floury [RD.21], B_0 is the magnetic field strength [Tesla] evaluated at the ionospheric pierce point (IPP), the point where the ray from the spacecraft to the surface crosses 400 km (lat_{400}, lon_{400}); χ is the angle the ray makes with the vertical towards the target and θ is the angle between the magnetic field vector and the ray from spacecraft to the surface. As shown in Fig. 16, this angle is generaly larger than 90° in the northern hemisphere (with negative Ω) and less than 90° in the southern hemisphere (with positive Ω).

The reduction of VTEC to satellite altitude is formulated as two equations, one (morning) for local time within 6 hours of 6 a.m., and the other (evening) for local times within 6 hours of 6 p.m.

$$\begin{aligned} VTEC(z = 800\ km, lat_{400}, lon_{400}) \\ &= VTEC(z = \infty, lat_{400}, lon_{400}) \\ &\times \left[(A_m \cdot F_s + B_m) + C_m \cdot \cos\left(D_m \cdot C_m \cdot lat_{400}(\pi/180)\right)\right] \end{aligned}$$

Where F_s is the daily solar flux obtained from daily RSGA files [sfu] and the coefficients A_m, B_m, $C_m$and D_m wehere determined by N. Floury from ESA to be as provided in Table 5.

The $VTEC(z = \infty, lat_{400}, lon_{400})$ is obtained from the 1-day forecast produced Centre for Orbit Determination in Europe (CODE), University of Berne, Switzerland. For reprocessed wind products the VTEC is obtained from IGS consolidated VTEC.

Coefficient	Morning value (between 00 and 12 LT)	Evening value (between 12 and 24 LT)
A_m	-1.43×10^{-4}[sfu^{-1}]	-9.67×10^{-5}[sfu^{-1}]
B_m	8.66×10^{-1}[nd]	8.76×10^{-1}[nd]
C_m	3.75×10^{-3}[nd]	8.98×10^{-3}[nd]
D_m	3.7 [deg^{-1}]	2.03 [deg^{-1}]

Table 5: Coefficients in Floury TEC Altitude Correction

The Magnetic field vector is obtained from the 12th generation of the International Geomagnetic Reference Field (IGRF), evaluated at 400 km above the earth's surface along the line of sight using the software provided in https://www.ngdc.noaa.gov/IAGA/vmod/igrf12.f as converted into a callable FORTRAN function available here:https://gist.github.com/myjr52/62ca6c3e9c78ea0411

The function outputs magnetic field strength in nanoTeslas (1e-9 Teslas) which is converted into Gauss (1e-4 Teslas). This model is valid to the year 2020 and should be updated when a new version of the model becomes available.

Further information on the derivation of the associated geomagnetic model may be found here: https://www.ngdc.noaa.gov/IAGA/vmod/igrf.html

3.5 SMOS L-band wind GMF

Using the forward model expressed in §3.4 forced by auxilliary geophysical data (e.g., obtained from ECMWF atmospheric parameters and SST, CMEMS or the World Ocean Atlas as for the SSS) that are colocalized with SMOS observations, the algorithm evaluate the residual wind/wave/foam induced emissivity as follows :

$$\Delta e_{s1} = \frac{1}{T_s}\left[T_{th}^{(full)} + T_{tv}^{(full)} - (\tau_d\tau_v)[T_{esh} + T_{sch} + T_{ssh} + R_h T_{ea} + T_{esv} + T_{scv} + T_{ssv} + R_v T_{ea}] - 2T_{ea}\right]$$

where $T_{th}^{(full)} + T_{tv}^{(full)}$ are the bias-corrected MIRAS Tbs and where the other contributions are estimated using the forward radiative transfer model (§3.4). The inverse GMF is then applied to the individual scene residual emissivities:

$$\mathrm{w}_r^{(i)}(lat, lon) = GMF^{-1}\left\{\Delta e_{s1}^{(i)}(lat, lon)\right\}$$

After the entire NRT product is processed, the final retrieved wind speed is obtained by averaging the individual scene retrieved wind speeds $\mathrm{w}_r^{(i)}$:

$$w_r(lat, lon) = \langle \mathrm{w}_r^{(i)}(lat, lon) \rangle_{i=1..n}$$

where n is the number of individual winds observed at a given grid node (lat,lon).

The inversion of the estimated wind and wave induced residual contribution to the First Stokes emission into surface wind speed is based on a Geophysical Model Function (GMF) relating Δe_{s1} and the surface wind speed: $\Delta e_{s1} = function\ (w_r)$. The model function used to obtain wind speed from excess emissivity must be valid over the full range of possible wind speeds to be retrieved. Moreover, in order to avoid biases in the retrieved wind speeds, this model function must be consistent with the roughness emission model (Yin et al. (2016), RD.22) used to compute the OTT bias correction for the MIRAS brightness temperatures, which is applied before retrieving the wind speed. As the OTT bias correction is derived using data for which the wind speeds are mostly below 15 m/s, the wind retrieval function should be consistent with that function below 15 m/s. At higher wind speeds, the wind retrieval function must be consistent with the GMF appropriate at high wind speeds, as derived by Reul et al (2012 ; 2016) for Tropical Cyclone conditions (RD.1 see Fig. 14).

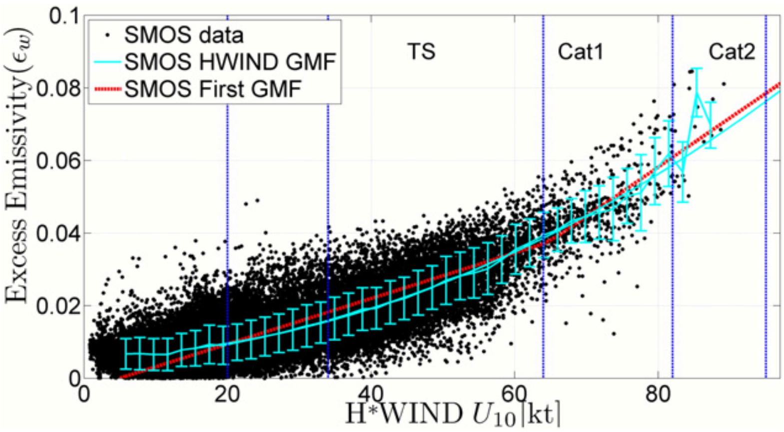

Figure 14: Wind Excess emissivity as function of co-located H*WIND wind speed collected for an ensemble of storms in between 2010 and 2013 as described in Reul et al., 2016. The cyan curve show the 'average' GMF function based on the SMOS/H*WIND paired data sets. The excess emissivity data were averaged per 5 knots bins of H*WIND winds with vertical bar indicating ± 1 standard deviation of the Δe within each wind speed bin.

The GMF of Yin et al. (2016) is detailed in the L2OS ATBD and the reader is refered to [RD.22 and RD.12] for details on this model function. This roughness emissivity model, hereafter denoted $GMF_{L2OS}(w_r)$, is valid for low to moderate wind speeds. It was derived by Yin et al. (2016) by collocating MIRAS brightness temperatures and ECMWF wind speeds and the bulk of the data used to develop this model is characterized by wind speeds below 15 m/s. This roughness emissivity model was derived over the full range of incidence angles observed by MIRAS (in the EAF-FOV) and is a function of wind speed, incidence angle, SSS, and SST.

By contrast, the high wind GMF of Reul et al., (2016) (see RD.1), hereafter denoted $GMF_{HW}(w_r)$ was derived by collocating tropical cyclone wind measurements and dwell-line averaged brightness temperatures from MIRAS. The roughness/foam induced emissivity was derived by averaging all data independent of SSS, SST, and incidence angle and so is a function of wind speed only. It expresses the half-power L-band storm-induced brightness temperature contrast as function of surface wind speed as follows:

$$\frac{\Delta(T_h + T_v)}{2} = T_s \cdot \Delta e_s = T_s \cdot (2.7935 \times 10^{-5} w_r^2 + 6.8599 \times 10^{-5} w_r + 0.0059)$$

or

$$\Delta e_s = GMF_{HW}(w_r) = 2.7935 \times 10^{-5} w_r^2 + 6.8599 \times 10^{-5} w_r + 0.0059$$

Comparison of these two GMFs (Fig. 15) shows that the GMF used in the SSS retrieval algorithm in not accurate for wind speed in excess of about 15 m/s, where it predicts roughness emissivities that are consistently larger than those predicted by the high wind GMF of Reul et al. (2016) (see RD.1). By constrast, the high wind GMF is inaccurate below this wind speed. Moreover, this GMF does not have any dependence upon incidence angle, SSS, or SST.

To derive a wind GMF vaild for the full range of wind speeds, the GMF based on the L2OS roughness emission model of Yin et al. (2016) (see RD.22) for low-moderate wind speeds must be combined with the High-Wind GMF introduced by Reul et al (2016).

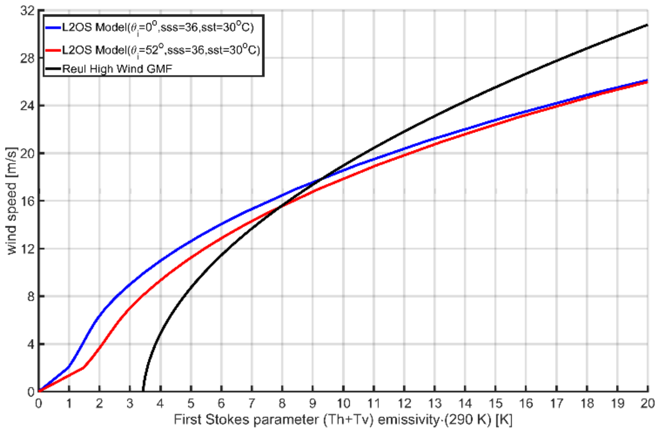

Figure 15: plot showing the function $w_s = GMF^{-1}\{\Delta(T_v + T_h)\}$ where the low-to moderate wind speed GMF of Yin et al., (2016) is shown for two values of the incidence angle: $\theta_i = 0°$ (blue curve) and $\theta_i = 52°$ (red curve), as well as the high wind GMF of Reul et al. (2016) (black curve).

In principle, the wind speeds retrieved using the inverse of the roughness emissivity, namely GMF^{-1} should be consistent with the forward GMF used to compute the complete scene brightness in the forward model. Given the ranges of wind speed within which each of the two GMFS is accurate, an all-wind-speed inverse GMF is introduced to retrieved wind speeds over the full range of roughness emissivities to be encountered. Ideally, the high wind GMF should be extended to include at least incidence angle dependence, but this is a difficult problem because of the scarcity of high winds datasets and the level of noise in the MIRAS brightness temperatures. This task is left for future algorithm evolutions.

Consequently, the approach taken for the current wind retrieval algorithm is to blend the two existing GMFs with weighting functions to ensure smooth transition between the two models.

Let the inverse of the high wind GMF be denoted by:

$$G_H(\tilde{e}) = GMF_{HW}^{-1}(\tilde{e})$$

where $\tilde{e} = \Delta e_s$ is the wind-induced emissivity. Now, let's introduce the low-wind inverse GMF as:

$$G_L(\tilde{e}, \theta, T_s, S) = GMF_{L2OS}^{-1}(\tilde{e}, \theta, T_s, S)$$

where θ is the incidence angle, T_s the sea surface physical temperature and salinity *S*.

The blended all-wind inverse GMF is then defined by:

$$G_A(\tilde{e}, \theta, T_s, S) = w_1(\tilde{e}) \cdot G_H(\tilde{e}) + (1 - w_1(\tilde{e})) \cdot G_L(\tilde{e}, \theta, T_s, S)$$

where $w_1(\tilde{e})$ is a weighting function defined as:

$$w_1(\tilde{e}) = \frac{1}{2}\tanh[5(f(\tilde{e}) - 0.5)]$$

with *f* being a normalizing function given by:

$$f(\tilde{e}) = \begin{cases} 0 \text{ if } \tilde{e} < 0.028 \\ \dfrac{\tilde{e} - 0.028}{0.004} \quad \text{if } 0.028 \leq \tilde{e} \leq 0.032 \\ 1 \text{ if } \tilde{e} > 0.032 \end{cases}$$

The final blended all wind GMF is given by:

$$G_A(\tilde{e}, \theta, T_s, S) = \overline{G_A}(\tilde{e}) + w_2(\tilde{e}) \cdot G_L'(\tilde{e}, \theta, T_s, S)$$

where $\overline{G_A}$ is the preceding blended all-wind inverse GMF function G_A averaged over incidence angle, surface physical temperature and surface salinity:

$$\overline{G_A}(\tilde{e}) = \langle G_A(\tilde{e}, \theta, T_s, S) \rangle_{(\theta, T_s, S)}$$

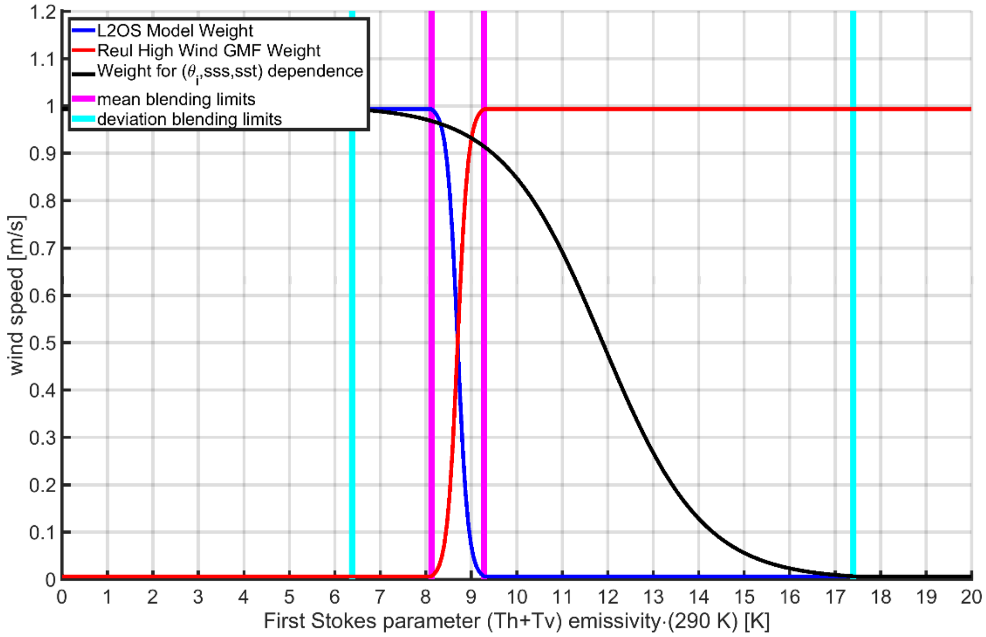

Figure 16: Weighting functions $w_1(\tilde{e})$ (blue), 1-$w_1(\tilde{e})$ (red) and the second weigthing function $w_2(\tilde{e})$ is shown in black.

The function $G_L'(\tilde{e},\theta,T_s,S)$ is the deviation from the low-wind inverse GMF averaged over incidence angle, SST and SSS:

$$\overline{G_L}(\tilde{e}) = \langle GMF_{L2OS}^{-1}(\tilde{e},\theta,T_s,S)\rangle_{(\theta,T_s,S)}$$

defined by:

$$G_L'(\tilde{e},\theta,T_s,S) = G_L(\tilde{e},\theta,T_s,S) + \overline{G_L}(\tilde{e})$$

and $w_2(\tilde{e})$ is another weighting function defined as:

$$w_2(\tilde{e}) = \frac{1}{2}\tanh[5(g(\tilde{e}) - 0.5)]$$

with g being a normalizing function given by:

$$g(\tilde{e}) = \begin{cases} 0 \text{ if } \tilde{e} < 0.022 \\ \dfrac{\tilde{e} - 0.022}{0.038} \text{ if } 0.022 \le \tilde{e} \le 0.06 \\ 1 \text{ if } \tilde{e} > 0.06 \end{cases}$$

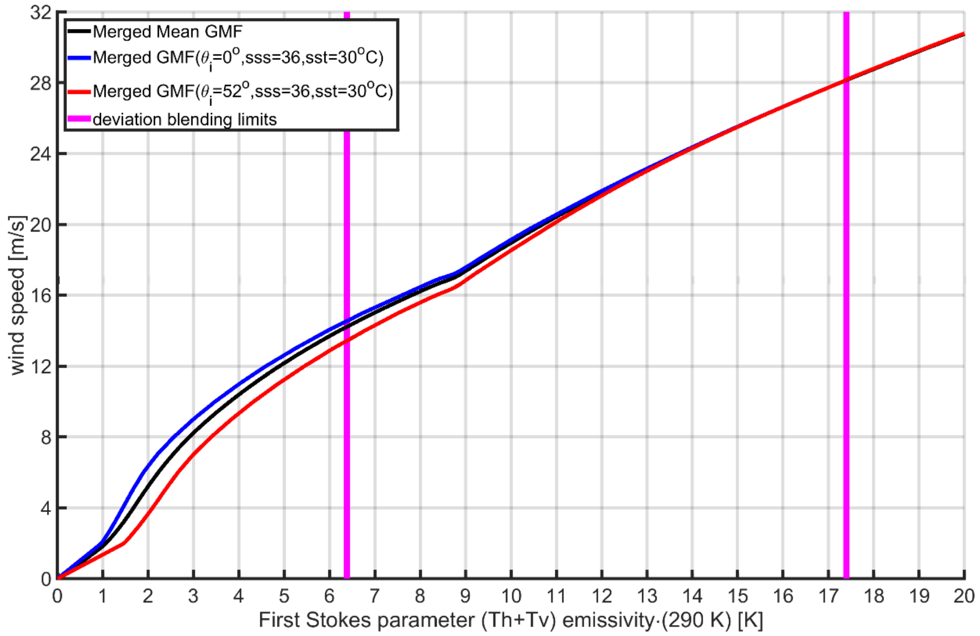

Figure 17: Blended GMF of Yin et al. (2016) GMF and Reul et al. (2016)'s GMF as function of the roughness/foam induced First Stokes parameter [Kelvins].

The resulting blended GMF is shown in Figure 17, for two different incidence angles. SSS and SST dependence is very weak and not shown.

3. 6 Bayesian surface wind speed retrieval method

3.6.1 Retrieval Method

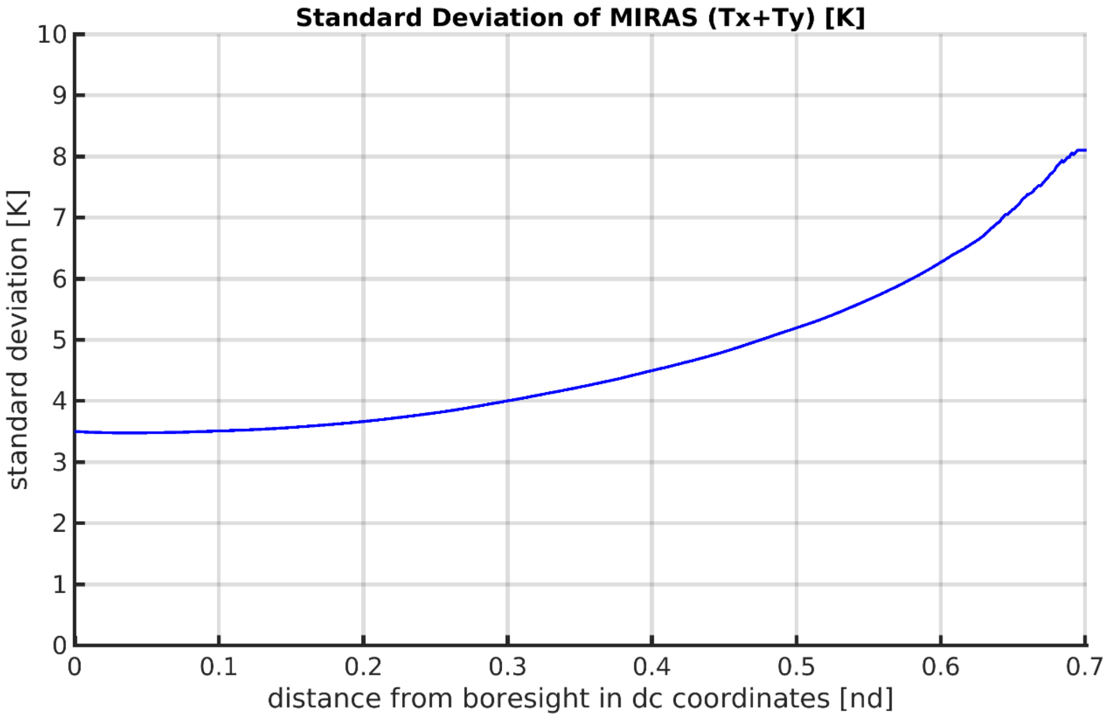

Figure 18 : azimuthally averaged standard deviation of MIRAS First Stokes parameter (K).

The direct inversion method was used for the first version of the products (v100) does not facilitate the introduction of constraints on the retrieved wind speed. The MIRAS measurements are sufficiently noisy that in low roughness conditions the weighted average excess emission can be negative, in which case the direct method yields negative wind speeds. To avoid this issue and to allow the introduction of additional a priori information on surface wind speed, a new wind retrieval method has been introduced. In this Bayesian approach, the posterior distribution of the retrieved wind speed is taken to be the product of the likelihood function $\mathcal{L}$ and a prior distribution P,

$$P\left(\tilde{w}\middle|\boldsymbol{T_p},\boldsymbol{\theta_{i;}}\sigma,w_p\right)=\mathcal{L}(\tilde{w},\boldsymbol{T_p},\boldsymbol{\theta_i})\cdot P(\tilde{w}|\sigma,w_p)$$

where the prior takes the form of a Rice distribution,

$$P\left(\tilde{w}\middle|\sigma,w_p\right)=\frac{\tilde{w}}{\sigma^2}exp\left[-\frac{(\tilde{w}^2+{w_p}^2)}{2\sigma^2}\right]I_o\left(\frac{\tilde{w}\cdot w_p}{\sigma^2}\right)$$

w_p coincides with the distance of the peak of the distribution from the origin and σ is the standard deviation of the individual orthogonal components of the prior wind speed. The standard deviation on the prior wind components takes the form

$$\sigma=\sigma\left(w_p,\tilde{w};\sigma_o,\beta\right)=\sigma_o+\frac{\partial\sigma}{\partial w}\overline{w}=\sigma_o+\beta\overline{w}$$

where the modifed wind speed has been introduced

$$\overline{w} = \alpha w_p + (1-\alpha)\,\widetilde{w}$$

Where α=0.5. This wind speed is a weighted average of the posterior wind speed and the prior wind speed (which, in turn, is set to the ECMWF wind speed). The parameter β is the variation of the prior wind component standard deviation with respect to wind speed and is set equal to the constant value 0.2. The minimum component standard deviation σ_o is set to 0.1 m/s. Examples of this standard deviation and the prior are shown in Fig. 2.

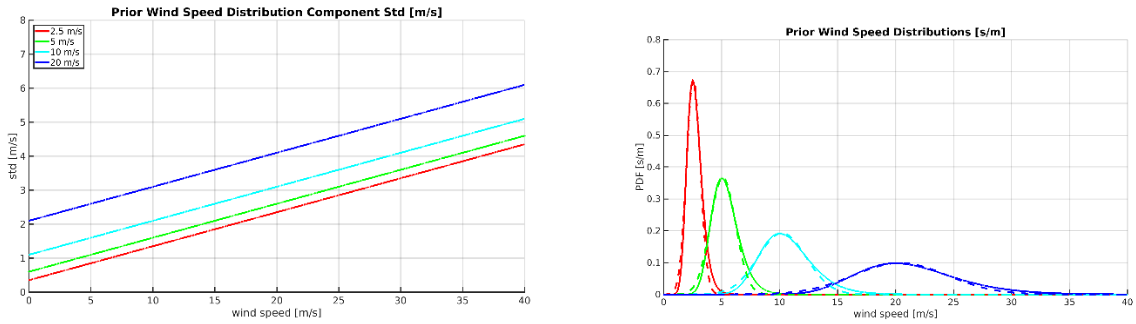

Figure 19 : (Left) The prior wind component standard deviation $\boldsymbol{\sigma(w_p, \widetilde{w}; \sigma_o, \beta)}$ plotted as a function of the retrieved wind speed and evaluated at four values of the prior wind speed; (right) Examples of prior wind speed distribution $P(\widetilde{w}|\sigma, w_p)$ (as a function of retrieved wind speed , $\widetilde{w}$) corresponding to values of w_p of 2.5, 5, 10, and 20 m/s.

The likelihood function is computed using the roughness emission residual brightness temperatures and the geophysical model function (GMF).

$$\mathcal{L}(\widetilde{w}, \boldsymbol{T_p}, \boldsymbol{\theta_i}) = \prod_{i=0}^{N_s} \exp\left[-\frac{\left(\boldsymbol{T_{pi}} - \boldsymbol{G}(\widetilde{w}, T_s, \boldsymbol{\theta_i}, S)\right)}{2\sigma_{pi}^2}\right]$$

Where σ_{pi}^1 is the standard deviation of the first Stokes parameter of the MIRAS reconstructed brightness temperatures (shown in Fig. 18). It is obtained from analysis of a large set of scenes used to build the OTT correction.

The nominal Bayesian wind speed solution is taken to be the mode of the posterior distribution,

$$\widehat{w_r} = arg_{\widetilde{w}} max\ P\left(\widetilde{w}\middle|\boldsymbol{T_p}, \boldsymbol{\theta_i};\sigma, w_p\right)$$

Alternatively, a mean retrieved wind speed may be defined as

$$\widehat{w_2} = \int_0^\infty (\widetilde{w} - \widehat{w_2})^2\ P\left(\widetilde{w}\middle|\boldsymbol{T_p}, \boldsymbol{\theta_i};\sigma, w_p\right) d\widetilde{w}$$

Using this the standard deviation of the retrieved wind speed may be taken to be $\sqrt{\widehat{w_2}}$

3.6.2 Impact of the Bayesian inversion method

The impact of the Bayesian retrieval method is illustrated in this section. The main impact of the Bayesian retrieval is the reduction in the noise near the swath edges, where the new method produces solutions close to that provided by the ECMWF reference wind field.

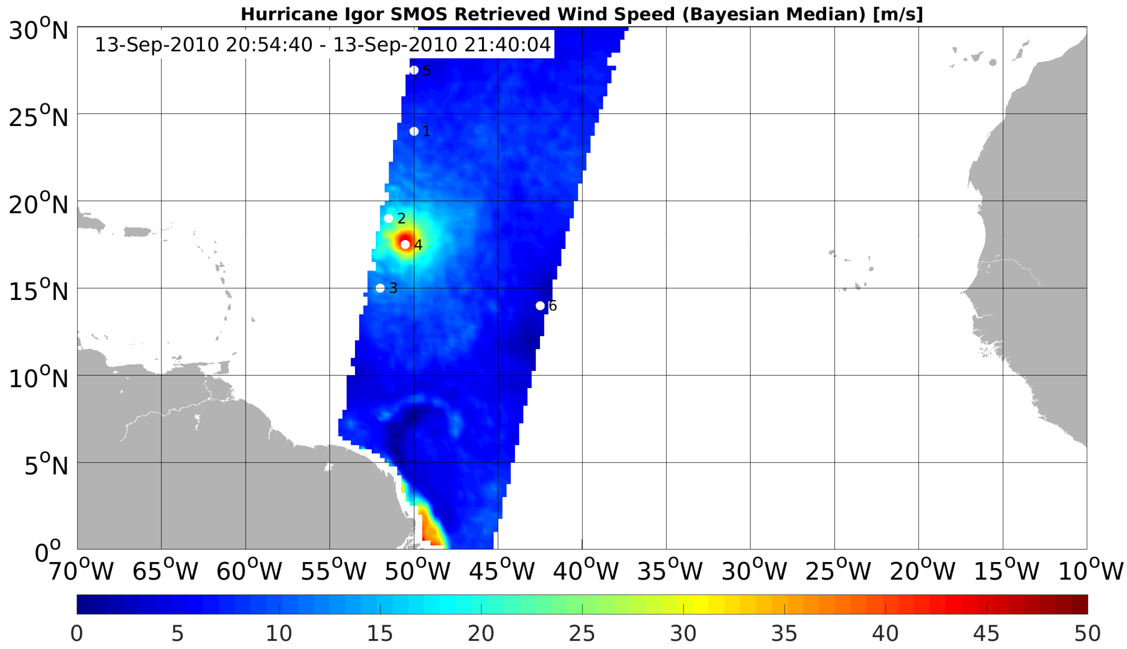

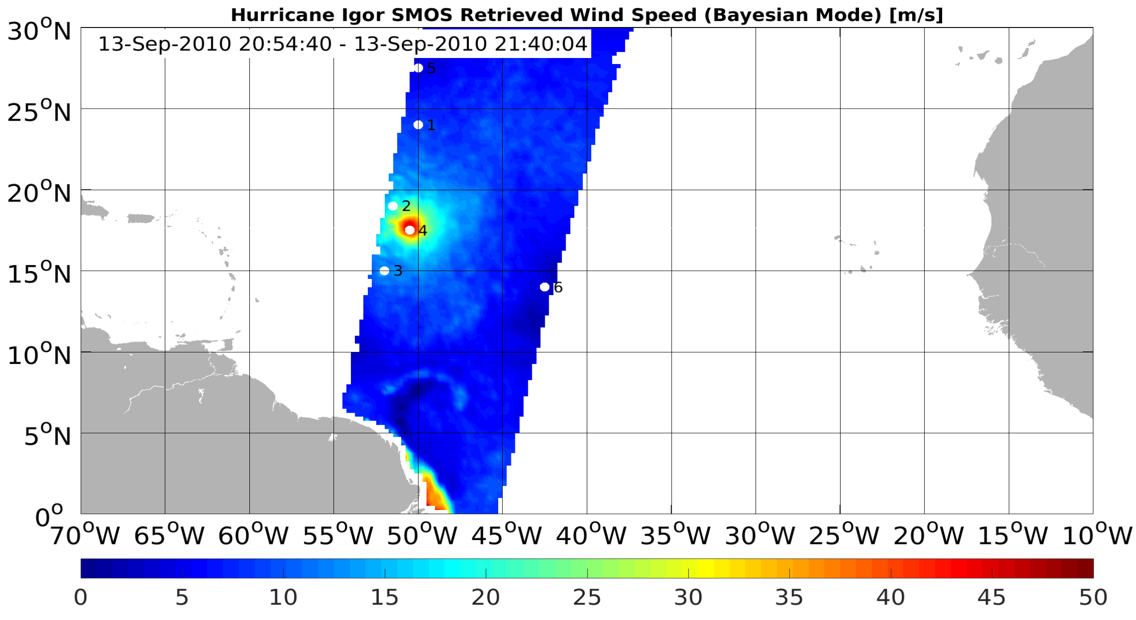

Figure 20 : (Top) Surface wind speed near Hurricane Igor on 13 Sep 2010 retrieved from SMOS (descending pass) using the non-Bayesian algorithm; (bottom): corresponding wind speed retrieved using the Bayesian retrieval method described in 3.6.

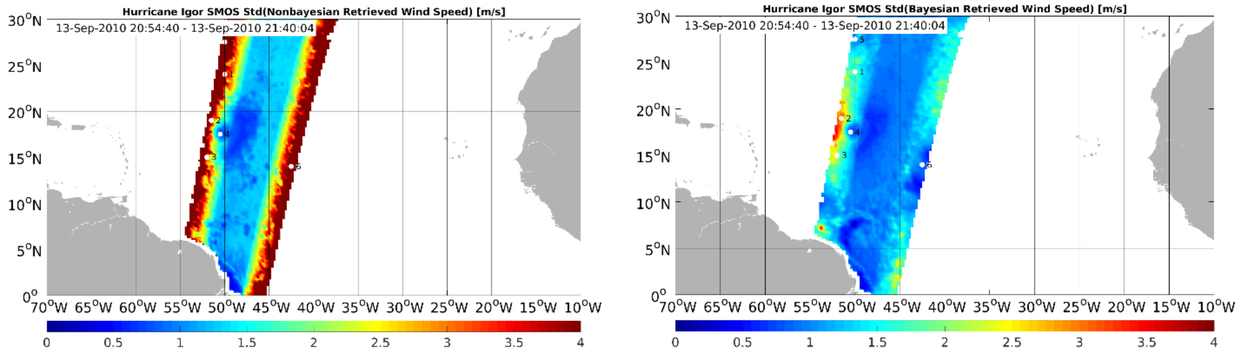

Figure 21 : Estimated standard deviation (m/s) of retrieved wind speed for the retrieved wind shown in Fig. 20; (Left) non-Bayesian method; (Right) Bayesian method.

Fig. 21 shows the corresponding estimated standard deviations. The Bayesian retrieval standard deviations, which are obtained directly from the posterior pdfs, are indeed less than half the corresponding values obtained with the non-Bayesian method near the swath edges. In the region of strongest winds near the storm center both methods yield similar wind speeds and associated errors.

(a) (b)

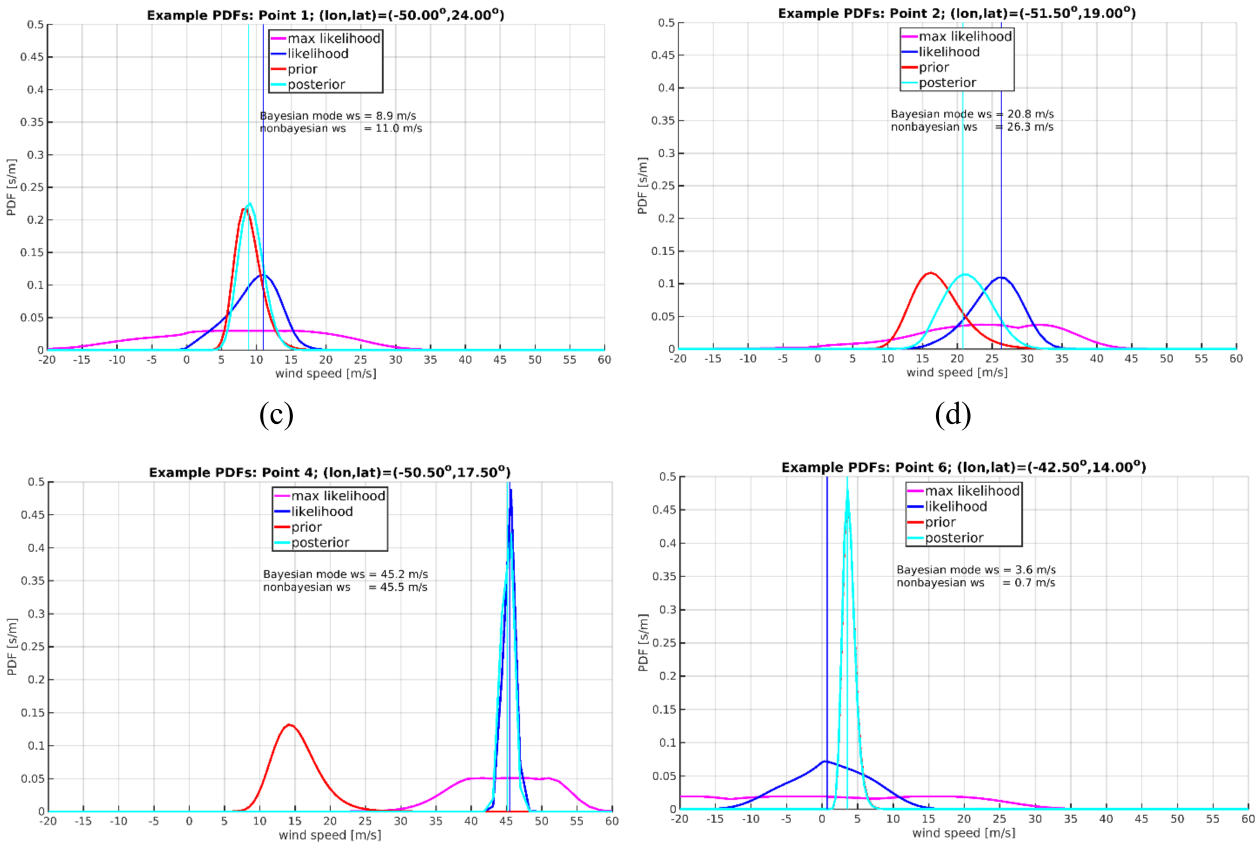

Figure 22 : Posterior (cyan), prior (red) , and likelihood (blue) functions for four points in the vicinity of Hurricane Igor for the swath shown in Figures 20. Also shown (magenta curves) are the envelopes of the likelihood function derived from the individual measurements along the dwell lines. (a)-(d) correspond, respectively, to locations 1, 2, 4 and 6 shown in Figures 20. Abscissa is the wind speed (m/s) and the ordinate is the probability density (s/m).

The influence of the ECMWF-based prior wind speed on the solution is clarified in Fig. 22, which shows the contributions to the posterior pdf at four points distributed around hurricane Igor. Fig. 22(a) (point 1) corresponds to a location at which the ERA-5-based prior peaks near 7 m/s and the likelihood function peaks near 11 m/s. In this case the Bayesian posterior pdf peak location is close to the ERA-5 background value. The wind speed based on the non-Bayesian method is essentially the value at the peak of the likelihood function (11 m/s).

Fig. 22(b) (point 2) depicts a diferent situation, in which likelihood function peak occurs near 26 m/s, the peak in the prior distribution peaks near 16 m/s (the ERA-5 background wind speed), and the posterior pdf peaks in between these two values near 21 m/s. In this case the di_erence between the non-Bayesian and Bayesian methods is quit large (around 6 m/s).

Fig. 22(c) (point 4) depicts an extreme situation near the location of maximum wind near the storm center. In this case the prior and likelihood functions peak at very different wind speeds: the prior peaks near 14 m/s. while the SMOS-based likelihood function peaks near 45 m/s. The sharply-peaked likelihood function dominates the prior and the wind speed obtained using both the non-Bayesian and Bayesian methods are close and around 45 m/s.

Fig. 22(d) (point 5) shows a case where the background wind speed is around 5 m/s while the likelihood function peaks at a slightly negative wind speed (-0.5 m/s). The non-Bayesian method yields an unphysical negative wind speed while the Bayesian solution is very close to the background value. Owing to the formulation of the prior, the Bayesian method can never yield an unphysical negative wind speed.

3.7 SMOS NRT Wind Processor Auxilliary Data Requirements

To calculate the forward radiative transfer solutions to be susbtracted to SMOS data, the NRT wind processor need to be forced by auxilliary data to describe the observed scene as illustrated in Fig. 23.

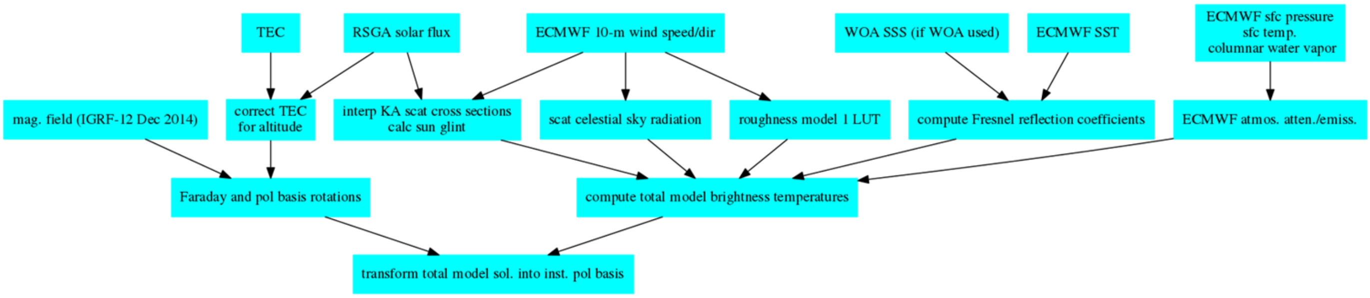

Figure 23: Auxilliary data needed by the NRT wind processor

Auxilliary data are also used to flag the quality of the SMOS retrieved wind speed. The list of auxiliary data used by the processor is listed in Table 6.

Quantity	Required For	Sources
Sea Surface Salinity	Specular Emission	WOA, CMEMS (Mercator), SMOS (CATDS), SMAP (RSS), CCI (ESA)
Sea Surface Temperature	Specular Emission	ECMWF
Surface Pressure	Atmos. model	ECMWF
2-m temperature	Atmos. model	ECMWF
Columnar vapor	Atmos. model	ECMWF
10 m Neutral wind speed	Glint (solar & sky)	ECMWF
land-sea mask	Processor init	ECMWF
Sea Ice Concentration	Processor init	ECMWF
Mispointing angles	Geometry initialization	ESA-ftp MISP files
Best fit plane angles	Geometry initialization	ESA-ftp BFP files
Time correlations	EO-CFI initialization	ESA-ftp BULL_B files
VTEC	Faraday rotation	ESA-ftp COPG or IGSG files
Solar flux	TEC alt. Corretion, sunglint	ESA-ftp RSGA files
ORBSCT file	EO-CFI	ESA-ftp ORBSCT files
Wind GMF	Wind speed inversion	Internal file
OTT bias correction	Stokes vector bias correction	SMOS wind processor

LSC correction	Land sea contamination correction	Internal file
Sea Surface Salinity gridded temporal standard deviation	Flag for high SSS variability zone	In Situ Analysis System (ISAS) [RD.31]
Distance to Nearest Coastlines	Data filtering and Flagging	Internal file

Table 6 : Auxilliary Data Required for the NRT SMOS wind processor

3.8. SMOS Wind Data Quality Level Description

In this section, we describe the ways the SMOS NRT wind processor provide quality estimators associated with the SMOS NRT retrieved wind speed. The quality level estimation approach is twofold:

1. The processor provides an estimate of the retrieved wind speed error based on the standard deviation of the Bayesian retrieved wind speed The error estimate approach is described in §3.6.1

2. Trough an ensemble of tests, conditions for which the surface wind speed retrieval at a given grid node might be degraded are established and associated flags are raised. The combination of flags is used to form final and simple quality level estimates (0=good; 1=fair; 2= poor) which are also provided in the final SMOS NRT wind Level 2 netcdf files. These quality levels are described hereafter.

While the previous statistical retrieved wind speed error estimate provides a first-order estimate of the expected error, it does describe only a limited part of the local conditions in which the measurement was performed. The SMOS NRT wind speed product will not be retrieved properly, or its quality will be degraded to various degrees, for an ensemble of SMOS sensor observational conditions which might include both instrumental and geophysical issues. In this section, we succesively define the conditions and flags in which the SMOS NRT wind quality can be degraded and shall be accepted as 'valid' or not. Note that the final surface wind speed product is gridded onto a regular 0.25° x 0.25° lat/lon grid. To ease the use of the products, we do not provide in the final SMOS Level 2 NRT wind files the ensemble of flags which are tested by the processor to qualify a SMOS surface wind speed retrieval at a given geographical grid node. However, we provide a summary of the data quality through a Quality Level index which equal:

quality_level	**=**	**0**	**(good)**
	=	**1**	**(fair)**
	=	**2**	**(poor)**

We distinguish 6 main types of criteria to determine the ensemble of conditions for which a wind speed value in a given grid cell will belong to either one quality level or not:

1. **missing input data**
2. **Type of observed scene**
3. **Grid cell distance to coast and land contamination extent**
4. **Conditions with high radiometric uncertainties**
5. **Conditions with high geophysical correction uncertainties**
6. **Out of range product fields**

For each main type of acceptance/rejection criteria, there are series of specific tests (with resulting information that can be used internally by the processor but also to provide external the quality level indicators in the final product) that will drive the processor to decide weither or not an SWS retrieval at a given 0.25°x0.25° grid cell shall be accepted or not. These conditions, tests and results are detailed in sections 3.8.1 to 3.8.6. The conditions for which the value of the quality levels are established will be finally be described in § 3.8.7.

3.8.1 Criteria associated to missing input data

If some input data to the SMOS wind processor are missing (e.g., file transfer problems during the ESA/DPGS to Ifremer L1 NRT push, ECMWF missing data, etc..), the retrieved Surface Wind Speed (SWS) quality can be degraded or will not be feasible. Figure 24 provides an overview of these 7 specific cases. Three conditions lead to wind speed retrieval rejection (no input data from DPGS). In the five other conditions, the missing input data are replaced either by other fields (VTEC, Solar Flux, etc..) or by the closest estimates in time from the current NRT file as previously used by the processor.

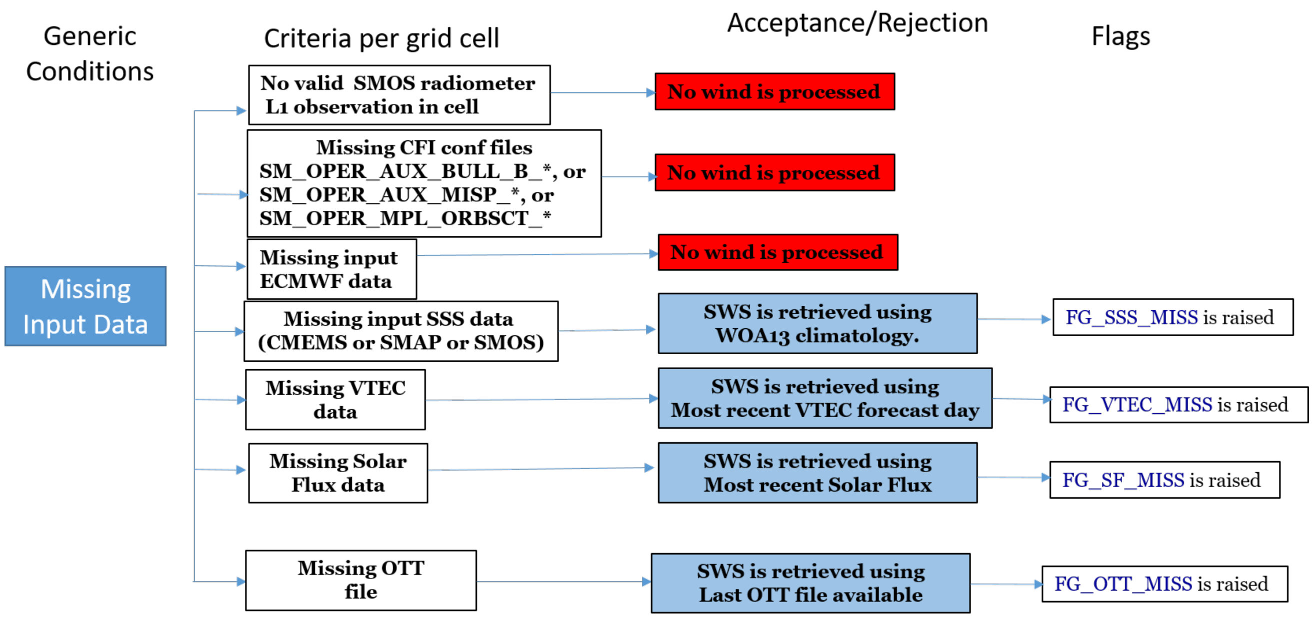

Figure 24 : Sketch showing the SMOS NRT wind processor acceptance criteria in conditions of missing input data. The critera leading to surface wind speed product acceptance and rejection are shown in blue and red colors, respectively. The Flags are internal to the processor and not available within the SMOS Level 2 wind speed product.

Note that in the following cases :

- there are **no valid SMOS radiometer L1 observation in the grid cell** such a situation can happen when the satellite performs cold-sky calibration manoeuvers and is detected by the processor when the antenna boresight incidence angle is exceeding 42°±3°
- one of the **Earth CFI configuration files are missing :**
  - ✓ SM_OPER_AUX_BULL_B_* (UTC, UT1 correaltion time information), or,
  - ✓ SM_OPER_AUX_MISP_* (antenna mispointing errors), or,

- ✓ SM_OPER_MPL_ORBSCT_* (satellite orbit parameters)
- the **input ECMWF data are missing**

the NRT SMOS level 2 wind speed product will not be generated. In case other input data are missing, alternative data can be used as input to the processor but then internal quality flags are raised as described herebelow:

- **Missing input SSS data**

⇨ If the auxilliary SSS data used as input by the processor (from either CMEMS daily forecasts, SMOS or SMAP L3 SSS map from the preceeding week, depending on the processor configuration choice) are missing, surface wind speed is retrieved using WOA13 climatology by default. The internal flag FG_SSS_MISS is raised and the interpolated WOA13 climatology is used instead for correcting the Tb with the differents forward model components.

- **Missing VTEC data**

⇨ surface wind speed is retrieved. The last VTEC file available is used to cover a possible gap of few days during NRT operation. The internal flag FG_VTEC_MISS is nonetheless raised if one or more VTEC data is missing for the ionospheric correction models.

- **Missing Solar Flux data**

⇨ surface wind speed is retrieved. The last Solar Flux data available is used to cover a possible gap of few days during NRT operation. The internal flag FG_SF_MISS is raised if one or more solar flux data is missing for the sunglint forward models.

- **Missing OTT file**

⇨ surface wind speed is retrieved. The last OTT file generated by the processor and available is used to cover a possible gap of few days during NRT operation. The internal flag FG_OTT_MISS is raised if the last OTT file is missing.

For an ensemble of instrumental and observational conditions, the surface wind speed can not be evaluated (e.g ; 100% land fraction in the pixel) or it will be of degraded quality (e.g. solar effects, land contamination, RFI, uncertainties in forward model, etc...). To determine such conditions, the processor will evalute criteria and will raised internal flags characterizing:

- the type of scene observed within the surface wind speed retrieval cell,
- the surface wind speed retrieval cell distance to coasts and the level of Land Sea Contamination,
- the conditions with large radiometric uncertainties (solar & galactic glints, RFI, etc..),
- the conditions with large geophysical and forward model uncertainties.

We review them successively hereafter.

3.8.2 Characterizing the type of observed scenes.

As described in Figure 25, the processor will reject or accept a wind speed retrieval in a grid cell depending on the type of scene observed within that cell. The types of scenes are defined by 7 criteria, leading to four surface wind speed rejections and 3 acceptances. To characterize the land/ocean/ice fraction, we use the static land mask and water fraction from ECMWF, and, the dynamic Sea Ice Concentration from ECMWF (see table 6).

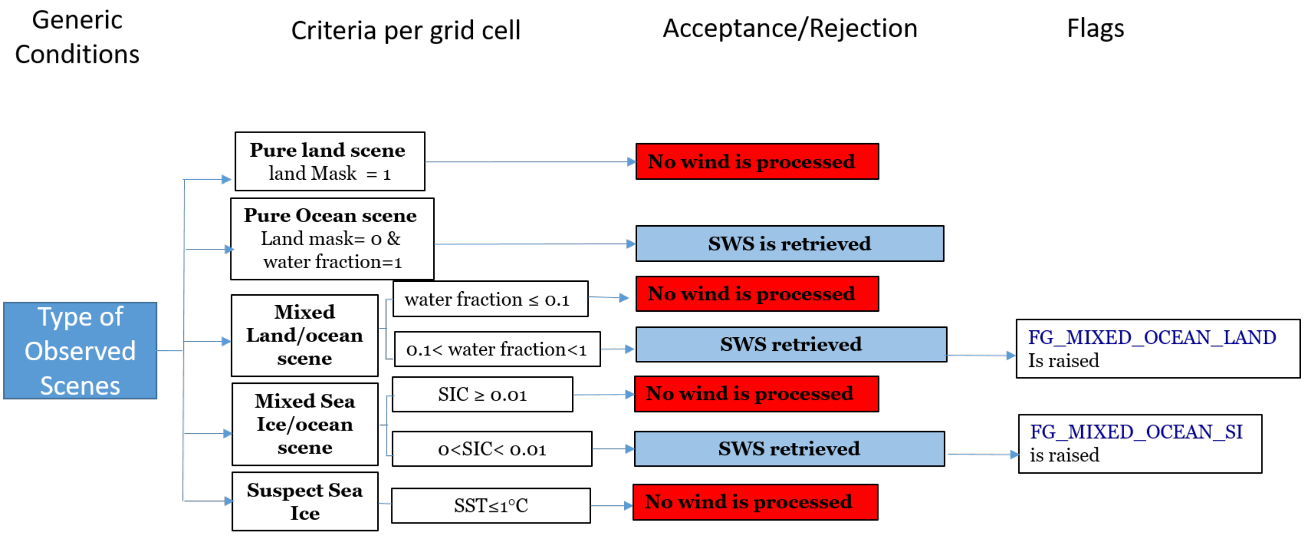

Figure 25 : Sketch showing the SMOS NRT wind processor acceptance criteria as a function of the type of observed scenes. The critera leading to surface wind speed product acceptance and rejection are shown in blue and red colors, respectively. The Flags are internal to the processor and not available within the SMOS Level 2 wind speed product.

If the centroid of the grid cell [lon,lat] at which the surface wind speed is retrieved belong to either:

- a **pure land scene** (land mask equal 1).

⇨ then surface wind speed is not retrieved.

- a **pure ocean scene** (water fraction in grid cell equal 1 & land mask equal 0)

⇨ then surface wind speed is retrieved.

- **a mixed land/ocean scene** (land mask equal 0, land and ocean fractions in grid cell less than 1) :
  If water fraction ≤ CTRL_WATER_FRAC (default=0.1) then there is a high probability of pixel contamination by land masses.

⇨ surface wind speed is not retrieved

If CTRL_WATER_FRAC < water fraction<1

⇨ surface wind speed is retrieved. Moderate to strong degradation is expected and the internal flag FG_MIXED_OCEAN_LAND will be raised.

- **A mixed sea-ice/ocean scene** (sea ice and ocean fractions in grid cell less than 1)
  if Sea Ice Concentration (SIC) ≥ CTRL_SIC (default=0.01)

⇨ surface wind speed value is not retrieved.

If Sea Ice Concentration (SIC) is 0 < SIC < CTRL_SIC
⇨ surface wind speed is retrieved. Moderate to strong degradation is expected and the internal flag FG_MIXED_OCEAN_SI will be raised.

- **A scene with suspect sea ice**

Salty water freezes below 0°C with a freezing temperature that decreases linearly with increasing salinity from 0°C at SSS=0 to −1.8°C at SSS=35. So for most ocean SSS values, a sea surface temperature below 0°C might indicate the presence of sea ice. In practice we noticed that ice contaminated pixels still remain after applying this filter, so we choose a more conservative threshold filtering value for low SST of 1°C

If SST ≤ CRTL_LOW_SST (default=1°C):
⇨ SWS value is not retrieved.

3.8.3 Distance to coasts criteria and land contamination correction uncertainties

For SMOS data, significant errors exist near coastal areas because of the contamination by the nearby land signals radiating in the synthetic beam main and secondary lobes. As shown in Li et al. (2017), within 40 km of Distance to Coast (DC), the brightness temperature error is large and decreases sharply from ~60 K to ~4 K with the increase of DC, since the mainlobe of the antenna array is departing from land to ocean; during 40-120 km of DC, gibbs-like phenomena due to secondary antenna lobes can still contamine the data and shall be flagged. We use a static map of the distance to nearest coastlines evaluated at the SWS grid nodes.

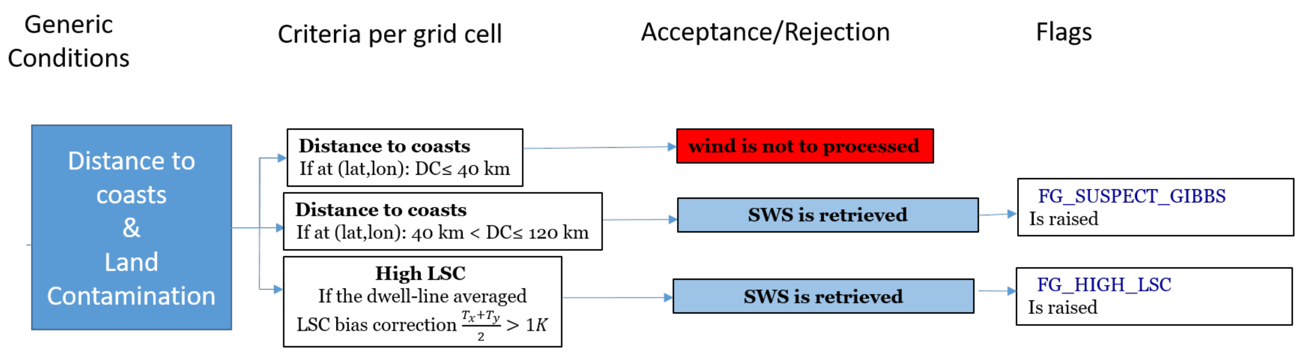

Figure 26: Sketch showing the SMOS NRT wind processor acceptance criteria as a function of the grid node (lon,lat) distance to coasts and Land Sea Contamination LUT correction amplitude. The critera leading to SWS product acceptance and rejection are shown in blue and red colors, respectively. The Flags are internal to the processor and not available within the SMOS Level 2 wind speed product.

For a given grid node (lon,lat) where surface wind speed is retrieved, we therefore evaluate the **distance to nearest coasts**: DC. Then :

- If DC ≤ CTRL_DIST2_COAST1 (default is 40 km):

⇨ surface wind speed is not retrieved

- If CTRL_DIST2_COAST1 < DC ≤ CTRL_DIST2_COAST2 (default is 250 km):

⇨ surface wind speed is retrieved. Moderate to strong degradation is expected and the internal flag FG_SUSPECT_GIBBS will be raised.

In addition, residual errors persist in the SMOS interferometric image reconstruction over ocean pixels in presence of land masses located somewhere in the extended Field Of View (FOV) of the MIRAS antenna. These residual errors are called "**Land Sea Contamination**" (LSC) and consists fundamentally of a perturbation of the brightness temperature of water in zones near large land areas. This contamination extends to distances much larger (up to ~800 kms) than the relatively low resolution of the instrument would predict. It was reported early in the mission by the SMOS ocean science team to be associated generally with both positive and negative biases, and it has been so far the most important limitation in using SMOS data for coastal areas. It is important for wind speed retrieval since the first Stokes parameter varies by only about 0.3-0.7 K/m.s^{-1}. Part of the LSC can be attributed to the so-called 'floor' error and can be slightly reduced by using differential techniques before visibility inversion. However, no image reconstruction method has yet been able to fully cancel this artifact. An empirical correction method was therefore derived for sea surface salinity retrievals. A Look-Up Table (LUT) correction has been derived by comparing time-average differences between radiative transfer forward model predictions and L1 reconstruted images as function of:

- latitude, longitude of the earth target
- xi, eta coordinates of the Tbs in the antenna frame
- ascending or descending orbit pass direction D
- Tb polarization in the antenna-frame (X or Y)
- Polarization of the snapshot *p*

The ensemble of multi-angular brightness temperatures $Tb_{i=1\ldots n} = Tb(\theta_{i=1\ldots n})$ used to estimate the surfac ewind speed for a given grid node (lon,lat) is obtained for an ensemble of pairs $(xi_j, eta_j)_{j=1\ldots n}$ coordinates and polarizations at the grid node (lon,lat). The dwell line-averaged absolute amplitude of the LSC LUT value which was applied for each individual Tb_i provides an estimate of the 'strength' of the LSC correction which was applied in a given grid cell :

$$\mathrm{mod}^{LSC} = |< mod_i^{LSC} >_{i=1\ldots n}|$$

where mod_i^{LSC} denote the amplitude of the LSC LUT applied to each individual brightness temperature in a given dwell-line.

Let CTRL_LUT_LSC_MOD =1K (configurable value) be the threshold amplitude of the empirical LSC correction above which the LSC LUT correction is judged significant.

- **Land Sea Contamination criteria:**

If $\mathrm{mod}^{LSC} \geq$ CTRL_LUT_LSC_MOD,

⇨ Then surface wind speed is retrieved. Moderate to strong degradation is expected and the internal flag FG_HIGH_LSC will be raised.

3.8.3 Criteria to characterize conditions with high Radiometric uncertainties

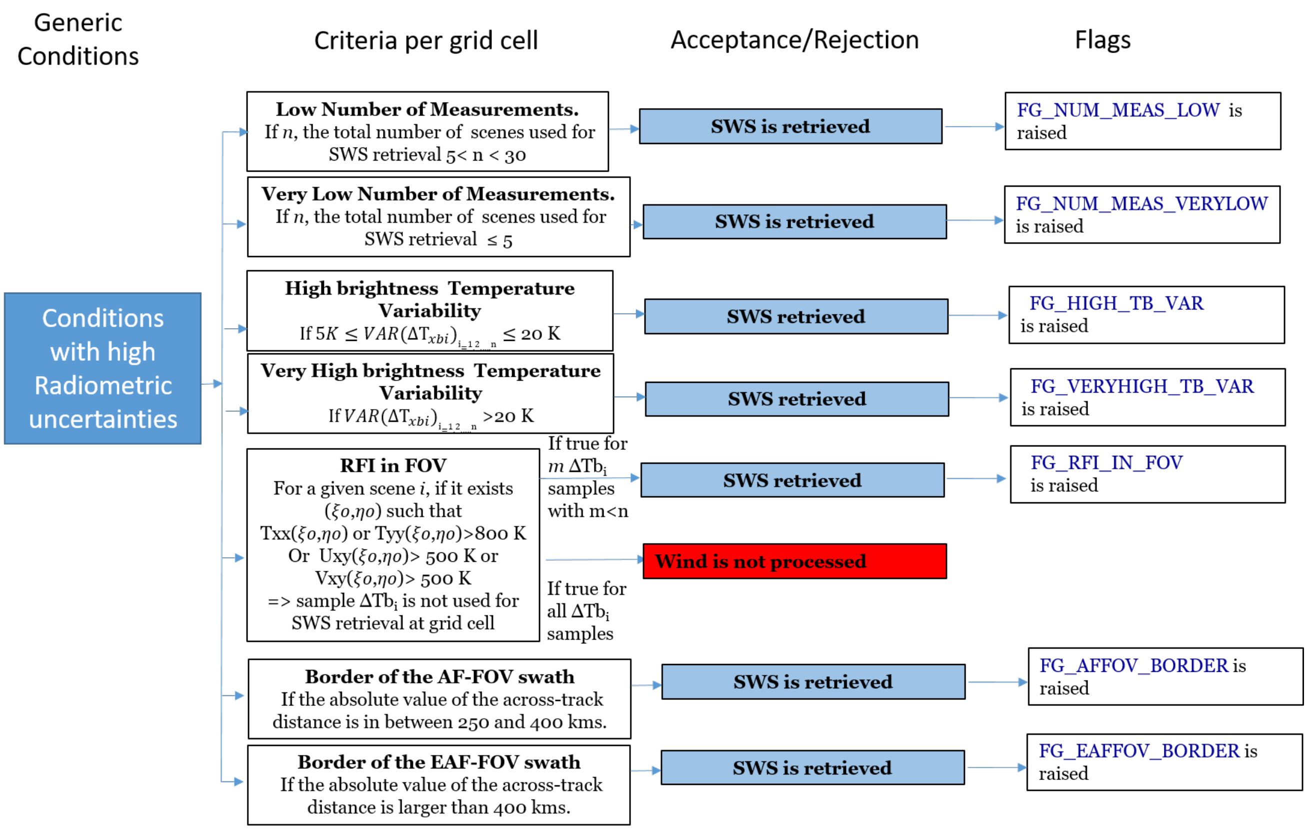

Figure 27: Sketch showing the SMOS NRT wind processor acceptance criteria in increased radiometric uncertainty conditions. The critera leading to SWS product acceptance and rejection are shown in blue and red colors, respectively. The Flags are internal to the processor and not available within the SMOS Level 2 wind speed product.

Uncertainties in the SMOS retrieved wind speed do include radiometric uncertainties which can be significant in the input L1 data and processings for an ensemble of conditions such as (see Fig. 27):

- **Low number of measurements**:

Let $\Delta Tb_{i=1...n}$ be the *n*-multi-angular wind-induced brightness temperature residuals which are used to retrieved the SMOS NRT SWS in a grid cell. If CTRL_NUM_MEAS_VERYLOW (default =5)< n < CTRL_NUM_MEAS_LOW (default =30), then the surface wind speed is retrieved from a low number of measurements and the internal flag FG_NUM_MEAS_LOW will be raised.

- **Very Low number of measurements:**

Let $\Delta Tb_{i=1...n}$ be the *n*-multi-angular wind-induced brightness temperature residuals which are used to retrieved the surface wind speed in a grid cell. If n ≤ CTRL_NUM_MEAS_VERYLOW (default =5), then the surface wind speed is retrieved from a very low number of measurements and the internal flag FG_NUM_MEAS_VERYLOW will be raised.

- **High and very high variability in the multi-angular brightness temperature residuals:**

In Reul et al. 2012 [RD.5], it was shown that except for wind speeds smaller than about 20 m.s^{-1}, there is apparently a small dependence of the wind-excess emissivity at high winds on incidence angle. Regardless of incidence angle, 50 km resolution ΔT_b data increase quadratically with the surface wind speed. For almost all individual wind speed bins, the differences between averaged ΔT_{bi} acquired at incidence angles ranging from ~10° to ~60° are always smaller than ~5 K, which is below the SMOS instrumental noise level. Only the data at low incidence angles (15° and 25°) and for wind speed smaller than 20 m.s-1 exhibit slightly smaller ΔT_{bi} values than at the other angles.

- If the variance Var($\Delta T_b^{i=1..n}$) of the n-multi-angular wind-induced brightness temperature residuals ΔTbi=1…n which are used as inputs to retrieve the surface wind speed in a grid cell is such that:

CTRL_VAR_MEAS_TB_HIGH(default=5K)≤Var($\Delta T_b^{i=1..n}$)<CTRL_VAR_MEAS_TB_VERYHIGH (default=20K) it is likely that there is either an RFI contamination or other sources of radiometric uncertainty. The internal flag FG_HIGH_TB_VAR is raised.

- If the variance Var($\Delta T_b^{i=1..n}$) of the n-multi-angular wind-induced brightness temperature residuals ΔTbi=1…n which are used as inputs to retrieve the surface wind speed in a grid cell is such that: Var($\Delta T_b^{i=1..n}$)>CTRL_VAR_MEAS_TB_VERYHIGH (default=20K)

The brightness variance is very high and the surface wind speed quality is very likely affected by an RFI contamination or other sources of radiometric uncertainty. The internal flag FG_VERYHIGH_TB_VAR is raised.

- **Radio Frequency Interferences:**

Radio Frequency Interferences continues to plague SMOS SSS and SM geophysical product retrievals and certainly affect also the quality of wind speed retrieval from SMOS data in many important areas. Fig. 28 is one example showing intermittent contamination from radars in Alaska. The RFI induces large spatial ripples in the images far from the sources, and the impact extends into the extended field of view (magenta domain) where surface wind speed is retrieved.

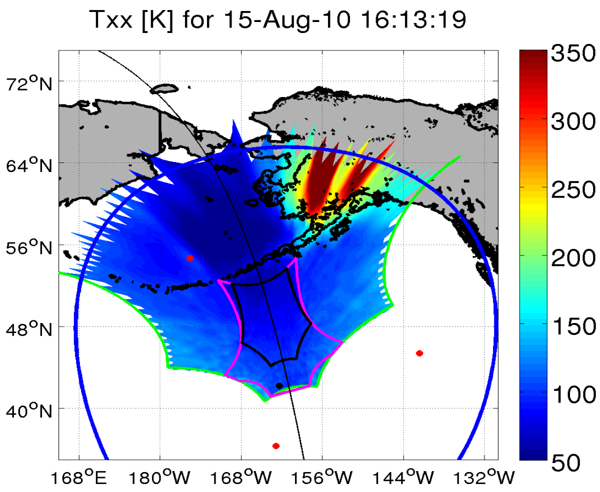

Figure 28. Example of a strong RFI detected far away from the retrieval zone (magenta domain).

No solution proposed thus far can eliminate its impact in all cases. Many people have been working on this problem and at this time there is not a satisfactory correction methodology. Most of the effort is directed towards filtering out contaminated brightness temperatures. However, much (but not all) of the RFI impact over the ocean is related to sources over land, and the impact in the usable portion of the field of view can be difficult to detect by simple thresholds on brightness temperatures in the usable portion of the FOV.

One approach is to search for RFI in the entire fundamental hexagon using simple (empirically determined) thresholds on the brightness temperatures (800 K for Txx and Tyy, and 500 K for the third and four Stokes parameter Uxy and Vxy). For a given scene i, we first sort the brightness temperature stokes vector elements Txx, Tyy, Uxy and Vxy polarizations including the earth-surface reconstructed Tb values outside the fundamuntal hexagon of the SMOS reconstructed FOV. Then we look for brightness temperatures in excess of configurable threshold values, so that for a given snapshot i,

-if it exist $(\xi o,\eta o)$ such that Txx$(\xi o,\eta o)$>CTRL_RFI_TXX, Tyy$(\xi o,\eta o)$> CTRL_RFI_TYY, Uxy$(\xi o,\eta o)$> CTRL_RFI_UXY or Vxy$(\xi o,\eta o)$> CTRL_RFI_VXY, then the scene i won't be used for the final surface wind speed retrieval at a given grid cell.

By default, we will use the same threshold values as in the SMOS+STORM prototype processor:

- CTRL_RFI_TXX= CTRL_RFI_TYY=800K
- CTRL_RFI_UXY=500 K
- CTRL_RFI_VXY=500 K

If the RFI test is true for *m* samples of the *n*-multi-angular ΔTb_i samples available at a grid node such that m<n/2 then SWS is retrieved but the internal flag FG_RFI_IN_FOV is raised.

-if any of the fourth preceeding flags is raised for more than 50% of the *n* multi-angular brightness temperatures $Tb_{i=1...n}$ = Tb $(\theta_{i=1...n})$ samples (i.e. if $m \geq n/2$) used to retrieve surface wind speed at a grid node than we consider that too much scenes are contamined by RFI to produce a reliable wind speed and the final value is not processed.

- **Sun and sun alias imaging:**

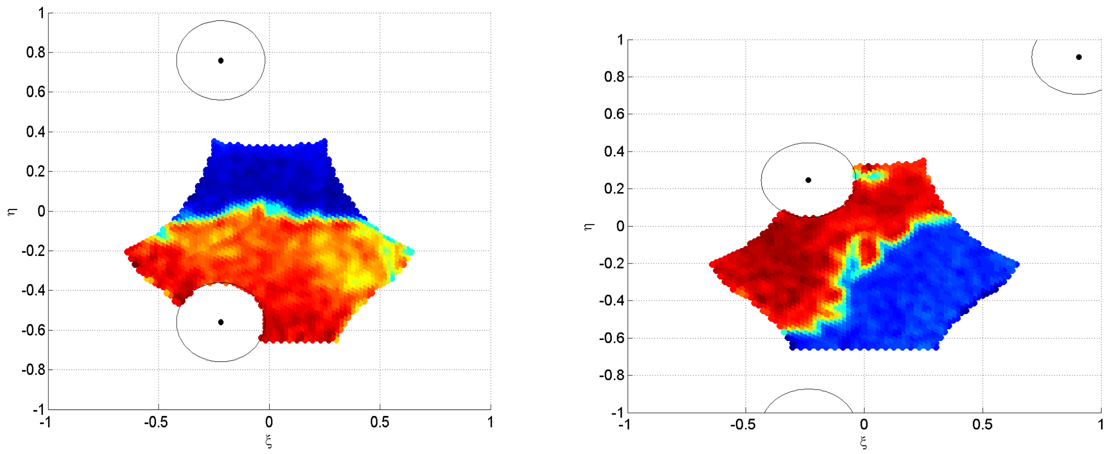

Figure 29: Illustration of the data filtering around sun alias images. The black dots are showing the position of the sun aliases and the circles around them delineate the circular area where we removed data in proximity to the aliases (for this example the sun blanking radius is 0.2).

The direct sun image and its aliases are a strong source of data contamination in the SMOS Field of view that might translate into inaccurate wind speed retrievals. Several methodologies to remove that spurious signal during the Level 1A to Level 1B processing have been developed and proposed but none of them give a perfect correction. Residual errors are still present after the Level 1A to Level 1B processing and sun tails signals are found in the Level 1B data. To minimize that effect we filter the data around the location of each of the 6 sun aliases, within a radius of CTRL_SUN_RAD = 0.05 in the cosine director coordinate system as illustrated in Fig. 26. This can generate local gaps in the dwell-line data.

- **Border of the Alias-Free Field of View:**

If the absolute value of the across-track distance is in between CTRL_AFOV_BORDER= 250 km and CTRL_EAFOV_BORDER= 400 kms, the SWS is retrieved on the border of the Alias-Free Field of View. The quality is degraded because less multi-angular data are available than in the central part of the swath.

- **Border of the Extended Alias-Free Field of View:**

If the absolute value of the across-track distance is larger than CTRL_EAFOV_BORDER=400 kms, the SWS is retrieved on the border of the Extended Alias-Free Field of View. The quality is highly degraded because little multi-angular data are available for retrieval and the radiometric uncertainty is highest.

3.8.4 Criteria for high geophysical correction uncertainty conditions

Finally, some geophysical contributions to the observed brightness signal at L-band in general conditions are poorly known and/or erroneously accounted for in corrections implemented in the retrieval algorithms.

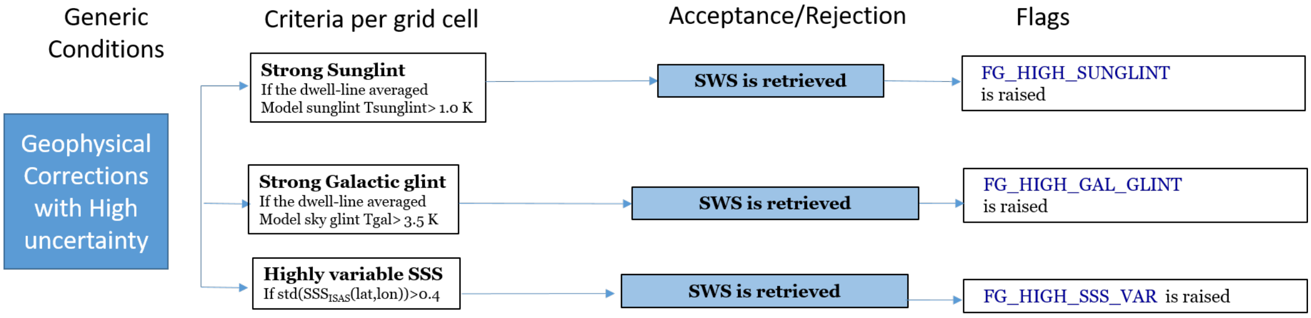

Figure 30: Sketch showing the SMOS NRT wind processor acceptance criteria for specific geophysical correction increased uncertainty conditions. The critera leading to SWS product acceptance and rejection are shown in blue and red colors, respectively. The Flags are internal to the processor and not available within the SMOS Level 2 wind speed product

These includes conditions when the extra-terrestrial reflected signal corrections (sunglint, galactic glints) become significant, such as:

- **Strong Sun glint**:

Error in surface wind speed retrieval induced by excess ΔTbs residuals can happen due to badly corrected sunglint effects on the reconstructed brightness temperature images. Let's assume that the surface wind speed is retrieved at a grid cell from an ensemble of *n* brightness temperature residuals $\Delta Tb_{i=1\ldots n}$.

- If the First Stokes (Tx+Ty)/2 sunglint forward model signal contribution averaged over the dwell-lines, Tsunglint, exceeds CTRL_HIGH_SUNGLINT (set by default to 0.5 K), the measurement will be flagged for sun Glint, i.e., FG_HIGH_SUNGLINT will be raised.

- **Strong Galactic glint**:

Error in surface wind speed retrieval induced by excess ΔTbs residuals can happen due to badly corrected galactic glint effects on the brightness temperature images. Let's assume that the surface wind speed is retrieved at a grid cell from an ensemble of n brightness temperature residuals ΔTbi=1…n.

- If the First Stokes (Tx+Ty)/2 galactic glint forward model signal contribution averaged over the dwell-line, Tgal, exceeds CTRL_HIGH_GALGLINT (set by default to 5 K) the measurements will be flagged for high Galactic Glint, i.e., FG_HIGH_GALGLINT will be raised.

- **Highly variable SSS zone:**

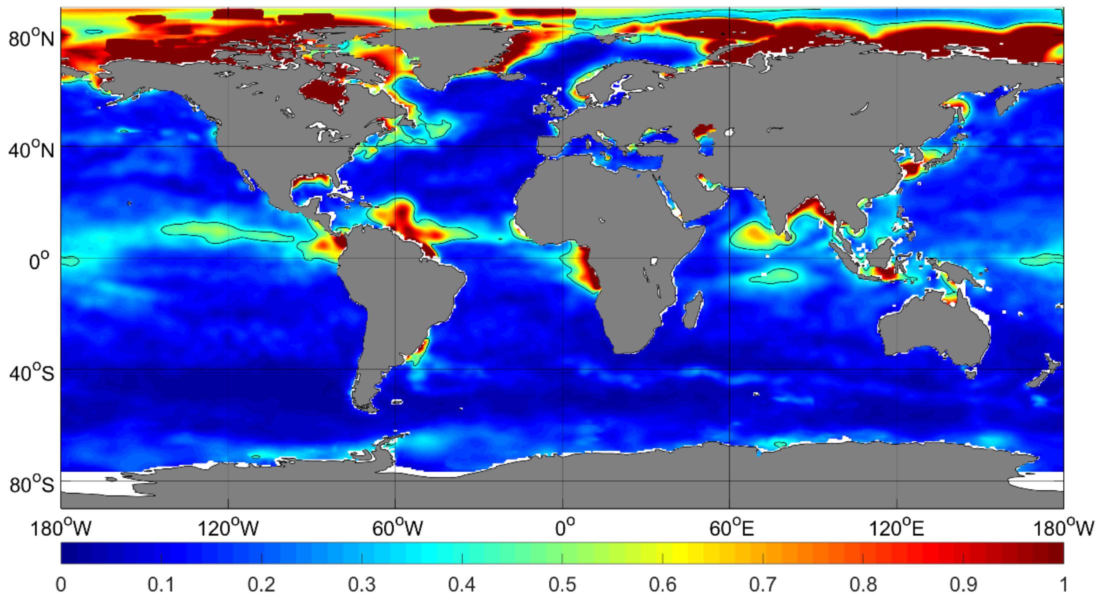

Figure 31: Map of the SSS standard deviation as derived from the ISAS analysis system [RD.21]. The black contour curves indicate area where SSS standard deviation exceed 0.4.

The geophysical correction uncertainty criteria also include uncertainties on the auxiliary sea surface salinity (SSS) value at pixels which is determined in our algorithm using the ocean surface salinity from the CMEMS Operational Mercator global ocean forecast system at 1/12 degree updated daily as the ancillary input field. The CMEMS salinity field is largely based on measurements by drifters from the ARGO network. Though the CMEMS ancillary field is in general of good quality (with an RMS error of about 0.25 psu) there are some instances in which the CMEMS salinity does not accurately represent the salinity within the upper few centimeters of the surface that is seen by the SMOS L-band radiometer. Important examples are:

- ✓ Freshwater outflows from large rivers (Amazon, Congo, Ganges, Mississippi, Rio de la Plato, ...). ARGO drifters cannot get close to the shelf. Therefore, the salinity values from the CMEMS model, which is used in the NRT processing, can be inaccurate, because of the lack of input data. SMOS wind speed retrievals in those areas can have spurious biases and should be used with great care. Observations from locations with a large natural variability in salinity shall be discarded. These issues are resolved in the Final reprocessed version of SMOS winds by using a higher quality ancillary field from salinity retrievals from SMOS data itself, which are not available at the time of the NRT processing.

- ✓ Freshening by heavy rain in low winds can cause stratification within the upper ocean layer. The ARGO drifters measure salinity at 5-meter depth and therefore the CMEMS model, which is based on ARGO, can be too salty compared with the SMOS measurement. The rain freshening effect is not a problem when measuring winds in storms, because at high wind speeds the upper ocean layer is well mixed [Boutin et al., 2015].

To characterize if an SSS retrieval grid cell belong to an highly variable SSS zones, the processor is using a static map of the temporal standard deviation of the SSS (see Figure 28) obtained from the In Situ Analysis System (ISAS) [RD.31].

⇨ If the temporal standard deviation of sea surface salinity (SSS) from ISAS interpolated at the 0.25°x0.25° grid node (lat,lon) is STD(ISAS)> CTRL_SSS_VAR_THRS (default value set to 0.4 psu) then SWS is retrieved but Moderate to strong degradation is expected and the flag FG_HIGH_SSS_VAR is raised.

3.8.5 Out-of range criteria

Finally, one need to check for the validity of the range and values of all the output product fields. As described in the Product Description Document [AD.6], these are:

- ✓ wind_speed
- ✓ wind_speed_error
- ✓ time
- ✓ longitude
- ✓ Latitude
- ✓ across_track_distance
- ✓ Quality levels

The out of range criteria for the 5 first physical variables are provided herebelow.

- **Out of range wind speed value**
  - ⇨ If the processor generate a surface wind speed at grid cell such that**:**

SWS<0 m/s, or

SWS > 80 m/s (~155 kts)

then surface wind speed value is not produced.

- **Out of range time value**
  - ⇨ If the processor generate a time (in days since 1990/1/1) at grid cell with value such that:

    time< start time of input L1B file acquistion

    or

    time> end time of input L1B file acquistion

  then surface wind speed value is not produced.

- **Out of range longitude value**
  - ⇨ If the processor generate a longitude (in °E) at grid cell such that: Lon>180° or Lon <-180°.

  then surface wind speed value is not produced.

- **Out of range latitude value**
  - ⇨ If the processor generate a latitude (in °N) at grid cell such that: Lat>90° or Lat <-90°.

  then surface wind speed value is not produced.

- **Out of range cross_track_distance**
  - ⇨ If the processor generate absolute cross-track distance >600 km, then surface wind speed value is not produced.

3.8.6 Definition of the product Quality Levels

Overview of the QC test Configurable thresholds

To realize the Quality Control (QC) tests listed previously, the SMOS NRT wind processor is using an ensemble of threshold values for several variables which are part of the processor configuration. These threshold values are described in the table 7 below:

Configurable Variables #	Name	Description	Default Value	Unit
1	**CTRL_WATER_FRAC**	Water fraction threshold in surface wind speed retrieval cell.	0.1	N/A

2	**CTRL_SIC**	Sea Ice Concentration threshold in surface wind speed retrieval cell.	0.01	N/A
3	**CTRL_LOW_SST**	Sea Surface Temperature below whch surface wind speed is not retrieved.	1	Degree Celcius
4	**CTRL_DIST2_COAST1**	Critical distance from the SWS retrieval cell to the nearest coasts for which surface wind speed is not retrieved.	100	km
5	**CTRL_DIST2_COAST2**	Critical distance from the SWS retrieval cell to the nearest coasts for which surface wind speed is retrieved but potentially affected by GIBBs effects.	250	km
6	**CTRL_LUT_LSC_MOD**	Threshold absolute value of LSC LUT dwell-line averaged amplitude above which uncertainty is expected in the correction.	1	K
7	**CTRL_NUM_MEAS_VERYLOW**	Critical number of L1 Tbs scenes below which SWS is retrieved from a very low number of measurements.	5	N/A
8	**CTRL_VAR_MEAS_TB_HIGH**	Threshold value of the variance $\mathrm{Var}(\Delta T_b^{i=1..n})$ of the n-multi-angular wind-induced brightness temperature residuals $\Delta Tb_{i=1...n}$ which are used as inputs to retrieve the surface wind speed in a grid cell. Above this threshold, the brightness variance is high and the surface wind speed quality is likely affected by either an RFI contamination or other sources of radiometric uncertainty.	5	K
8	**CTRL_VAR_MEAS_TB_VERYHIGH**	Threshold value of the variance $\mathrm{Var}(\Delta T_b^{i=1..n})$ of the n-multi-angular wind-induced brightness temperature residuals $\Delta Tb_{i=1...n}$ which are used as inputs to retrieve the surface wind speed in a grid cell. Above this threshold, the brightness variance is high and the surface wind speed quality is very likely affected by either an RFI contamination or other sources of radiometric uncertainty.	20	K
9	**CTRL_RFI_TXX**	Theshold brightness values found in the full FOV in XX polarization and above which the snapshot is declared RFI-contaminated.	800	K
10	**CTRL_RFI_TYY**	Theshold brightness values found in the full FOV in YY polarization and above which the snapshot is declared RFI-contaminated.	800	K
11	**CTRL_RFI_UXY**	Theshold brightness value found in the full FOV in third stokes polarization and above which the snapshot is declared RFI-contaminated.	500	K
12	**CTRL_RFI_VXY**	Theshold brightness values found in the full FOV in fourth Stokes	500	K

		parameter and above which the snapshot is declared RFI-contaminated.		
13	**CTRL_SUN_RAD**	Radius around the sun and sun alias images in the antenna director cosine coordinate system within which Tb data are blancked for surface wind speed retrieval.	0.05	n/a
12	**CTRL_HIGH_SUNGLINT**	Threshold sunglint forward model signal amplitude above which data are flagged for sun glint.	0.5	K
13	**CTRL_HIGH_GALGLINT**	Threshold galactic glint scattering forward model signal amplitude above which data are flagged for galactic nglint.	5	K
15	**CTRL_SSS_VAR_THRS**	Thresold value of the temporal standard deviation of SSS from the obtained from the In Situ Analysis System (ISAS) at the 0.25°x0.25° grid node above which surface wind speed will be retrieved in an high SSS variability zone.	0.4	PSU
16	**CTRL_AFOV_BORDER**	Threshold value of the absolute across track distance above which the SWS starts to be degraded	250	km
17	**CTRL_EAFOV_BORDER**	Threshold value of the absolute across track distance above which the SWS starts to be highly degraded	400	km

Table 7*:* List of configurable threshold values to perfom the processor acceptance tests.

Final Quality Levels

The final surface wind speed product is gridded onto a regular 0.25°x0.25° lat/lon grid. To ease the use of the products, we do not provide in the final SMOS Level 2 NRT wind files the ensemble of internal flags which are tested by the processor to qualify a SMOS surface wind speed retrieval at a given geographical grid node. However, we provide a summary of the data quality through a Quality Level index which equal:

quality_level	=	**0**	**(good)**
	=	**1**	**(fair)**
	=	**2**	**(poor)**

The conditions for which the value of the quality levels are established is described in the table 8 below as a function of the individual flag values. Note that the convention assume a value of 1 when a flag is raised (0 otherwise). For the Quality Level (QL), if several flags are raised which produce a similar QL value on the same grid node, the final QL for the grid node will stay the same, except for some Flag combination which are described herebelow in Table 8.

Flag #	Flag Name	Flag Description	Flag Conditions	Quality Level (2) poor	1(fair)	0(good)
0	**FG_SSS_MISS**	This flag is raised when WOA13 SSS is used by the processor instead of CMEMS, SMAP or SMOS SSS to evaluate the flat ocean emissivity.	If **FG_SSS_MISS=1**		1	
			If **FG_SSS_MISS=1** **and** **FG_HIGH_SSS_VAR=1** Situation where both the WOA SSS climatology is used for the retrieval and the SWS retrieval occur in an highly variable SSS area	2		
1	**FG_VTEC_MISS**	This flag is raised when VTEC file from DPGS is not available and the last file used by the processor is used instead.	If **FG_VTEC_MISS=0** or If **FG_VTEC_MISS=1** The algorithm rely on first stokes parameter so that the retrieved wind quality is not affected by VTEC			0
2	**FG_SF_MISS**	This flag is raised when RSGA Solar Flux data are not available to calculate sunglint. The most recent value is used.	If **FG_SF_MISS=1**		1	
			If **FG_SF_MISS=1** & **FG_HIGH_SUNGLINT=1** Situation where the daily sun Tb data is missing and the sungling is high (see Flag 16)	2		
3	**FG_OTT_MISS**	This flag is raised when the OTT is not evaluated based on the last 10 days window. A previous OTT is used instead.	If **FG_OTT_MISS=1**		1	
4	**FG_MIXED_OCEAN_LAND**	This flag is raised when the surface wind speed cell is a mixed ocean/land scene.	If **FG_MIXED_OCEAN_LAND =1**		1	
7	**FG_MIXED_OCEAN_ICE**	This flag is raised when the surface wind speed cell is a mixed ocean/ice scene.	If **FG_MIXED_OCEAN_ICE =1**		1	
9	**FG_HIGH_LSC**	This flag is raised when the LSC LUT correction is above a threshold.	If **FG_HIGH_LSC=1**		1	

10	**FG_SUSPECT_GIBBS**	This flag is raised when the cell is at a distance to coast where Gibbs effects can affect the Tbs.	if **FG_SUSPECT_GIBBS=1**		1	
11	**FG_NUM_MEAS_LOW**	This flag is raised if the number of multi-angular Tbs used for surface wind speed retrieval is below a threshold.	If **FG_NUM_MEAS_LOW=1**		1	
12	**FG_NUM_MEAS_VERYLOW**	This flag is raised if the number of multi-angular Tbs used for surface wind speed retrieval is below a threshold.	If **FG_NUM_MEAS_VERYLOW=1**	2		
13	**FG_HIGH_TB_VAR**	This flag is raised when the multi-angular Tbs used for surface wind speed retrieval shows high variance.	If **FG_HIGH_TB_VAR=1**		1	
14	**FG_VERY_HIGH_TB_VAR**	This flag is raised when the multi-angular Tbs used for surface wind speed retrieval shows very high variance.	If **FG_VERY_HIGH_TB_VAR=1**	2		
15	**FG_EXT_RFI_IN_FOV**	This flag is raised if some of the multi-angular Tbs used for surface wind speed retrieval were discarded because the associated scenes are contamined by RFI.	If **FG_EXT_RFI_IN_FOV=1**		1	
16	**FG_HIGH_SUNGLINT**	This flag is raised if the dwell-line averaged sunglint forward model predicts a significant sunglint signal.	If **FG_HIGH_SUNGLINT=1**		1	
17	**FG_HIGH_GALGLINT**	This flag is raised if the dwell-line averaged galactic glint forward model predicts a significant signal.	If **FG_HIGH_GALGLINT=1**		1	

18	**FG_HIGH_SSS_VAR**	This flag is raised if the surface wind speed cell is located in an area of high SSS variability and where the flat ocean emission correction might be erroneous.	If **FG_HIGH_SSS_VAR=1**	2		
19	**FG_AFFOV-BORDER**	This flag is raised if the surface wind speed is retrieved at across track distances between 250 and 400 kms	If **FG_AFFOV-BORDER=1**		1	
20	**FG_EAFFOV-BORDER**	This flag is raised if the surface wind speed is retrieved at across track distances larger than 400 kms	If **FG_EAFFOV-BORDER=1**	2		

Table 8: List of the flags in the SMOS NRT wind processor and definition of the QC-levels

4. Algorithm for the Wind Radii estimates

4.1 Forewords

As detailed in [RD.4], wind radii estimates in tropical cyclones (TCs) are crucial to helping determine the TC wind structure for the production of effective warnings and to constrain initial conditions for a number of applications. In that context, the capabilities of the new generation of satellite microwave radiometers operating at L-band frequency (~1.4 GHz) have been demonstrated. SMOS and SMAP wind data collected were shown to provide reliable estimates of the gale-force (34 kt), damaging (50 kt), and destructive winds (64 kt), within the best track wind radii uncertainty [RD.4]. Combined, and further associated with other available observations, these measurements can now provide regular quantitative and complementary NRT surface wind information of interest for operational TC forecasting operations.

The maximum radial extent of wind strength are evaluated at several significant wind speed thresholds and are typically referred to collectively as « wind radii ». They generally come in the form of the maximum radial extent of 34-, 50-, and 64-kt (1 kt = 0.514 m s^{-1}) winds in geographic quadrants (i.e., in the northeast, southeast, southwest, and northwest directions). These distances, denoted R_{34}, R_{50}, and R_{64} are reported in units of nautical miles (n.mi, where 1 n.mi = 1.85 km).

In this section, we detail the algorithm that is used to evaluate, when feasible, and in Near Real Time, the wind radii information from the NRT "swath" Level-2 SMOS wind products intercepts with TCs.

4.2 Finding SMOS L2 wind swath intercepts with TCs

In the first step to determining the wind radii from SMOS wind speed fields, the processor interpolates the 6-hourly cyclone center fixes obtained from the Automated Tropical Cyclone Forecast (ATCF) best-track files ([RD.23]) which provide the TC center every 6 hours. The Automated Tropical Cyclone Forecast System (ATCF™) is a software application developed by Naval Research Laboratory, Marine Meteorology Division that provides a toolkit to assist the tropical cyclone (TC) forecaster and to automate and streamline the TC forecast process. The ATCF system is an interactive forecast application that directly addresses the specialized functionality needed to allow forecasters to efficiently prepare the necessary products for the Joint Typhoon Warning Center (JTWC). A modified version is also used by the National Hurricane Center (NHC), the TC forecasting arm of the National Oceanographic and Atmospheric Administration (NOAA). ATCF is provided in two forms: a dedicated application installed on the user's computer, and a web-based version with essentially the same functionality but an insignificant local footprint. For our algorithm, we use the ATCF best-track files (aka B-decks) which are available in real-time from the Tropical Cyclone Guidance Project (TCGP) and provide official synoptic hour positions, intensity and wind radii of Tropical Cyclones.

In a first step, for all SMOS L2 NRT Swath wind products, the algorithm calculate the average date of the full swath product and look for the storm tracks which lifetime include that average date *t*. For those storms, the storm center positions provided at synoptic hours are then interpolated in time using a cubic Hermite interpolation to each satellite swath/storm intercept time (see Appendix 1).

In a second step, the algorithm determine the four SMOS L2 swath wind grid nodes that are the nearest neighbors around the interpolated storm center locations determined in the first step. The average of the "local" dates corresponding to these grid nodes is then evaluated and the previous storm center location is then re-estimated using the again a cubic Hermite interpolation in time. This algorithm to determine at which grid node the SMOS swath L2 wind data intercept with the storm center is applied iteratively until some convergence is reached.

4.3 Determining the wind Radii

Once a SMOS L2 wind swath is found to intercept a storm track and once the storm center location is determined at the time of intercept, in the second step, the retrieved wind field is interpolated onto a cylindrical grid centered on the time-interpolated ATCF storm center. This grid has a radial extent of 1000 kms from the storm center (Fig. 32).

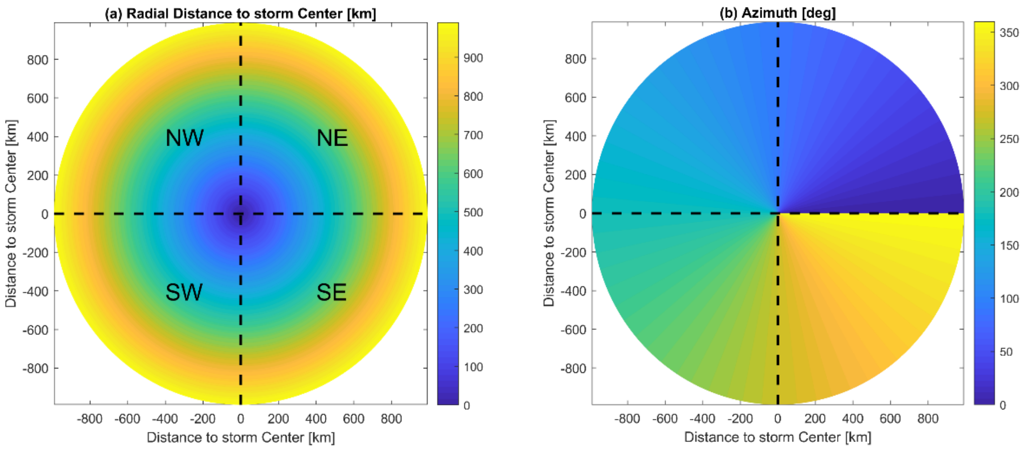

Figure 32: Radial distances (a) and azimuth (b) of the cylindrical grid used to interpolate the L2 swath wind and determine the wind radii per geographical sectors.

The grid has a radial grid spacing of 10 km and an azimuthal sampling of 1 deg. It therefore significantly oversamples the retrieved SMOS L2 wind field. The algorithm then scan the data in each geographical sector per increasing radii. For each geographical sector on this grid, the algorithm then scan the interpolated wind data per increasing radii from 0 to 1000 km. The algorithm is based on successive tests. For a given radii R_i, the algorithm seek for all data found within $r \leq R_i$ and evaluate the fraction of gridpoints within that radial extent for which valid SMOS wind data retrievals exist. Let's denote $F_{validwinds}$ the fraction of non-missing wind data within the domain defined by $r \leq R_i$ and all the azimuths of a given geographical sector.

Step 1: checking data availability in a given sector

- ⇨ If $F_{validwinds} < 30\%$ of the total number of grid points within that domain then no wind radii is produced for that sector.

- ⇨ Condition 1: If $F_{validwinds} \geq 30\%$ of the total number of grid points within that domain, then the wind radii can be further evaluated for that given sector and wind radii incremental value R_i.

Step 2: checking data availability above a certain wind speed threshold in a given sector

- ⇨ If Condition 1 is verified, the fractions of gridpoints for which the retrieved wind speed exceeds each of the three wind speed threshholds (34, 50, and 64 kts) are estimated within the domain defined by $r \leq$ Ri and all the azimuths of a given geographical sector. If the fraction of wind speeds above a critical wind speed (34, 50, or 64 kts) is at least 10% in that domain, then the maximum wind radius at this threshold is set to Ri.

Step 3: The processor then go to next radius increment and apply the same tests until R_i=1000 km.

Step 4: the final maximum wind radius for a given threshhold and geographical sector is the finalR_i for which there is at least 10% of the data that exceed the wind speed threshold in that domain

The 10% filtering is used to remove the presence of small distant patches of high wind speeds that are often detected in the satellite imagery (e.g. see Reul et al., 2017). The preceding algorithm is designed to reduce this bias.

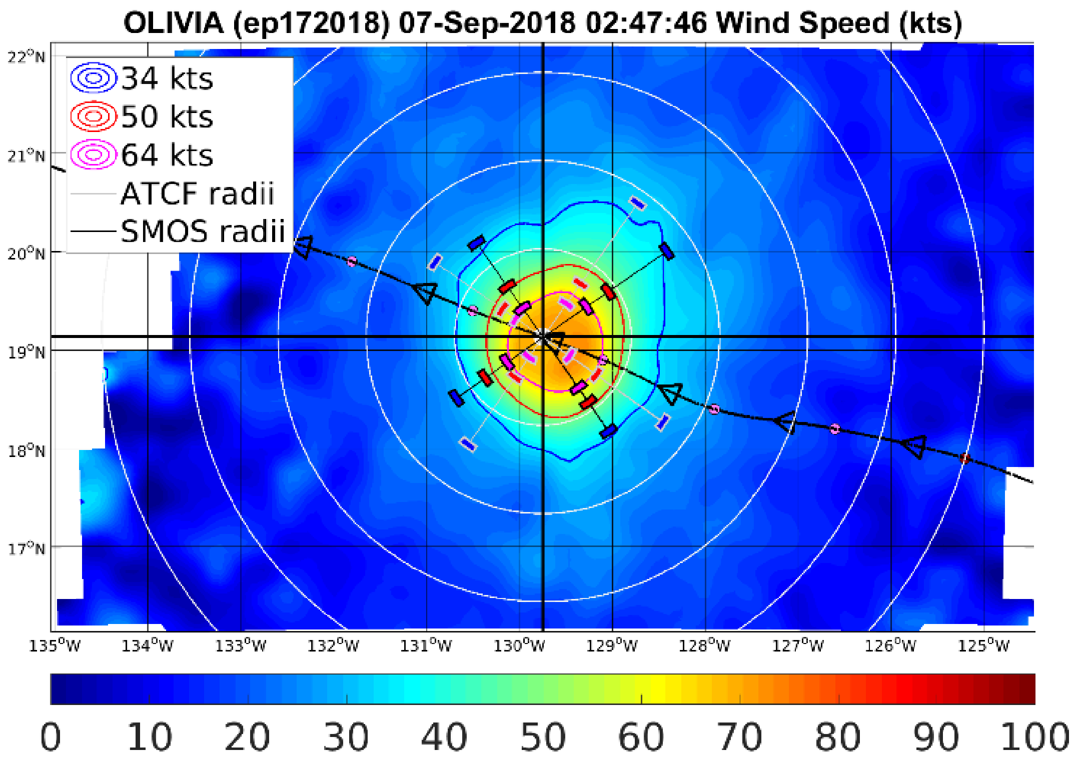

Figure 33: Example of wind radii determined from SMOS L2 swath wind data over TC Olivia in the East-Pacific on 7 Sep 2018. The wind radii per geographical quadrants deduced from SMOS and ATCF forecasts are illustrated by the segments ended by black and grey contoured rectangles, respectively. The color in the rectangles correspond to R_{34} (blue), R_{50} (red) and R_{64} (magenta).

5. SMOS NRT wind Level 3 products

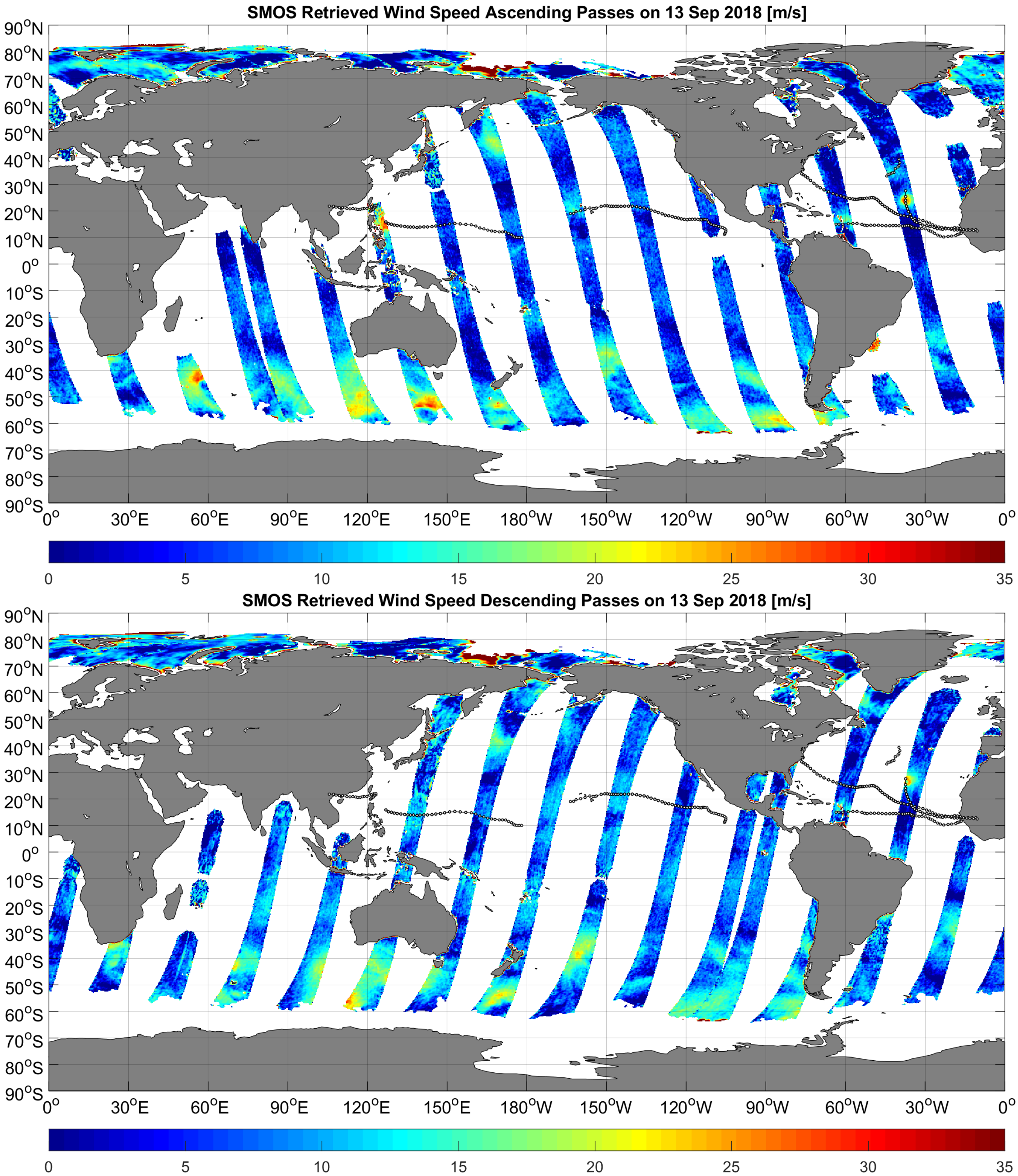

Figure 34: Examples of Level 3 SMOS wind products determined from SMOS L2 swath wind data for the 13 Sep 2018. (top) is ascending passes and (bottom) is descending passes.

It is very convenient to be able rapidly visualizing the SMOS L2 swath wind data accumulated for a given full day, particularly in the context of analyzing the reprocessed NRT wind data.

To do so, a very simple algorithm is collecting the SMOS L2 swath wind product for a specific day and generates global gridded maps of the daily surface winds, separated into ascending and descending passes. These two gridded fields form the so-called Level 3 SMOS wind products (see Fig. 34).

The grid on which the L3 data are generated is identical to the one used by the L2 NRT wind processor.

The only processing performed in addition to collecting the data of the given day per pass type on the same grid is concerning high latitudes where two successive swaths of the same direction (ascending or descending) might overlap.

In this case, the algorithm perfoms a weighted average of the two measurements available for the same grid node. The idea is to give the priority to the best quality wind retrieval in between the two datasets, simply characterized by the theoretical wind speed Bayesian retrieval variance, as described in §3.6.1.

The weight is given by the inverse of the theretical error variance α_i defined in §3.6.1. If n is the number of individual wind speed measurements w_r^i available at a grid node to generate the SMOS Level 3 wind speed product, with respective root mean square error rms_i and if n>1 then, the Level 3 wind speed product at this node will be defined by:

$$\langle w_r \rangle = \frac{\sum_{i=1}^{N} \alpha_i w_r^i}{\sum_{i=1}^{N} \alpha_i}$$

6. Appendix

6.1 Cubic-Hermite Interpolation

Denote four successive grid points in one dimension by (x_0, x_1, x_2, x_3) and consider the problem of interpolating some discrete function F_i, whose values are given at these grid points by (F_0, F_1, F_2, F_3), on the interval $[x_1, x_2]$. We wish this interpolating function to be continuous and to have continuous first derivatives on this interval. Noting that a cubic polynomial provides the freedom to enforce these constraints, we choose our interpolating function to be a cubic polynomial, and we determine coefficients for this polynomial to satisfy our constraints. Let:

$$s = \frac{x - x_1}{x_2 - x_1}$$

and define the interpolating function on the interval $[x_1, x_2]$ by:

$$p(s) = C_1 s^3 + C_2 s^2 + C_3 s + C_4$$

We wish this cubic interpolating polynomial $p(s)$ to pass through x_1 and x_2 so we must have

$$p(s = 0) = C_4 = F_1 \text{ and}$$

$$p(s = 1) = C_1 + C_2 + C_3 + C_4 = F_2$$

Additionally, we want the first derivatives of p(s) to be constrained such that they are identical to the first derivatives of the corresponding p(s) functions on the neighboring intervals. One way to accomplish this is to use centered differences to the define the derivatives at x_1 and x_2. Noting that:

$$\frac{\partial p}{\partial s} = \frac{\partial p}{\partial x}\frac{\partial x}{\partial s} = (x_2 - x_1)\frac{\partial p}{\partial x}$$

We see that:

$$\frac{\partial p}{\partial s}(s = 0) = C_3 = \alpha(F_1 - F_o)$$

$$\frac{\partial p}{\partial s}(s = 1) = 3C_1 + 2C_2 + C_3 = \beta(F_3 - F_1)$$

where:

$$\alpha = \frac{x_2 - x_1}{x_2 - x_o}$$

$$\beta = \frac{x_2 - x_1}{x_3 - x_1}$$

Arranging the preceding four constraints into a matrix equation, we have:

$$M_1 F_i = M_2 c_i$$

where $F_i = (F_0, F_1, F_2, F_3)^{\mathrm{T}}$ and $c_i = (c_1, c_2, c_3, c_4)^{\mathrm{T}}$ and

$$M_1 = \begin{pmatrix} 0 & 1 & 0 & 0 \\ 0 & 0 & 1 & 0 \\ -a & 0 & a & 0 \\ 0 & -b & 0 & b \end{pmatrix}$$

and

$$M_2 = \begin{pmatrix} 0 & 0 & 0 & 1 \\ 1 & 1 & 1 & 1 \\ 0 & 0 & 1 & 0 \\ 3 & 2 & 1 & 0 \end{pmatrix}$$

Now we can write the interpolating polynomial as:

$$p(s) = (s^3, s^2, s, 1)\begin{pmatrix} c_1 \\ c_2 \\ c_3 \\ c_4 \end{pmatrix}$$

But since

$$c_i = M_2^{-1} M_1 F_i$$

we have

$$p(s) = (s^3, s^2, s, 1) M_2^{-1} M_1 F_i$$

and

$$p(s) = \begin{pmatrix} -\alpha s^3 + 2\alpha s^2 - \alpha s^1 \\ (2-\beta)s^3 + (\beta - 3)s^2 + 1 \\ (\alpha - 2)s^3 + -(3 - 2\alpha)s^2 - \alpha s^1 \\ \beta(s^3 - s^2) \end{pmatrix} \begin{pmatrix} F_o \\ F_1 \\ F_2 \\ F_3 \end{pmatrix}$$

Note that the weights are independent of the data Fi and depend only on the desired interpolation location s and the location of grid points xi on which the discrete function is defined.

6.2 Other potential sources of surface wind speed errors

6.2.1 T_B dependencies on sea state

The brightness temperature of the ocean is strongly dependent on the foam coverage due to whitecap and streaks induced by wave breaking and wind tearing of the wave crest (Holthuijsen, L. H., et al., 2012, Norberg, W., et al., 1971, Ross, D. B. and Cardone, V., 1974, Webster, W. J., et al., 1976) but also on the distribution of foam formation thickness (Anguelova, M.D. and Gaiser, P.W., 2012, Golbraikha, E. and Shtemler, Y. M., 2016, Newell, A.C. and Zakharov, V. E., 1992, Reul, N. and Chapron, B., 2003). Recent observations from Holthuijsen et al. (2012) suggest that the whitecap coverage is not increasing at hurricane wind force and above to reach a constant value of about 4%. The “whitening” of the sea surface observed above 64 kt would therefore be dominated by the growth of streak coverage. Whether it is the increasing coverage of these streaks, or the increasing thickness of the whitecaps, or a combination of both that explain the quadratic growth of the radio-brightness at the L-band in extreme conditions remains an open question. Both characteristics can be related to wind speed, but surface wave breaking and streak generation are also strongly dependent on wave growth, wave–wave and wave–current interactions, water depth and the changing (turning) direction of winds. The physics of wave breaking generation processes within hurricanes is complicated by the rapidly turning winds that generate cross-seas and higher sea state in the forward right-hand quadrant of storms in the northern hemisphere (and in the left-hand quadrant for the southern hemisphere). The velocity of the forward movement of the storm, the maximum wind velocity, and radius of maximum wind for a given storm as well as the duration of wind action with respect to the group velocity of waves, are key parameters known to play an important role in determining both the magnitude and spatial distribution of the waves generated within storm quadrants (Kudryavtsev, V., et al., 2015, MacAfee, A. W. and Bowyer, P. J., 2005, Young, I. R., 2003). The wave field is thus more asymmetric than the corresponding wind field, mainly due to the “extended fetch” which exists to the right (left in the Southern hemisphere) of a translating hurricane due to relative wind/wave motions. It is worth noting that the effects of wave–current interaction on surface foam formation may also be important for hurricanes in some areas, e.g. in the U.S., due to the strong influence of either the Gulf Stream (Western Atlantic) or the Loop Current (Gulf of Mexico). Yet, the impact on the radio-brightness contrast at the L-band of wave and wave breaking development and variability in storm quadrants is still poorly known. Thus, algorithms for wind speed retrieval from L-band microwave radiometry must be developed that are sensitive to these effects using a statistically significant number of storm samples from which a new GMF could be derived to account for both wind and wave effects. This is left for future versions of the algorithm.

6.2.2 T_B dependence on rain rate

While much less sensitive to rain than at the higher microwave frequencies, the L-band radiation may still be affected in the hurricane rain bands, in particular in the presence of very strong rain rates. Potentially, the SMOS reported enhancement in the emissivity sensitivity to wind speed above hurricane force, that we previously attributed to sea state changes, could be also associated to the more frequent impact of heavy rain events at the highest winds. Whether a forecaster or scientist can get away with neglecting rainfall at L-band is an important question to investigate.

As described in [RD.31] an excellent approximation for the increase in T_B due to the presence of cloud liquid water and rain is the following:

$$\Delta T_{B,liq} = 2(1-E)\bar{T}_{liq}\bar{a}_{ray}L\sec\theta$$

where E is the sea surface emissivity, $\bar{T}_{liq}$ is the averaged temperature of the rain cloud, $\bar{a}_{ray}$ is the Rayleigh coefficient at temperature $\bar{T}_{liq}$, and L is the total content of liquid water in the field of view. Thus, the increase in T_B due to the presence of clouds and rain at L-band is simply proportional to the total content of liquid water in the field of view. This equation shows that the rain impact shall be about a factor 2 higher at 60° incidence angle than at 10°. As reported in [RD.5] data acquired over the full incidence angle range however all appear to behave similarly above the hurricane wind speed threshold, likely indicating a weak effect of rain on average.

Based on radiative transfer model and some scaling assumptions, we estimated in [RD5] that the maximum TB changes induced by rain could reach 4 K in very intense precipitation. If one assume that the GMF function that we found above hurricane force is not affected by rain impact on the mean (as found at lower wind speeds), than neglecting rain effect would translate into a maximum rain-induced wind speed bias of ~5 m/s.

In an attempt to further partially answer this question, in [RD.5 and RD.1], we analyzed the SMOS and rain data acquired concomitantly within Hurricanes. Unfortunately, most of the brightness temperature data collected above hurricane force are associated with rainy conditions and the contributions to wind and rain-induced emission cannot be separated easily from observations. Given these few example, it is yet difficult to firmly conclude on the potential rain effect at L-band above Hurricane force. A more important data set of co-registered brightness temperature and rain rate data will be required from an ensemble of TCs to established reliable statistics in these conditions.

7. References

Allen, W. T. R. (1983), Wind and sea: State of sea photographs for the Beaufort Wind Scale 57 pp., Atmos. Environ. Serv., Environ. Can., Ottawa, Ontario.

Anguelova, M. D. and F. Webster (2006), Whitecap coverage from satellite measurements: A first step toward modeling the variability of oceanic whitecaps, *J. Geophys. Res.*, 111, C03017, doi:10.1029/2005JC003158.

Anguelova, M. D (2008), Complex dielectric constant of sea foam at microwave frequencies *J. Geophys. Res.*, 113, C08001, doi:10.1029/2007JC004212.

Anguelova, M.D., Bobak, J.P., Asher, W.E., Dowgiallo, D.J., Moat, B.I., Pascal, R.W. and Yelland, M.J. (2009), Validation of satellite-based estimates of whitecap coverage: Approaches and initial results. In, *16th Conference on air-sea interaction, Phoenix, USA 11 - 15 Jan 2009.* Boston MA, USA, American Meteorological Society, 14pp.

Arakawa H. (1954), On the pyramidal, mountainous, and confused seas in the right or dangerous semi-circle of typhoons, *Pap in Meteorol Geophys* 1954;5:114–23**.**

Ardhuin, F., B. Chapron, F. Collard (2009), Observation of swell dissipation across oceans, Geophy. Res. Letter, 36, L06607, doi:10.1029/2008GL037030.

Banner, M. L. and D. H. Peregrine (1993), Wave breaking in deep water, *Annu. Rev. Fluid Mech.*, 25, 373–397.

Bettenhausen M. H., C. K. Smith, R. M. Bevilacqua, N.-Y. Wang, P. W. Gaiser, and S. K.Cox (2006), "A nonlinear optimization algorithm for WindSat wind vector retrievals," *IEEE Transactions on Geoscience and Remote Sensing*, vol. 44, no. 3, pp. 597-608, 2006.

Black, P. G., R. W. Burpee, N. M. Dorst, and W. L. Adams (1986), Appearance of the sea surface in tropical cyclones, Weather Forecasting, 1, 102–107.

Black, P. G., E. A. D'Asaro, W. M. Drennan, J. R. French, P. P. Niiler, T. B. Sanford, E. J. Terrill, E. J. Walsh and J. A. Zhang (2007), Air-sea exchange in hurricanes, *Bull. Am. Meteorol. Soc.*, 88, 357–374.

Boyer, T.P., Antonov, J.I. , Garcia, H.E., Johnson, D.R., Locarnini, R.A., Mishonov, A.V., Pitcher, M.T., Baranova, O.K. and Smolyar, I.V. (2006), *World Ocean Database 2005*. U.S. Government Printing Office, Washington, D.C., DVD.

Bender, M. A. and I. Ginis (2000), Real-case simulations of hurricane–ocean interaction using a high-resolution coupled model: Effects on hurricane intensity. Mon. Wea. Rev. 128:917–946.

Camps, A., Vall-llossera, M., Villarino, R., Reul, N., Chapron, B., Corbella, I., Duffo, N., Torres, F., Miranda, J.J., Sabia, R., Monerris, A. and R. Rodriguez, R (2005), The emissivity of foam-covered water surface at L-band: Theoretical modeling and experimental results from the FROG 2003 field experiment, *IEEE Trans. Geosci. Remote Sens.*, 43, 925–937.

Carrère, L., Y. Quilfen, F. Mertz, J. Dorandeu, J. Patoux (2008), Observing and studying extreme low pressure events with altimetry. Sensors 9, 1306-1329, doi:10.3390/s90301306.

Chao, Y., L. Burroughs and H. Tolman, (2003) Wave Forecasting for the western North Atlantic and Adjacent Waters. *Technical Procedures Bulletin* No. 495, National weather Service, NOAA, U.S. Department of Commerce.

Chao, Y. Y. and H. L. Tolman (2001), Specification of Hurricane Wind Fields for Ocean Wave Prediction. Ocean Wave Measurement and Analysis, San Francisco, CA, B.L. Edge and J. M. Hemsley, Eds., ASCE, 671-679.

Collard, F., F. Ardhuin and B. Chapron (2009), Monitoring and analysis of ocean swell fields from space: New methods for routine observations, J. Geophys. Res., 114, C07023, doi:10.1029/2008JC005215.

Delpey, M. T., F. Ardhuin, F. Collard and B. Chapron (2010), Space-time structure of long ocean swell fields, J. Geophys. Res., 115, C12037, doi:10.1029/2009JC005885.

Donlon, C. J., M. Martin, J. D. Stark, Jonah Roberts-Jones and Emma Fiedler, (2011), The Operational Sea Surface Temperature and Sea Ice analysis (OSTIA), *in press, Remote Sensing of the Environment.*

Donelan, M. A., B. K. Haus, N. Reul, W. J. Plant, M. Stiassnie and H. C. Graber, 2004: On the limiting aerodynamic roughness of the ocean in very strong winds. Geophys. Res. Lett., 31.L18306, doi:10.1029/2004GL019460.

Dombrovskiy, L. A., and V. Y. Raizer (1992), Microwave model of a two-phase medium at the ocean surface, Izvestiya, Atmospheric and Oceanic Physics, 28, 650-656.

D'Asaro E. and C. McNeil (2007), Air-sea gas exchange at extreme wind speeds measured by autonomous oceanographic floats, *Journal of Marine Systems*, Volume 66, Issues 1-4, 5th International Symposium on Gas Transfer at Water Surfaces - Pages 92-109, ISSN 0924-7963, DOI: 10.1016/j.jmarsys.2006.06.007.

Dvorak, V. F. (1984), Tropical cyclone intensity analysis using satellite data. NOAA Tech. Memo. NESDIS-11, 47 pp.

Elachi, C., T. W. Thompson and D. King (1977), Ocean wave patterns under Hurricane Gloria: Observations with an airborne synthetic aperture radar, Science, 98, 609-610.

J. Font, A. Camps, A. Borges, M. Martín-Neira, J. Boutin, N. Reul, Y. H. Kerr, A. Hahne and S. Mecklenburg (2010), SMOS: The Challenging Sea Surface Salinity Measurement from Space, *Proceedings of the IEEE* , vol 98, 5,649-665.

Gloersen, P. and F. T. Barath (1977), Scanning multichannel microwave radiometer for Nimbus-G and Seasat-A. *IEEE Journal of Ocean Engineering* OE-2: 172-178.

Goldenberg, S.B., Landsea, C.W., Mestas-nunez, A.M. and W.M. Gray (2001), The recent increase in Atlantic hurricane activity: causes and implications, Science, v. 293, p. 474–479.

Guo, J., L. Tsang, W. Asher, K.-H. Ding and C.-T. Chen (2001), Applications of dense media radiative transfer theory for passive microwave remote sensing of foam covered ocean, IEEE Trans.Geosci. and Remote Sens., 39, 1019-1027.

Hanson, Jeffrey L., Owen M. Phillips, (1999), Wind Sea Growth and Dissipation in the Open Ocean, J. Phys. Oceanogr., 29, 1633–1648.

Harris, D. L., (1986), Models for the hurricane wave field. Wave Dynamics and Radio Probing of the Ocean Surface, O. M. Phillips and K. Hasselmann, Eds., Plenum Press, 677–681.

Hasselmann K., T.P. Barnett, E. Bouws, H. Carlson, D.E. Cartwright, K. Enke, J.A. Ewing, H. Gienapp, D.E. Hasselmann, P. Kruseman, A. Meerburg, P. Mller, D.J. Olbers, K. Richter, W. Sell and H. Walden (1973), Measurements of wind-wave growth and swell decay during the Joint North Sea Wave Project (JONSWAP)' Ergnzungsheft zur Deutschen Hydrographischen Zeitschrift Reihe, A(8) (Nr. 12), p.95.

Hilburn K. A. and F. J. Wentz (2008), "Intercalibrated passive microwave rain products from the unified microwave ocean retrieval algorithm (UMORA)," *Journal of Applied Meteorology and Climatology*, vol. 47, pp. 778-794.

Holt, B. and F. I. Gonzalez (1986), SIR-B Observations of Dominant Ocean Waves Near Hurricane Josephine, J. Geophys. Res., 91(C7), 8595–8598, doi:10.1029/JC091iC07p08595.

Hock, T. F. and J. L. Franklin, 1999: The NCAR GPS dropwindsonde. Bull. Amer. Meteor. Soc., 80, 407–420.

Katsaros, K. et al., 2000: Wind fields from SAR: Could they improve our understanding of storm dynamics? *Johns Hopkins APL Technical Digest*, **21,** No. 1., 86-93.

Kerr Y. H., P. Waldteufel, J-P. Wigneron, F. Cabot, J. Boutin, M-J. Escorihuela, N. Reul, C. Gruhier, S. Juglea, J. Font, S. Delwart, M. Drinkwater, A. Hahne, M. Martín-Neira and S. Mecklenburg (2010) The SMOS mission: new tool for monitoring key elements of the global water cycle, *Proceedings of the IEEE*, vol 98, 5, 666-687.

Kunkee, D. B. and A. J. Gasiewski (1997), Simulation of passive microwave wind direction signatures over the ocean using an asymmetric-wave geometrical optics model, Radio Sci., 32, 59-78.

Kleiss, J. M., W. K. Melville, J. R. Lasswell, P. Matusov and E. Terrill, (2004) Breaking waves in hurricanes Isabel and Fabian. Preprints, *26th Conf. on Hurricanes and Tropical Meteorology,* Miami Beach, FL, Amer. Meteor. Soc., CD-ROM, 3A.1.

Mecklenburg S., N. Wright, C. Bouzinac and S. Delwart (2009), Getting down to business - SMOS operations and products, *ESA Bulletin*, **137**, 25-30.

Meissner, T., FJ Wentz, (2009), Wind vector retrievals under rain with passive satellite microwave radiometers, *IEEE Transactions on Geoscience and Remote Sensing*, 47, 3065-3083, doi:10.1109/TGRS.2009.2027012.

Melville, W. K. (1996), The role of surface-wave breaking in air-sea interaction. *Annu. Rev. Fluid Mech.*, 28**,** 279–321

Miller, B. I., 1958: The three-dimensional wind structure around a tropical cyclone. National Hurricane Research Project Rep. 15, U. S. Weather Bureau, 41 pp.

Monahan, E. (1971)., Oceanic whitecaps, J. Phys. Oceanogr., 1, 139.

Monahan, E. and I. G. O'Muircheartaigh (1980), Optimal power-law description of oceanic whitecap coverage dependence onwind speed, J. Phys. Oceanogr., 10, 2094–2099.

Norberg, W., J. Conaway, D. B. Ross and T. Wilheit (1971), Measurements of microwave emission from a foam-covered, wind-driven sea, *J. Atmos. Sci*., 429– 435.

Padmanabhan, S., Reising, S.C., Asher, W.E., Rose, L.A. and P.W. Gaiser (2006), Effects of foam on ocean surface microwave emission inferred from radiometric observations of reproducible breaking waves, *IEEE Trans. Geosci. Remote Sen*., vol. 44, no. 3, pp. 569-583.

Pielke R. A., Jr. and C. W. Landsea (1999), La Niña, El Niño, and Atlantic Hurricane Damages in the United States, Bull. Amer. Meteor. Soc., 80, 2027-2033.

Pore, A., (1957), Ocean surface waves produced by some recent hurricanes. Mon. Wea. Rev., 85, 385–392.

Powell, M. D., S. H. Houston, L. R. Amat and N. Morisseau-Leroy, (1998), The HRD real-time hurricane wind analysis system. *J. Wind Engineer. and Indust. Aerodyn.* 77-78, 53-64.

Powell, M. D., S. H. Houston and T. A. Reinhold, (1996), Hurricane Andrew's landfall in South Florida. Part I: Standardizing measurements for documentation of surface wind fields. Wea. Forecasting, 11, 304–328.

Powell, M. D., Eric W. Uhlhorn, Jeffrey D. Kepert. (2009) Estimating Maximum Surface Winds from Hurricane Reconnaissance Measurements. *Weather and Forecasting* **24**:3, 868-883.

Quilfen, Y., J. Tournadre and B. Chapron (2006) Altimeter dual-frequency observations of surface winds, waves, and rain rate in tropical cyclone Isabel, J. Geophys. Res., 111, C01004, doi:10.1029/2005JC003068.

Quilfen, Y., C. Prigent, B. Chapron, A. A. Mouche and N. Houti, (2007), The potential of QuikSCAT and WindSat observations for the estimation of sea surface wind vector under severe weather conditions, J. Geophys. Res., 112, C09023, doi:10.1029/2007JC004163.

Quilfen, Y., B. Chapron and J. Tournadre, (2010), Satellite Microwave Surface Observations in Tropical Cyclones. Mon. Wea. Rev., 138, 421–437. doi: 10.1175/2009MWR3040.1.

Quilfen, Y., D. Vandemark, B. Chapron, H. Feng and J. Sienkiewicz (2011), Estimating gale to hurricane force winds using the satellite altimeter. *J. Atmos. Oceanic Technol., in press.*

Raizer, V. (2007), Macroscopic foam-spray models for ocean microwave radiometry, *IEEE Trans. Geosci. Remote Sens*., 45(10), 3138–3144.

Reul N. (2001), "Foam emissivity modeling at L-band', in "Scientific requirements and impact of space observations of ocean salinity for modelling and climate studies ». ESA contract 14273/00/NL/DC.

Reul, N. and B. Chapron (2003), A model of sea-foam thickness distribution for passive microwave remote sensing applications, *J. Geophys. Res*., 108(C10), 3321, doi:10.1029/2003JC001887.

Reul, N., J. Tenerelli, B. Chapron, D. Vandemark, and Y. Quilfen, (2011), Remote sensing of ocean surface properties beneath hurricanes with the new SMOS L-band radiometer, in preparation.

Ross, D. B. and V. Cardone, (1974), Observations of oceanic whitecaps and their relation to remote measurements of surface wind speed, *J. Geophys. Res*.,79, 444– 452.

Rose L.A, W.E. Asher, S.C. Reising, P.W. Gaiser, K.M.,St. Germain, D.J. Dowgiallo, K.A. Horgan, G. Farquharson and E. J. Knapp, (2002), "Radiometric Measurements of the Microwave Emissivity of Foam," IEEE Trans. Geosci. Remote Sens. 40(12), 2619-2625.

Rosenkranz, P. and D. Staelin, (1972), Microwave emissivity of ocean foam and its effect on nadiral radiometric measurements, J. Geophys. Res., 77, 6528–6538.

Ruf, C.S., Swift, C.T., Tanner, A.B. and Le Vine D.M., (1988), Interferometric synthetic aperture microwave radiometry for the remote sensing of the Earth. *IEEE Transactions on Geoscience and Remote Sensing,* 26, pp. 597-611.

Sampson, R. C. and A. J. Schraeder, (2000) The Automated Tropical Cyclone Forecasting System, version 3.2, *Bull. Amer. Meteor. Soc.,* 81, 1231-1240.

Sienkiewicz J., (2010) Extra-tropical Cyclone Climatology. International Ocean Vector Winds Meeting, Barcelona, 18-20 May 2010.

Smith, P. M., (1988), The emissivity of sea foam at 19 and 37 GHz, IEEE Trans. Geosci. Remote Sens., 26, 541– 547.

Skou N., (2003), Faraday rotation and L-band oceanographic measurements, Radio Sci., vol. 38, p. 8059.

Sharkov A., (2006), Breaking Ocean Waves, Springer-Praxis books in geophysical science, 278pp.

Skou N. and D. Hoffman-Bang (2005)**,** L-band radiometers measuring salinity from space: Atmospheric propagation effects," *IEEE T. Geosci. Remote,* vol. 43, pp. 2210-2217, 2005.

Soden, Brian J., C S Velden, and Robert E Tuleya, (2001) The impact of satellite winds on experimental GFDL hurricane model forecasts. Monthly Weather Review, 129(4), 835-852.

Stogryn, A., (1972), The emissivity of sea foam at microwave frequencies, *J. Geophys. Res.,* 77, 1658–1666.

Schulz J., (2001), "Rain Impact at L-band", "Scientific requirements and impact of space observations of ocean salinity for modelling and climate studies ». ESA contract 14273/00/NL/DC, (2002).

Schlüssel, P. and H. Luthardt (1991), Surface wind speeds over the North Sea from Special Sensor Microwave/Imager observations. *J. Geophys. Res.,***96,** 4845–4853.

Shibata A., (2006), A wind speed retrieval algorithm by combining 6 and 10 GHz data from Advanced Microwave Scanning Radiometer: Wind speed inside hurricanes. *Journal of Oceanography* **62**:3, 351-359.

Uhlhorn, E. W. and P. G. Black, (2003)**,** Verification of Remotely Sensed Sea Surface Winds in Hurricanes*, J. Atm. Ocean. Tech*., 20, 1, 99-116.

Uhlhorn, Eric W., Peter G. Black, James L. Franklin, Mark Goodberlet, James Carswell, Alan S. Goldstein, (2007), Hurricane Surface Wind Measurements from an Operational Stepped Frequency Microwave Radiometer. *Mon. Wea. Rev.*, 135, 3070–3085.

Walsh, E. J. and Coauthors, (2002), Hurricane directional wave spectrum spatial variation at landfall. J. Phys. Oceanogr. 32:1667–1684.

Webster, W. J., T. T. Wilheit, D. B. Ross and P. Gloersen, (1976) Spectral characteristics of the microwave emission from a wind-driven foam covered sea*, J. Geophys. Res*., 81, 3095–3099, 1976.

Wentz F. J. and R. W. Spencer, (1998), "SSM/I rain retrievals within a unified all-weather ocean algorithm," *Journal of the Atmospheric Sciences*, vol. 55, no. 9, pp. 1613-1627, 1998.

Wentz, F. J. (2005), The effect of clouds and rain on Aquarius salinity retrieval, Tech. Memo. 3031805, Remote Sens. Syst., Santa Rosa, Calif.

Wright, C. W. and Coauthors, (2001), Hurricane directional wave spectrum spatial variation in the open ocean. J. Phys. Oceanogr. 31:2472–2488.

Yin, X., J. Boutin, E. Dinnat, Q. Song and A. Martin, (2016), Roughness and foam signature on smos-miras brightness temperatures: A semi-theoretical approach. Remote sensing of environment, 180:221–233, 471, 2016.

Young, I. R., (1988), Parametric hurricane wave prediction model, J. Waterway, Port, Coastal and Ocean Eng., 114, 5,639-652.

Young, I. R., (2006), Directional spectra of hurricane wind waves, J Geophys Res, 111, C08020.

Yueh, S.H., West, R., Wislon W.J., Li, F.K., Njoku, E.G. and Rahmatsamii,Y., (2001), Error sources and feasibility for microwave remote sensing of ocean surface salinity. *IEEE Transactions on Geoscience and Remote Sensing,* 39, pp. 1049-1060.

Yueh S.H., S.J. Dinardo, A.G. Fore, F.K. Li, (2010), “Passive and Active L-band Microwave Observations and Modeling of Ocean Surface Winds”, IEEE Trans. Geosci. Remote Sens., vol. 48, no.8, pp. 3087-3100, Aug. 2010.

Zine S., J. Boutin 1, J.Font, N. Reul, P.Waldteufel, C.Gabarró, J. Tenerelli, F. Petitcolin, J.-L. Vergely, M. Talone, (2008) Overview of the SMOS sea surface salinity prototype processor, IEEE Transactions on Geoscience and Remote Sensing, vol 46, 3, doi:10.1109/TGRS.2007.915543.